Mapping Hydrothermal Alteration Products On Mt Tongariro Using Multispectral Satellite Data, XRD Analysis and Reflectance Spectroscopy

A thesis presented in partial fulfilment of the requirements for the degree of

Masters of Science

At Massey University, Palmerston North, New Zealand

Matthew Eric Irwin

2016

MASSEY UNIVERSITY

For Dumbo and Poppa

Acknowledgements

First and foremost I would like to thank my wonderful wife Kathryn Hutchinson who encouraged me to keep going and get this work done. Words cannot express my appreciation. You are an amazing wife and mother, I am very lucky!

To my two amazing boys, Joshua and Luke, both of you inspire me to be a better Dad and a better person everyday.

Over the years there has been many friends and collegues that have influenced my path, I would like to acknowledge supervisors Mike Tuohy and Shane Cronin for their efforts , John Holland for much encouragement and giving me the confidence to back myself.

Various members of the NZCPA group (in no particular order), Kate Saxton, Pip McVeagh, Ina Draganova, Ian Yule, Reddy Pullanagari, Miles Grafton, Gabor Kereszturi, Eduardo Sandoval, Sue Chok and Istvan Hadju for your support and friendship.

Past members Endang Savitri, Ian Rufe, Ieda Sanchez, Sarah Pitcher Campbell, Mark Coetzee, Paul Nelson, Rob Murray, and Hayden Lawrence. All of you have had a positive influence on me and I thank you for that.

And a special mention for Stefanie Von Buren – gone far too soon.

There is probably many others than I should mention but have forgotten, but I its been so long I just really want to submit asap, so I apologise for my forgetfullness.

"You must unlearn what you have learned." - Yoda

Abstract

The threat of a major collapse/landslide from a volcanic cone is a primary hazard of concern in the Tongariro National Park. The geologic record at Ruapehu and Tongariro volcanoes shows that past debris flows (lahars) have often contained a high proportion of alteration products. The present flanks of volcanoes in the Tongariro National Park have several hydrothermally altered zones that could be sources of future collapses. The purpose of this study was to assess the overall extent of alteration products and map altered zones on Mount Tongariro using field spectroscopy, X-Ray Diffraction analysis and analysis of satellite data.

Hyperspectral data from the Hyperion sensor on the EO1 satellite and multi-spectral data from the Aster sensor on the EOS (Terra) satellite platform were acquired for the study area. The low signal to noise ratio of the Hyperion dataset meant the data was not suitable for analysis. The Aster data was chosen as it contains bands above 1500nm, the wavelength range where diagnostic abosorptions for minerals appear. There were analysis issues with the Aster scene but once the questionable bands were removed, areas of hydrothermal alteration were successfully identified and located.

Mineral samples were collected from a variety of visually unique areas and reflectance spectra recorded using a portable spectroradiometer, along with the GPS locations. These samples were identified in the laboratory using the Spectral Analyst tool in ENVI and comparing them to the USGS, JPL and JHU mineral spectral libraries.

The identification results from the field spectra and traditional X-Ray Diffraction (XRD) analysis of the samples were used to ground truth the satellite data. XRD was used to identify the alteration products and confirm the findings of the field spectra analysis. This enabled the selection of accurate end-members that were used to perform a classification of the imagery of the study area. The XRD and field spectroscopy data correlated well, and only the problem of several mixed minerals hindered a direct corelation.

The alteration products form some of the least stable zones on the volcano. Smectite was identified in many of the samples which is a swelling/shrinking clay associated with volcanic faluire. Identifying these zones provides crucial information in the production of a new lahar hazard map for the Tongariro National Park. The northern flank of the Te Maari craters was found to contain hydrothermal alteration products and this areas has generated many colapses in the past.

Identifying large areas or mapping out larger zones of hydrothermal alteration products was not possible due to the small surface expression of some of the hydrothermal fields and also the atmospheric/signal to noise interference with the main satellite sensors. The mixed method approach used in this study remains useful and ongoing attempts at working with new hyperspectral data as it comes available should be investigated.

Contents

List of Figures

List of Tables

1 Introduction

Catastrophic collapses of volcanic flanks is a major threat to lives, property and infrastructure. The identification of areas prone to collapse is an important step in minimising the potential losses.

Zones of alteration on an active volcano are extremely common, as water permeates into the volcano it is heated and breaks down the parent rock by the process of hydrothermal alteration. These alteration products form some of the least stable areas on the volcano. Identifying hydrothermally altered material on the volcanoes of Tongariro National Park is important due to the threat of a major collapse or landslide from the volcanic cones. The geologic record at Ruapehu and Tongariro volcanoes shows that past debris flows (lahars) have often contained a high proportion of alteration products. Not only is the hydrothermal alteration zone the weak area on the flank of the volcano but clay rich rocks retain pore water during a collapse. This is the case in many other lahar and debris flows around the world. There are several known hydrothermal alteration zones on the flanks of the Tongariro National Park volcanoes, and these areas could be the source of future collapse events, but only a remote sensing survey of the whole volcano will reveal any other zones.

Remote sensing data is a technology that can be used to identify hydrothermal alteration products on the volcanoes of Tongariro National Park. The data can be acquired from a handheld sensor or a satellite. Each provides a different level or resolution of information that can be analysed.

2 Aims

1. Can a portable hyperspectral spectroradiometer be used to identify alteration minerals on the flank of a volcano?
2. Can portable hyperspectral spectroradiometer and XRD mineral identifications be used to classify satellite imagery and what noise processing is needed?
3. How best can a combination of field and satellite methods be used to identify zones of potential failures on stratovolcanos?

3 Literature Review

3.1 Volcanic Hazards and Processes

Active volcanoes often have zones of active hydrothermal systems that work to break down volcanic rock into alteration products or clays. These altered rocks form the least stable areas on the volcano and can be a significant threat to people, plants, animals and infrastructure.

3.1.1 Volcanic Flank Collapses

Catastrophic volcanic collapses generate huge landslides that are a severe hazard to populated regions and infrastructure. Examples of major destructive volcanic collapses include Mount St Helens, Mount Rainer, Mount St Augustine and the shield volcanoes of Hawaii (López and Williams, 1993; Reid et al., 2001) . Catastrophic volcanic collapses globally occur on average four times each century (López and Williams, 1993) and may lead to landslides, debris avalanches and debris flows (Martí and Ernst, 2005). The massive landslide that took place in 1980 on Mount St Helens is one example. The flank collapse of the Mount St Helens was such a catastrophic slope failure that it permitted the eruption of magma and produced explosive lateral blasts (Siebert, 1992) (López and Williams, 1993). Structural collapses of volcanoes are common and include debris avalanches, rock falls, rockslides and sector collapses. These phenomena are caused by steep slopes, faults, weak materials, internal deformations and other factors (Tilling, 1989)
Global volcanic collapse data indicates that horseshoe shaped calderas or depressions with a length between two and 7km are common (López and Williams, 1993). Catastrophic volcanic collapses can devastate areas in excess of 500 km^2 and travel at speeds in greater than 100 m per second (Siebert et al., 1987). There are two styles of eruptions related to hydrothermal processes. The first is “Bandaisan”, where the eruption is solely phreatic and no juvenile material is present. The second is “Bezymianny” which is a Mount St. Helens style eruption where a slope failure occurs and magma is erupted.

Volcanoes generally consist of volcanic clastic rock and lava that has a highly permeable structure. Meteoric water readily infiltrates the system and eventually encounters deep magmatic fluids (Aizawa et al., 2009). Interaction of water with the magmatic fluids produces rock dissolution and hydrothermal mineral alteration that might lead to flank instability. Clays on basal contacts near fault planes provide the perfect mechanism to facilitate slope failure and sudden decompression may trigger a Mount St Helens style of eruption (Tilling, 1989). Identification of hydrothermal alteration zones, weak areas, on the steep slopes of volcanoes can provide useful hazard prediction information. For the Mt Tongariro National Park and surrounding region, although there is a low population, the hydro power scheme is a critical piece of infrastructure that could be adversely affected if a major collapse was to occur.

3.1.2 Debris Avalanches

Volcanic debris avalanches are rapidly moving incoherent and unsorted rock and soil mobilised by gravity, they are a mixture of debris and water with a clay component (Capra et al., 2002). They can range in size from relatively small events to some of the largest mass movements from the Quaternary (Tilling, 1989). Volcanic debris avalanches are different to dry rock avalanches in the amount of material involved. Volcanic debris avalanches produce hills and depressions on their surfaces (Martí and Ernst, 2005).

The stability of a volcano's slope slowly declines when it is subjected to hot, acidic waters of a hydrothermal system over an extended period of time (Hoblitt et al., 1995). Debris avalanches with a clay content >3% in weight of the matrix are defined as cohesive debris flows, and commonly originate as a volcanic collapse or landslides with the clay formed by hydrothermal alteration within the edifice (Capra et al., 2002; Hoblitt et al., 1995). They are classed as cohesive due to the large amount of clay derived from chemically altered rocks (Hoblitt et al., 1995). At Mount Rainer hydrothermal clay minerals are abundant in some of the most widespread lahar deposits indicating a role of hydrothermal alteration in promoting flank collapses (Reid et al., 2001).

Non-cohesive debris flows contain relatively little clay and are triggered by water mixing with loose rock debris, such as the mixing of pyroclastic flows or surges and snow and ice (Hoblitt et al., 1995).

Debris avalanches often accompany eruptions but can also occur during dormant periods (Hoblitt et al., 1995). The majority of debris avalanches travel in excess of 10 km with several events travelling up to 50-60km from the volcano (Martí and Ernst, 2005). Debris avalanches bury and destroy everything in their path and the creation of lahars and floods in a common secondary process generated from the dewatering of the debris avalanche.

3.1.3 Hydrothermal Alteration

Hydrothermal alteration is a stable reaction that occurs in a rock (Rencz, 1999). Hydrothermal solutions have a depositional range of 50-650°C and can carry a wide variety of materials, like gold and muscovite (Evans, 1993). The mineralogy and distribution of hydrothermal alteration products is associated with silicic magmatic intrusions controlled predominately by K+ and H+ ion activity and partly by temperature within the system (Rencz, 1999). Hydrothermal systems are usually small compared with most geological features, the largest being only a few km^3 in volume. Despite their variation in occurrence, a single hydrothermal system is usually restricted to a limited range of minerals, mostly sulphides and oxides (Evans, 1993). This suggests that few chemical processes are important in their genesis (Evans, 1993).

The water for a hydrothermal system has five main sources, surface or meteoric water, ocean water, formation and deeply penetrating meteoric water, metamorphic water and magmatic water. Formation water may have been meteoric water originally but long burial in sediments and reactions with rock minerals give it different characteristics (Evans, 1993).

Clay minerals are layered silicates with sheets of SiO_4 tetrahedra, $Al(O, OH)_6$ and/or $Mg(O,OH)_6$ octahedra (Evans, 1993). Water and other molecules are attracted to their surfaces resulting in the development of plasticity (Evans, 1993). In some clay minerals exchangeable cations (Na^+, K^+, H^+, Ca^{2+}, or Mg^{2+}) are essential to their structure (Evans, 1993). The clays expected to characterise volcanic hydrothermal

alteration (Chapter 2) are Kaolinite and illite, which are the alteration products of acidic volcanic rocks. Further, smectite, the alteration product of rhyolite and tuff could also be expected. Clay deposits normally consist of one or more clay minerals with varying proportions of non-clay minerals, the most common being quartz, feldspar, carbonate minerals, gypsum, and organic material (Evans, 1993). It is possible for hydrothermal alteration to form kaolin, but generally kaolin is formed by weathering (Evans, 1993).

3.2 Remote Sensing

Remote sensing is the technique of obtaining spectral information or measurements without physical contact with the region of interest. The most common type of remotely sensed data is in the form of imagery, and usually with a variety of spectral, spatial, and temporal parameters (Schowengerdt, 2007). It allows data to be collected and analysed for large areas and those areas that are inaccessible or hazardous. Compared to traditional methods of mapping, remote sensing provides a rapid and cost effective assessment of hazards (Reid et al., 2001)

3.2.1 Remote Sensing of Hydrothermal Alteration Products

Altered rocks have a low reflectance at wavelengths of 2.2 µm and a high reflectance at 1.6 µm (Moon et al., 2006). The absorption at 2.2µm is associated to Al-OH bonding, coupled with fundamental OH stretching modes near 2.2µm (Rencz, 1999). Carbonates and minerals with Mg-OH and Fe-OH bonding such as epidote, chlorite, biotite, and phlogopite have absorption features near 2.3µm (Rencz, 1999). Landsat TM band 7 is positioned to detect minerals with absorption features in the 2.2-2.3µm range as a group, due to its wide band width (Rencz, 1999). ASTER has 5 bands between 2.145µm and 2.430µm which may permit further distinction of alteration zones (Rencz, 1999). Clays and hydrous sulphate minerals, including those of hydrothermal origin typically display spectral features near 1.4, 1.9 and 2.1-2.4µm, related to vibrations of structural hydroxyl groups and molecular water (Crowley and Zimbelman, 1997). Iron bearing minerals commonly exhibit broad spectral features in the 0.4-1.2µm region due to electronic transitions in Fe^{3+} and Fe^{2+}, and to Fe-O charge transfer in Fe oxides and oxy-hydroxides (Crowley and Zimbelman, 1997).

3.2.2 Multispectral Remote Sensing Systems – ASTER and Landsat

Multispectral remote sensing refers to systems that capture image data at specific frequencies with discrete bands usually in the visible and infrared regions. Landsat and ASTER (Advanced Spaceborne Thermal Emission and Reflection Radiometer) are two typical multispectral systems. Landsat 7 has 7 bands ranging from 0.45 to 2.35µm in the Visible to Near Infrared (VNIR) and Shortwave Infrared (SWIR) and ASTER has 10 bands ranging from 0.52 to 2.43 µm. Multispectral sensor platforms usually have signal to noise ratios that provide data that can be analysed and the ASTER platform in particular has bands that collect between 2.0 and 2.5µm which is the region of interest when identifying minerals. The disadvantage is there are a limited number of data points to be used for analysis due to the number of bands on the sensor platform.

3.2.2.1 ASTER

ASTER is a sensor system on board the Terra satellite that was launched in December 1999. Terra is in a sun-synchronous orbit of 705 km, and this enables it to cross any given latitude at the same time every 16 days. The ASTER platform is a cooperative project between NASA and Japan's Ministry of Economy Trade and Industry. ASTER has three telescopes, VNIR with a spectral resolution of 15 metres, SWIR at 30 metres and Thermal Infrared (TIR) at 90 metres.

Table 3-1 ASTER Bands and wavelength range for each sensor array (JPL, 2004)

VNIR (15 m)	SWIR (30 m)	TIR (90 m)
Band 1: 0.52 – 0.60 µm	Band 4: 1.600 – 1.700 µm	Band 10: 8.125 – 8.475 µm
Band 2: 0.63 – 0.69 µm	Band 5: 2.145 – 2.185 µm	Band 11: 8.475 – 8.825 µm
Band 3: 0.76 – 0.86 µm	Band 6: 2.185 – 2.225 µm	Band 12: 8.925 – 9.275 µm
	Band 7: 2.235 – 2.365 µm	Band 13: 10.25 – 10.95 µm
	Band 8: 2.360 – 2.430 µm	Band 14: 10.95 – 11.65 µm
	Band 9: 2.360 – 2.430 µm	

There are three data levels with up to 7 products in a level including surface reflectance and digital elevation models. The ASTER Level 2 07XT product is an atmospherically corrected surface reflectance product, which is also crosstalk corrected (a signal scattering phenomenon discoved soon after launch). The 07XT

product provided the best option available to this study for mineral identification, (USGS, 2016).

3.2.3 Hyperspectral Remote Sensing

Hyperspectral remote sensing involves collecting and processing data from the electromagnetic spectrum in many narrow bands over a continuous spectral range. Hyperspectral data can be used in a wide array of applications including agriculture and mineralogy. Some of the issues facing hyperspectral satellite systems are the decreased signal to noise ratio and spectral resolution. Smaller resolution equals low energy per sensor cell and this causes a reduced effectiveness for identifying targets.

3.2.3.1 Hyperion

The Hyperion instrument is one of the sensors on board the EO-1 satellite was launched by NASA on November 21, 2000. The initial mission for EO-1 was a one year technology/validation for the Landsat Data Continuity Mission and this was completed in November 2001. Before the end of the mission there was high interest from the remote sensing and scientific communities to acquire image data, this lead to the EO-1 Extended Mission run by NASA and the United States Geological Survey (USGS).

The EO-1 extended mission is to collect and distribute ALI and Hyperion products in response to Data Acquisition Requests (DARs). The image data collected is archived and distributed by the USGS Center for Earth Resources Observation and Science for public use (van der Meer, 2006).

The Hyperion sensor is comprised of 242 spectral bands ranging from 0.4 to 2.5µm at 30 metre resolution. Each channel is 10nm wide and spaced at 10nm intervals. Images can be 7.5km by 100km land area with high radiometric accuracy. Of the 242 spectral bands 196 are calibrated and can be used for processing.

The sensor range is provided by two separate detectors, SWIR and VNIR. The Hyperion sensor uses a pushbroom 2-D array, which measures cross track spatial variation in a large number of spectral bands simultaneously (Schowengerdt, 2007)

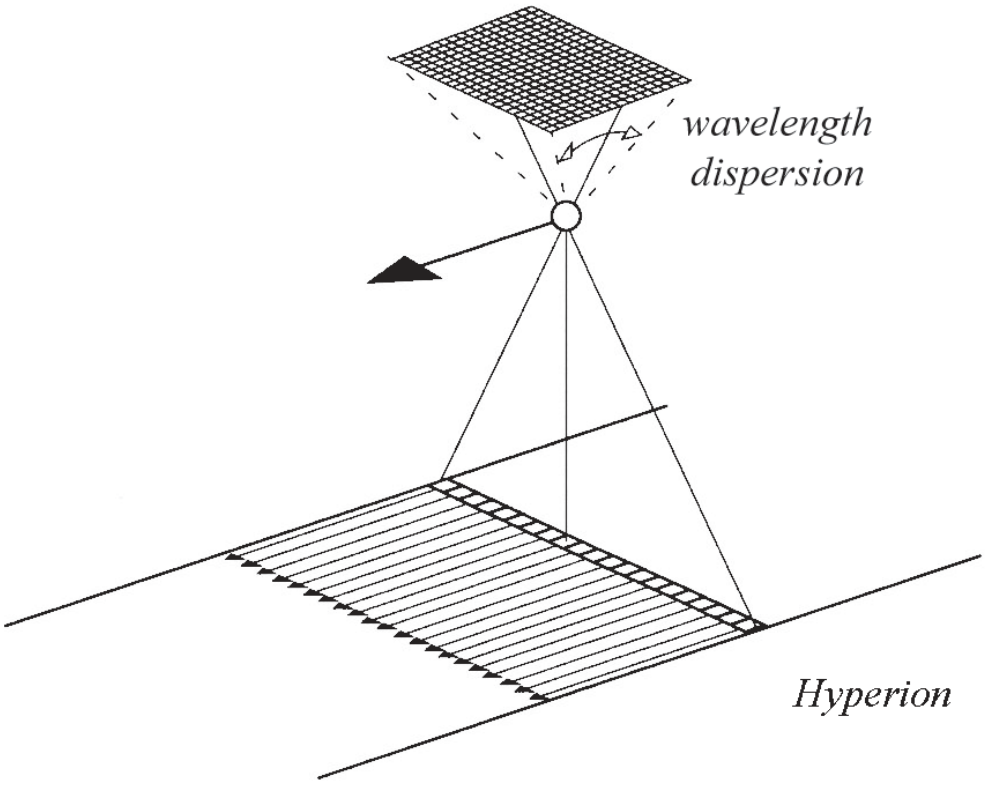

Figure 3-1 : Pushbroom 2-D array concept used in the Hyperion sensor. Each cross track of pixels is simultaneously dispersed in wavelength along the in-track direction of the array. Diagram adapted from (Schowengerdt, 2007).

The Hyperion sensor consists of two spectrometers, one covering 3.6 – 1.06 µm and the other from 0.85 – 2.58µm. The overlap between the spectrometers enables cross-calibration.

The 2.0 to 2.5µm spectral range covers the spectral features of hydroxyl-bearing minerals, sulphates, and carbonates common to many geologic units and hydrothermal alteration assemblages (Kruse, 2003).

3.2.3.2 Signal To Noise Ratio

Signal to Noise Ratio (SNR) for Hyperion ranges from 190 to 40 as the wavelengths increase (USGS, 2003). Signal is the useful part of the image data and the noise is corrupted signal that makes information extraction more difficult (Schowengerdt, 2007). The SNR has a direct effect on spectral mineral mapping, with lower SNR resulting in fewer minerals identified and less detail in specific spectra. Other factors that can affect SNR include site latitude, target brightness, processing level, smoke

and clouds. SNR can be calculated using a Mean/Standard Deviation method for a homogenous target (Kruse et al., 2002). Hyperion data collected under less than optimum conditions have marginal SWIR SNR and allow only the most basic mineral occurrences and mineral differences to the mapped (Kruse et al., 2002).

3.3 Spectroscopy

Spectroscopy is the study of light as a function of light that is emitted, reflected or scattered from an object (Rencz, 1999). Spectroscopy is sensitive to both crystalline and amorphous materials, unlike X-Ray diffraction (explained in section 3.6) which only looks at crystalline methods (Rencz, 1999). For mineral identification the spectral signature of an object is recorded and the spectral features analysed and mapped where they occur. A spectrometer is an instrument that acquires spectra from electromagnetic energy reflected from a target. These instruments can be handheld for use in field sampling, laboratory environment for controlled enviroment analysis, airborne or on a satellite platform. A spectrometer analyses the power spectral density $S(v)$ of an optical signal (Brady, 2009). Optical signals are functions of space, time and polarization as well as wavelength or frequency (Brady, 2009). Spectral information is isolated from optical signals by three mechanisms, Spatial Dispersion, Interferometry and Resonance (Brady, 2009).

There are four parameters of a spectrometer, spectral range, spectral bandwidth, spectral sampling and the signal noise ratio. Spectral range is the range of the electromagnetic spectrum that the sensor detects. The Hyperion spectrometer on the EO-1 satellite has a spectral range of 0.4µm to 2.5µm. Spectral bandwidth is the width of the spectral channels, i.e. Hyperion has a spectral bandwidth of 0.01µm (10nm). If the bandwidth of a spectrometer is greater than 25nm the ability to resolve important mineral absorption features is rapidly lost (Rencz, 1999). A sensor with 0.01 µm wide bands will only receive one third of the energy available compared to a sensor with 0.03 µm wide bands (Aranoff, 2005).

Multiple filters can be used on a sensor platform and a Bandpass Filter only allows light from a selected range to be collected by sensor. The bandpass profile is commonly a Gaussian function and the width of the bandpass (spectral width) is usually defined as the width in wavelength at the 50% response level of the function.

This is called the Full Width at Half the Maximum (FWHM). Spectral sampling is the distance between the spectral bandpass profiles for each channel in the spectrometer as a function of wavelength (Rencz, 1999).

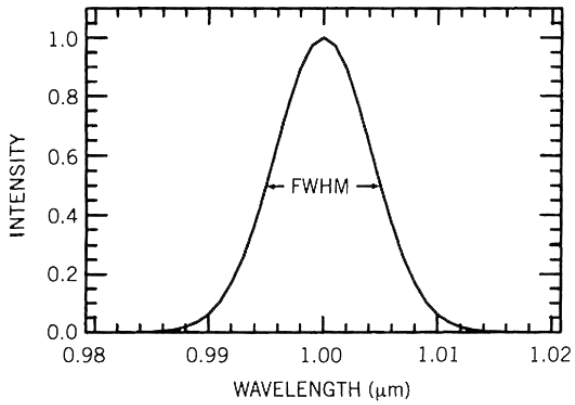

Figure 3-2 Example graph showing the FWHM function

The SNR needs to be high enough to record details in the spectrum. SNR is dependent on the sensitivity of the detector, spectral bandwidth, the energy intensity being reflected or emitted from the surface (Rencz, 1999) and the instantaneous field of view. Higher signal levels mean a reduction in spatial resolution. The challenge is finding a suitable balance between all the factors affecting the SNR to achieve a product that can be analysed successfully.
Hyperspectral spectrometers acquire images in many, very narrow, contiguous spectral bands, typically the number of bands will be greater than 200. This allows effective discrimination of earth surface features using diagnostic absorption and reflection characteristics (Lillesand, 2000).
The Hyperion sensor uses a pushbroom scanner to collect data. A pushbroom scanner has no moving parts and has a higher geometric and radiometric accuracy than scanners that use rotating or oscillating mirrors (Aranoff, 2005). It also have a longer dwell time providing a stronger signal, which improves the ability of the data to provide a useable image under low light levels (Aranoff, 2005).
Hyperion is commonly reported as having a 10nm bandpass, but technically this varies from 10.2856 to 11.5634 nm.

3.3.1 Field Spectroscopy

Field spectroscopy has become an important technique for characterising the reflectance of surfaces “in situ”. In the 1970s there was a research focus to make an accurate instrument that recorded measurements from the 1.1 to 2.4 µm region, as this was known from laboratory measurements to be important for geological applications (Milton et al., 2009).

The ASD FieldSpec Pro is a portable spectro-radiometer with a sampling interval of 2nm and a spectral resolution of 10nm. These specifications meet the nominal sampling and resolution requirements for hyperspectral remote sensing applications (ASD-Inc, 2002).

The FieldSpec Pro records the electromagnetic spectrum in the range of 0.35 to 2.5 µm. The VNIR portion of the spectrum from 350 to 1050 nm is recorded by a VNIR spectrometer. The SWIR portion of the spectrum is acquired by two scanning spectrometers. SWIR1 measures light between 900 to 1850 nm and SWIR2 from 1700 to 2500nm. The ASD software automatically accounts for the overlap in wavelength intervals (ASD-Inc, 2002).

3.4 Spectral Libraries

A spectral library is a digital collection of spectral profiles for a variety of natural and man-made materials, commonly minerals and vegetation in their purest form. ENVI is an image processing software package purchased by Massey University and it is considered to be the premier geospatial software solution to process and analyze all types of imagery and data such as multispectral, hyperspectral, LiDAR and more. There are a number of different spectral libraries that are provided with the ENVI software package. These libraries are stored in ENVI binary image format with the number of samples equal to the number of bands and the number of lines equal to the number of spectra in the library (ITTVis, 2005). There are several groups of laboratory spectra supplied with the ENVI installation from the NASA Jet Propulsion Laboratory (JPL), Johns Hopkins University (JHU), and the U.S. Geological Survey (USGS).

3.4.1 USGS Minerals

Spectra were measured using a Beckman spectrometer at the USGS Denver Spectroscopy Lab. The wavelength accuracy is on the order of 0.5nm in the near-IR and 0.2nm in the visible.

3.4.2 JPL

The JPL spectral library contains spectra for 160 minerals. The spectral library is split into 3 parts according to grain sizes, JPL1 <45 µm, JPL2 45 - 125µm, and JPL 125 - 500µm. The spectra are hemispherical reflectance using a Beckman UV-5240 spectrophotometer with a sampling interval of 0.001µm for 0.4 to 0.8µm and 0.004 µm from 0.8-2.5 µm (ITTVis, 2005).

3.4.3 JHU Minerals

The Johns Hopkins University (JHU) spectral libraries has 15 separate files, including igneous rocks, minerals, soils and snow. The mineral library was measured in bidirectional reflectance from 2.08 to 25 µm (ITTVis, 2005).

3.5 Spectral Angle Mapper

The Spectral Angle Mapper (SAM) is a hyperspectral classification technique that determines the spectral similarity between end-member spectra and pixel spectra in n-dimensional space (Yuan and Niu, 2007). An end-member spectra a material that are spectrally unique (or pure) within the wavelengths of a given image. The observed spectrum can be considered as a vector in the n-dimension where n equals the number of spectral bands (Lillesand, 2000). The SAM is not affected by the topographic effects as the length of the projected vector will increase or decrease due to illumination but the angle will remain constant (Lillesand, 2000). This method can be used with Hyperspectral, Multispectral and Field Spectroscopy data.

3.6 X-ray diffraction

X-ray diffraction (XRD) is an important method for studying crystalline minerals (Whitton and Churchman, 1987). X-ray reflection takes place from lattice planes according to Braggs law

$$\eta\lambda = 2\delta \, sin\theta$$

Where δ is the lattice spacing

Λ is the wavelength of the x-rays

Θ is the glancing angle of reflection

η is the order of the reflection, which can be any whole number

3.6.1 XRD Analysis

Clay minerals can be identified using the X-ray diffraction patterns looking at peak position, intensity, shape and breadth. Kaolinite has reflections based on a 7.1 Å structure while Smectite has reflections at 16.9 Å (Moore and Reynolds, 1989). The XRD pattern of all samples were compared to the International Centre for Diffraction Data (ICDD) powder diffraction files and any clay minerals were identified.

Scanning a range of angles of reflection with a detector gives a pattern of peaks at certain spacings and intensities that are characteristic of the minerals present. As $\delta \propto 1/\sin\theta$ the diffraction angles (2θ) can be converted to d-spacings (space between the atom/lattice planes) by means of standard tables (Whitton and Churchman, 1987).

There are three classes of crystalline clay minerals, 1:1, 2:1 and 2:2 layer silicates. 1:1 layer silicates are one sheet of silicon-oxygen tetrahedral condensed with one sheet of aluminium-oxygen octahedral. The layers are stacked together so that the repeat distance is ≥7.2Å (Whitton and Churchman, 1987). The angstrom is a unit of length equal to one ten billionth of a meter, or 1×10^{-10}m.

2:1 layer silicates are based on mica, having a one sheet of aluminium ions with oxygen in octahedral co-ordination, in between two sheets of silicon-oxygen tetrahedra. In this case the basal spacing is 10 Å. Illites are micas with some replacement of potassium with other cations, with a typical XRD peak is at 10Å. There is no clear distinction between the 10Å peaks of illite and mica and so no differentiation can be made. Vermiculites are also 2:1 layer silicates but all of the potassium has been replaced by other cations. As a consequence the layer separation is greater and a basal spacing of 14Å is exhibited. The basal spacing can collapse to 10Å when all the potassium is substituted for magnesium as the interlayer cation, or where the vermiculite has aluminium hydroxide in the interlayer space and it is heated not higher than 550°C.

Smectites are also 2:1 layer silicates with the tetrahedral and octahedral layers giving

lower charge density between the surfaces. This result is smectites expanding or contracting very readily according to the nature of the exchangeable cations. Ethylene glycol or glycerol can cause expansion and result in a basal spacing of 18Å, alternatively smectites saturated with potassium exhibit a basal spacing of 10Å. Chlorites are often referred to as 2:2 layer silicates and their structure is similar to vermiculites except the interlayer space is completely occupied by magnesium hydroxide or aluminium hydroxide. Chlorites exhibit a 14 Å basal spacing that does not collapse on heating (Whitton and Churchman, 1987).

Interstratified minerals can occur where one layer is one type (10 Å) and the next layers is another type (14 Å), these regularly interstratified minerals have peaks with high spacings (24 Å) with second order spacings at half of the 2 constituents (12 Å). The aim of the XRD analysis was to identify the commonly occurring clay minerals present in the samples, not to estimate the quantities of those minerals, and use those results to validate the ASD spectra.

3.7 Approaches taken in similar studies

Rowan et al (2006) used the pixel purity index to identify spectrally distinct classes from sparsely vegetated areas. These spectrally distinct classes are the “spectral endmembers” used in the identification of the image. They identified eight spectral endmembers, and they used them in a matched-filtering procedure. The Minimum Fraction procedure minimises the response of the background materials and maximises the end-member responses. Bands 5 to 9 were used for most end-members except for the muscovite and unaltered tuff and chlorite end-members that used all 9 bands.

4 Methods

The approach to processing and analysing the samples was to use spectroscopy initially to identify clay minerals in each sample. The samples were then analysed using X-Ray Diffraction (XRD) to validate the spectroscopy results. The satellite data were then analysed to see if the same minerals could be identified, and whether any zones of hydrothermal alteration could be located. The samples taken and their identification via spectroscopy and XRD provide ground-truthing for the satellite analysis results. Initially Hyperion data were selected for analysis as Hyperion is a hyperspectral sensor with bands in the mineral range (2.0 – 2.5 μm), but due to the poor quality of the data they were unsuitable for analysis. The ASTER sensor was selected as an alternative as it contains bands in the mineral wavelengths of interest and the data are freely available. The satellite analysis methods were developed as the data was processed; when a problem or issue was encountered a new method or process was developed and applied. The main approach was to strip away all the data that was not of interest to allow the remaining data to be separated into its principal components or endmembers.

4.1 Sample Collection

Clay samples were collected in two field trips to Tongariro National Park (2005 and 2006), 21 samples were collected for laboratory analysis. Clays often display a wide range of coloured material especially white, yellow, red and green, that relate to the mineral composition of the sample. Therefore, the aim was to collect as many visually unique coloured samples that represented the range and type of hydrothermally altered materials encountered. The main hydrothermally altered areas of Mt Tongariro, Ketetahi Hot Springs, Central Crater, Emerald Lakes and South Crater, were traversed and samples collected on (Figure 4-1) A GPS location was recorded and a unique sample identification number allocated for each sample (Figure 4-2).

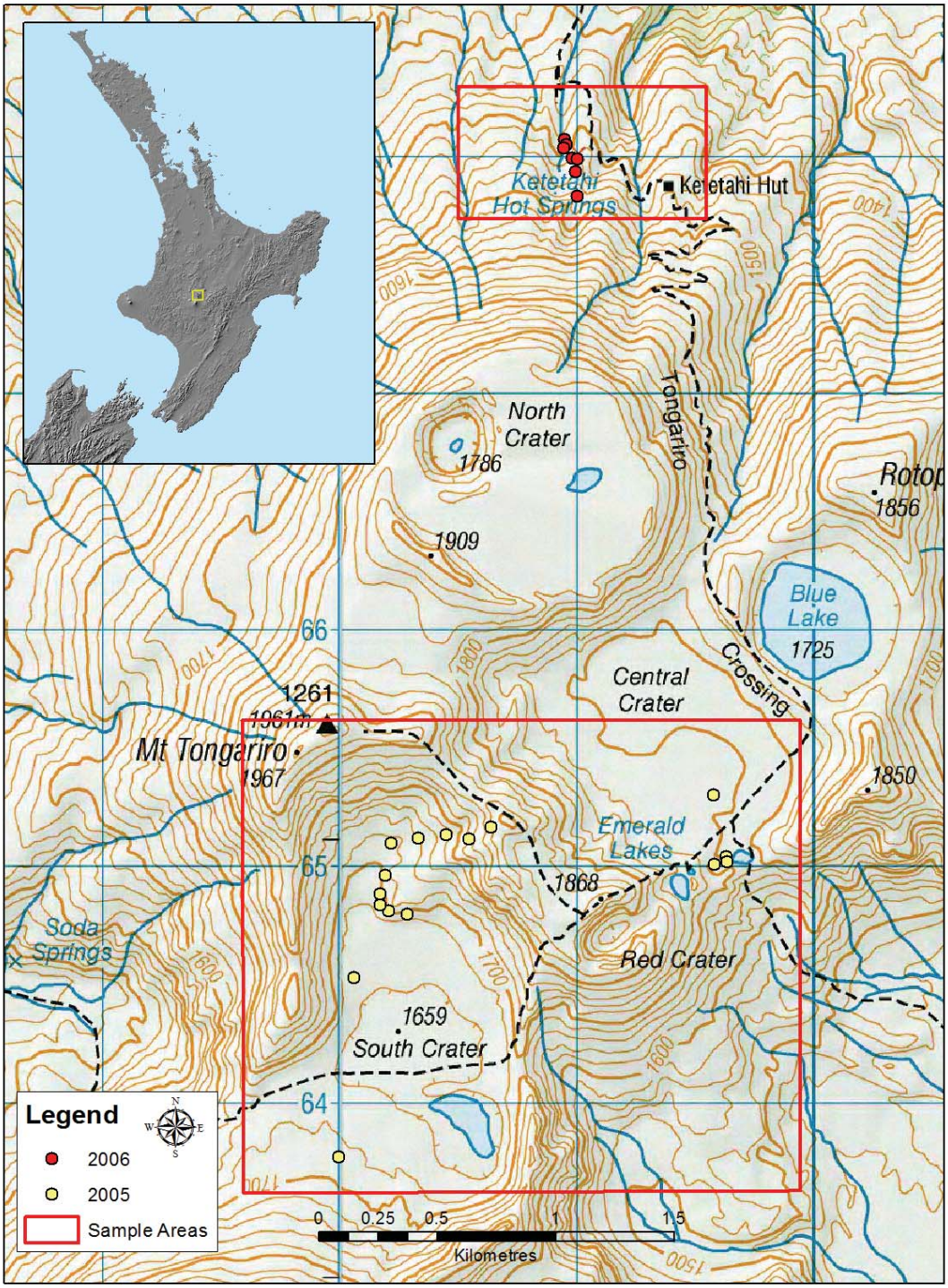

Figure 4-1 Overview map of sample collection locations taken in 2005 (yellow dots) and 2006 (red dots) for analysis

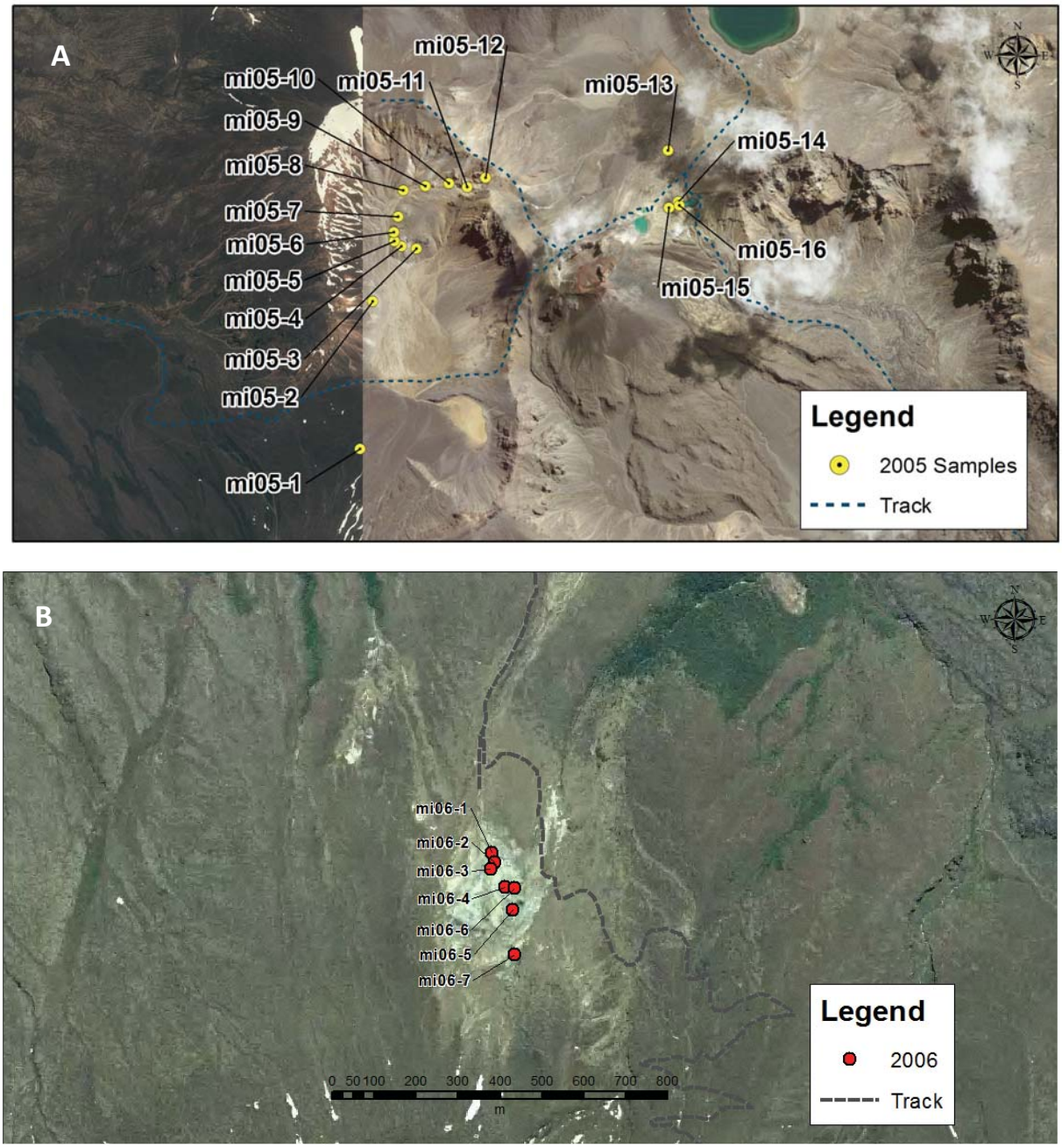

Figure 4-2 Location samples from Mt Tongariro taken in 2005 (A) and 2006 (B)

4.2 X-Ray Diffraction Methods

The aim of the XRD analysis was to identify the presence of clay minerals, not to estimate quantities.

Field samples were air-dried rather than oven dried, because drying at a temperature greater than 105°C can breakdown some clay structures. A more hydrous form of Halloysite when heated to 105°C can change to a “so-called” Kaolinite, and the 10Å form may transform to the 7 Å form at temperatures as low as 70°C (Brindley and Brown, 1980).

Raw air-dried samples were finely ground with an agate pestle and mortar. Powder mounts were prepared by gently pressing the powder into the sample holders. Samples were then placed in the diffractometer ready for scanning (Figure 4-3).

Figure 4-3 Samples loaded into the diffractometer for scanning

X-Ray Diffraction (XRD) measurements were made using a GBC Scientific EMMA diffractometer operating at 35 kV and 20 mA, using monochromatic Co Kα radiation and a scanning rate of 2° 2θ/min. Samples were scanned from 5 ° to 60° 2θ.

Clay mineral phases were identified by comparing the XRD scan of each sample to the International Centre for Diffraction Data (ICDD) powder diffraction files using both the Search-Match program and manual inspection. Ten samples had XRD scan results indicating smectite was present, some had a typical smectite XRD scan and some had a scan result which showed the presence of smectite and other clays . Samples MI05-5 and MI05-6 were selected to represent the two types of XRD scan results for smectite. These two representative samples were treated with 10% glycerol and air dried. The main objective of treatment with glycerol was to identify the nature of the non-swelling clays, and to discriminate between the swelling clays (Mosser-Ruck. R et al., 2005).The samples were ground in a mortar and pestle and gently pressed into sample holders and scanned from 2° to 40°. If the clay present is smectite then after treatment with glycerol the peak will shift. Treatment with formamide can discriminate Kaolinite from halloysite. Without formamide treatment a sample with Kaolinite or halloysite can only be classified as Kandite. Slurry of clay was prepared and evaporated onto a glass slide. Once dried, the samples were scanned in an using a GBC Scientific EMMA diffractometer operating from 8 to 20° to determine the

background peaks. The slides were then lightly sprayed with formamide ($HCONH_2$) and rescanned. If Halloysite is present, a peak will appear at 10.4Å, whereas Kaolinite does not expand beyond 7.2Å (Churchman et al., 1984).

4.3 Spectro-radiometer data collection

The ASD FieldSpec Pro is a portable spectro-radiometer with a sampling interval of 2nm and a spectral resolution of 10nm. The FieldSpec Pro records the electromagnetic spectrum in the range of 0.35 to 2.5 µm. Reflectance measures were collected for each sample *in situ* for the 2005 field visit and in the laboratory with a spectroradiometer (Fieldspec Pro, ASD inc). The ASD spectroradiometer suffered a fault and all the data collected on 2005 were unusable. No *in-situ* measurements were made with the ASD in the 2006 sample collection. The ASD spectroradiometer was used in the laboratory for collection of reflectance data on all samples. Once they had been dried and ground, ready for XRD analysis (section 4.2) they were placed under the contact probe with its own light source, that minimises the errors associated with stray light, and a reflectance scan was measured.

4.4 Spectral Analysis Methods

Using the Spectral Analyst Tool in ENVI, spectra recorded with the ASD were compared to a number of spectral libraries to identify the minerals in each sample based on their spectral characteristics. Spectral libraries relevant to identifying minerals in ENVI are from NASA Jet Propulsion Laboratory (JPL), Johns Hopkins University (JHU), and the U.S. Geological Survey (USGS) .

Many minerals are similar in one wavelength range and different in another. Abundant spectral features for common alteration minerals appear at wavelengths between 0.4 and 2.5 µm. Two key spectral features of alteration minerals occur near 1.4 and 1.9 µm, but these regions are obscured by atmospheric absorption. Due to this the 2.2 µm spectral region is particularly important for detecting and identifying clay minerals (Hunt and Ashley, 1979). Using a wavelength range that contained diagnostic absorption features for altered clay minerals (1.4 to 2.5µm) provided the best opportunity for correct identification of the minerals of interest (ITTVis, 2005).

The Spectral Feature Fitting (SFF) technique in the Spectral Analyst module was used as the first step in identify the unknown spectra recorded with the ASD Fieldspec Pro. SFF compares the fit of the unknown spectra to the library spectra using a least-squares

technique and is an absorption-feature based methodology, the continuum is removed from both spectra and the reference spectra are scaled to match the unknown spectra. Higher match scores indicate a higher confidence because more rules were satisfied (ITTVis, 2005). The similarity scores are used to rank the materials from the spectral library in order from highest to lowest, called a spectral ranking. High scores for multiple materials may indicate mixtures.

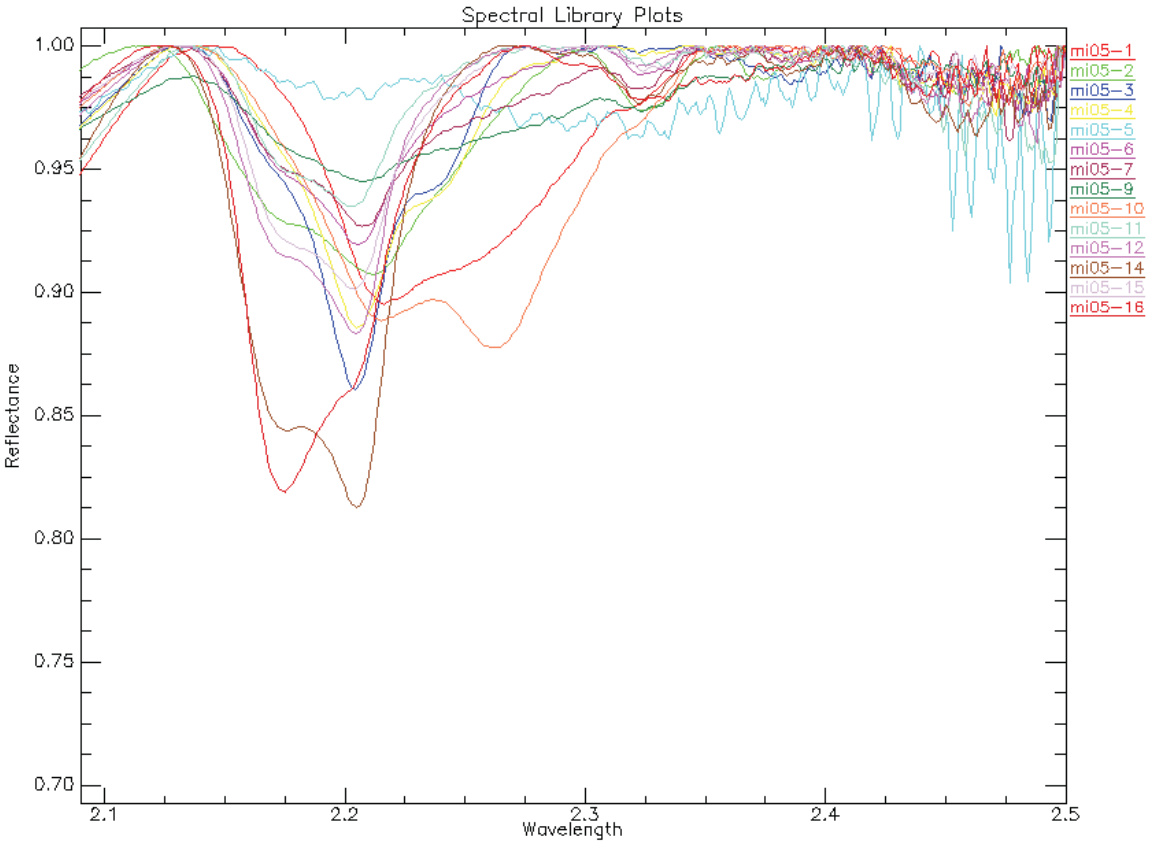

Figure 4-4 Continuum removed spectral plot of all samples over the wavelength range of the JHU library

The Spectral Analyst does not identify spectra; rather it recommends likely candidates based on the minerals that are present in the reference spectral library. As a result materials that are not present in the sample may be identified and score highly because they satisfy the most match rules. For example, if the spectral library does not contain a spectra for Kaolinite but does have Halloysite, a sample that contains Kaolinite will probably have its best match with Halloysite.

The user is responsible for the actual identification. The spectral ranking for each sample was checked and assessed in the context of the knowledge gained from the XRD data analysis and taking into account the environment where the samples were acquired the

most likely match was selected from the Spectral Analyst results. To test the robustness of the spectral analysis the ASD spectra of the samples were compared to the three spectral libraries, JHU, USGS and JPL.

4.5 Hyperion Processing Methods

Initially a Hyperion hyperspectral dataset was selected for its potential to provide mineral identification information at a spectral range that matched the ASD Fieldspec Pro. A Hyperion dataset acquired on the 4th June 2003 was selected as it was the closet cloud free data set that matched the field sampling collection when the ASD spectroradiometer was used to record *in-situ* rocks.

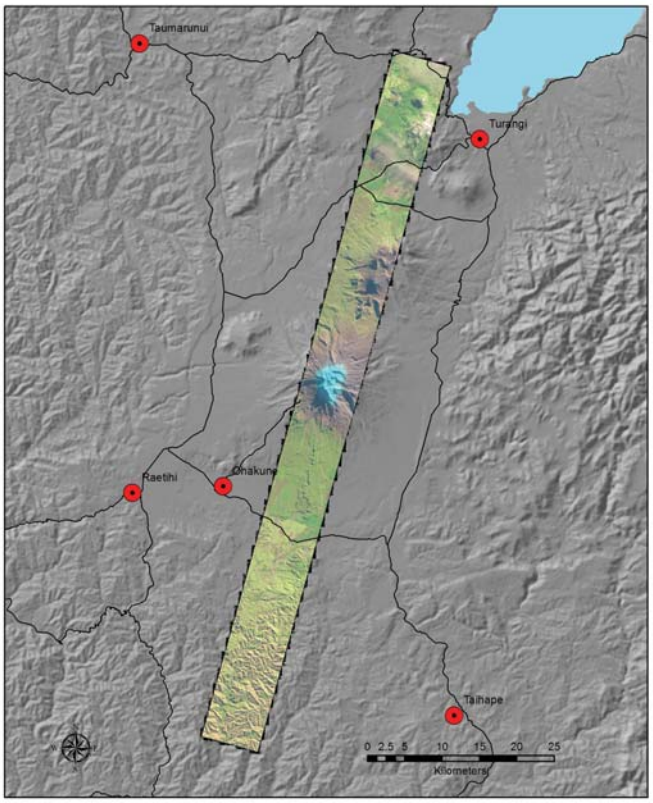

Figure 4-5 Location of the full Hyperion scene acquired 4th June 2003

The Hyperion on the EO-1 satellite passes over New Zealand at 10am every 16 days and the low sun angle at 10am results in a poor signal to noise ratio.

Before any mineral identification can be attempted the Hyperion data was converted from radiance to reflectance. The ENVI software contains an atmospheric correction module called FLAASH.

4.5.1 FLAASH

Fast Line-of-sight Atmospheric Analysis of Hypercubes (FLAASH) is a first-principles correction tool in ENVI that corrects wavelengths of most hyperspectral and multispectral sensors. The FLAASH tool was used to convert the Hyperion imagery from radiance to reflectance . The atmospheric model estimates the standard column water vapour, and the FLAASH documentation suggests selecting a model with similar or somewhat greater water vapour amounts than is expected for the scene. The atmospheric models are standard MODTRAN model atmospheres.

Mean precipitable water vapour values for June from Gillingham (Gillingham, 2002) state a value of 0.9 cm (derived from MODIS data). Based on these data the US Standard or Mid-Latitude Winter models were appropriate for use with the study scene correction (Table 4-1).

Table 4-1 FLAASH atmospheric model selection based on water vapour amount in the scene (sea level to space) (ITTVis, 2005)

Model Atmosphere	Water Vapor (std atm-cm)	Water Vapor (g/cm^2)	Surface Air Temperature
Mid-Latitude Winter (MLW)	1060	0.85	-1° C (30° F)
U.S. Standard (US)	1762	1.42	15° C (59° F)
Sub-Arctic Summer (SAS)	2589	2.08	14° C (57° F)
Mid-Latitude Summer (MLS)	3636	2.92	21° C (70° F)

If the water vapour and air temperature values are unknown for the area then the model can be selected based on the latitude. The Hyperion image centre is at -39°S and was acquired in June meaning SAS is probably the best option, but the MLS or MLW could also provide an acceptable result (Table 4-2).

Table 4-2 Atmospheric model selection for FLAASH based on time of year (ITTVis, 2005).

Latitude (°N)	Jan	March	May	July	Sept	Nov
-30	MLS	MLS	MLS	MLS	MLS	MLS
-40	SAS	SAS	SAS	SAS	SAS	SAS
-50	SAS	SAS	SAS	MLW	MLW	SAS

The water retrieval option was set to Yes because Hyperion data has the required bands available for performing the retrieval. In this process, the column water vapour for each pixel is determined and used to solve the radiative transfer equations that allow surface reflectance to be computed.

More than 25 different corrections were run using the FLAASH tool, experimenting with different combinations of the processing parameters. The spectral profiles of pixels were assessed for each correction attempt to determine the effectiveness of the correction to produce an acceptable reflectance image that could be used to match minerals from a spectral library.

During the FLAASH correction process there were warnings about the calculated solar elevation being very small. This indicates that the dataset may not be ideal for mineral identification.

Less than ideal data have been described by Kruse et al (Kruse et al., 2003) states that Hyperion data collected under less than optimum conditions has marginal SWIR SNR and only allows the identification of very basic mineral assemblages and differences. As a result of these findings no further analysis was conducted on the Hyperion image.

4.6 ASTER Processing Methods

The ASTER 3 band VNIR 07XT product was resampled to 30m using ENVI, and then combined with the 30m SWIR 6 band data to create a 9 band dataset. The float function in ENVIs Band Math tool was used so the resulting image contained real data values and not integer data which would result in an unsuitable dataset because the data values are converted to integers and data detail is lost.

The Minimum Fraction procedure minimises the response of the background materials and maximises the end-member responses. Higher numbers from the resulting matched-filter images indicate good matches, and the highest degree of match for each endmember was classified and overlaid on the Band 1 ASTER image.

A series of raster masks were applied to the dataset to reduce the range of pixels and remove the pixels that can be identified spectrally that are not of interest. The desired targets were the bare ground and sparsely vegetated pixels as these are the pixels that may show signs of hydrothermal alteration. A similar approach to that of Rowan et al (2006) of identifying spectral endmembers was then applied to the ASTER dataset.

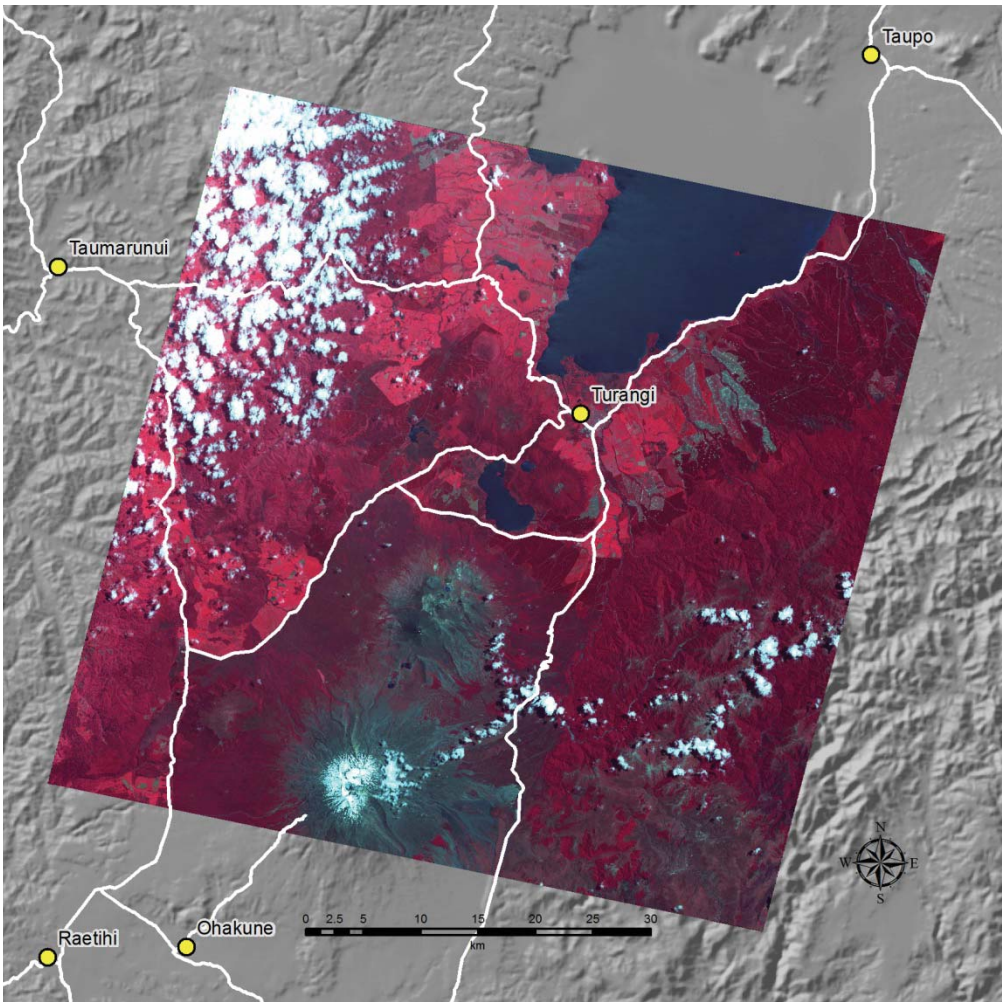

Figure 4-6 A the full ASTER image in false colour (14533); B the image after clipping using the National park boundary.

The full ASTER dataset was clipped to the Tongariro National Park boundary as the project was specifically on the national park and not the surrounding land in the image. This initial step also reduced the size of the dataset making data processing faster.

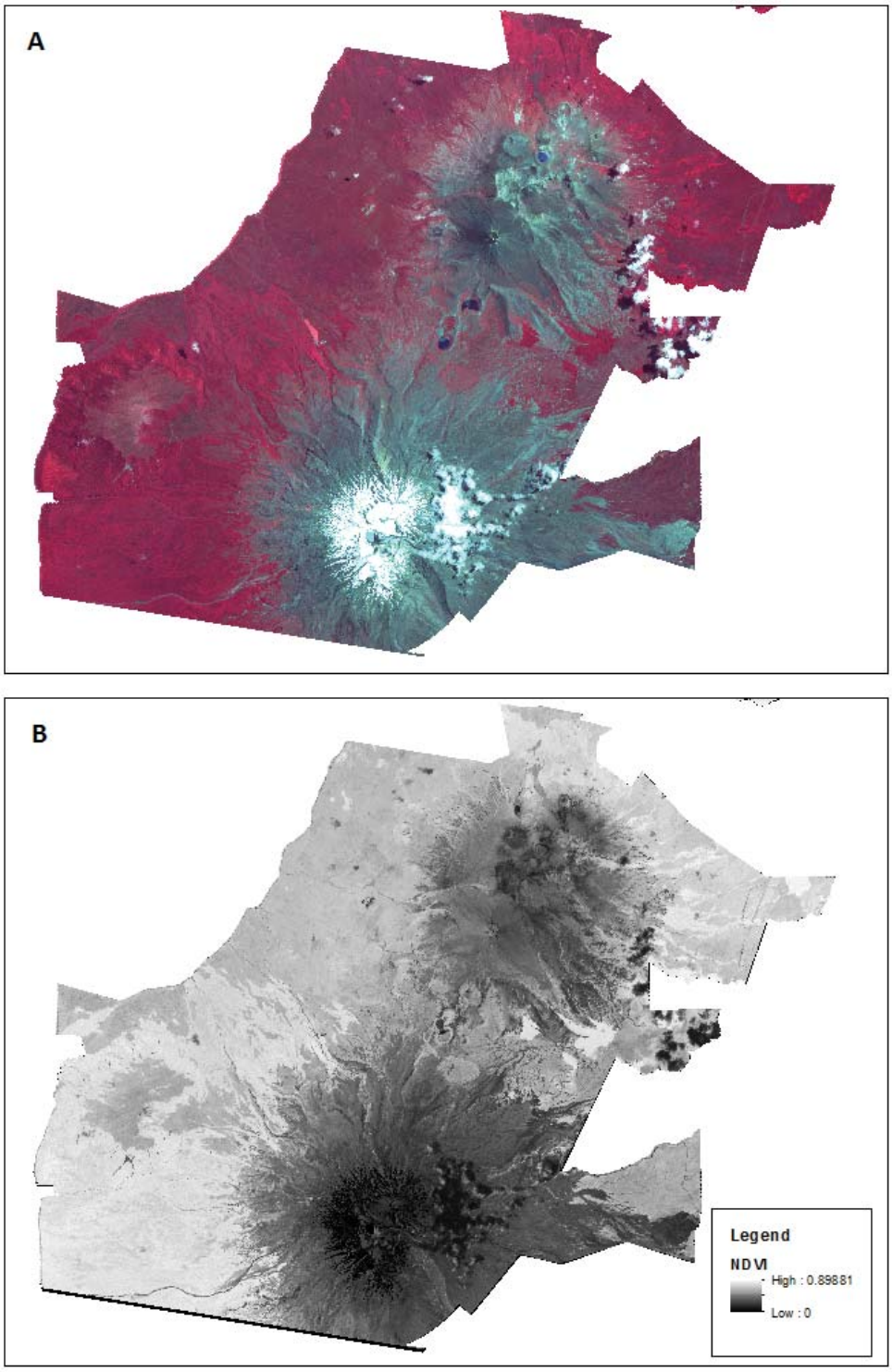

Figure 4-7 The calculated NDVI for the clipped Tongariro National Park image using bands 2 and 3.

To separate the vegetation in the image, Normalised Difference Vegetation Index (NDVI) was calculated from the clipped image. ENVI uses the standard NDVI algorithm $\frac{(NIR-Red)}{(NIR+Red)}$

where NIR is the near-infrared band and Red is the red band. Higher NDVI values indicate more green vegetation. Pixels with NDVI values from 0.55 (sparse vegetation) to 1 (dense vegetation) were used as a band threshold to identify groups of spectrally similar pixels from the dataset. These pixels form vegetation mask and were removed from the dataset. The areas of snow were classified using the Target Detection Wizard in the ENVI software. The detection wizard searched the image for pixels that matched the snow spectra from the JHU spectral library. The JHU spectral library contains four snow spectra, of these the Coarse Granular Snow was identified in the image. Once identified these pixels were used to create another mask and were removed from the dataset.

Using the spectral response of a cloud in the image all spectrally similar pixels were identified and removed from the image. The same procedure was performed on the image to mask out the water areas. The final masked dataset (Figure 4-8) was then ready for analysis using classification procedures. .

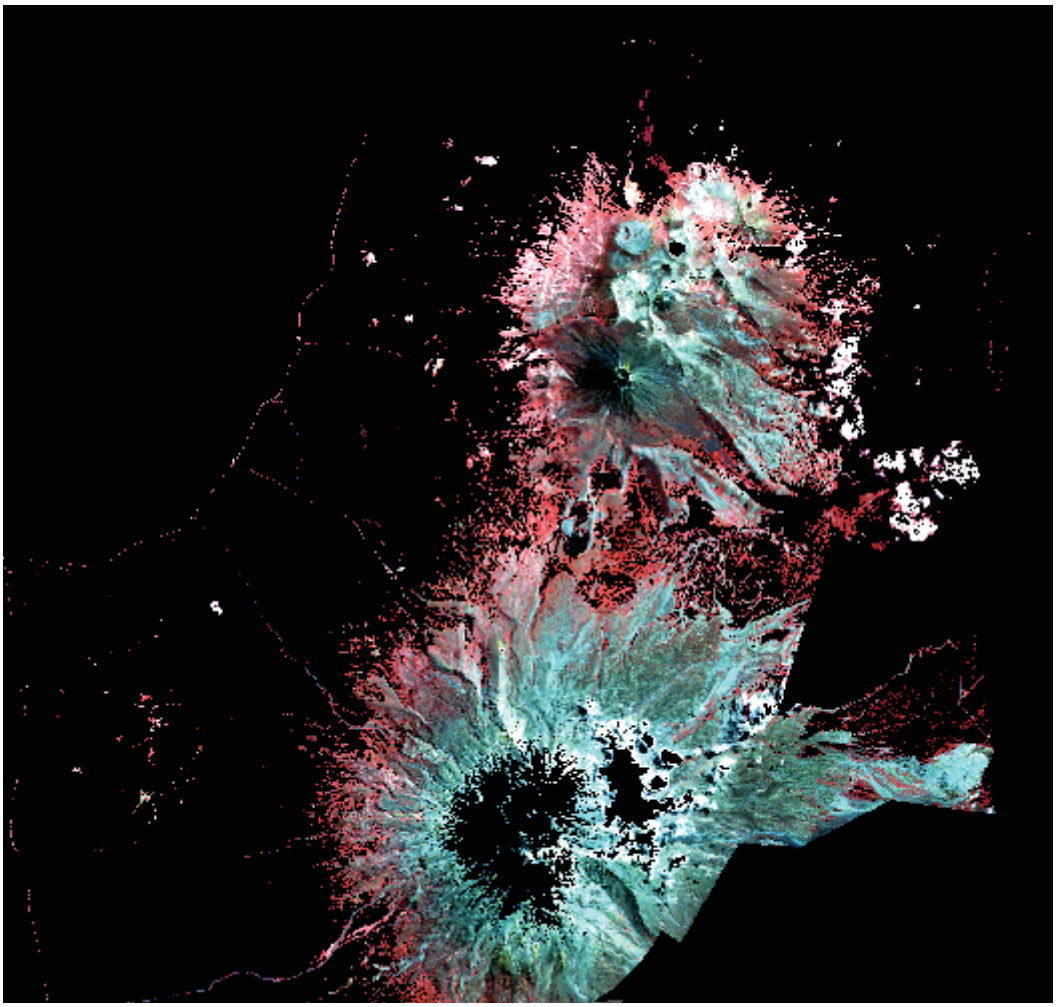

Figure 4-8 the ASTER image after the vegetation, snow, cloud and water masks were applied, the black pixels are the masked areas and the remaining pixels are the false colour ASTER image.

4.6.1 ASTER Band Statistics

Some classifications were attempted on the masked dataset but none of these were successful in identifying any hydrothermal zones. It was suspected that there could be some issues with the dataset and a better understanding of the dataset was required to find out why the classification results were unsatisfactory. For the 9 ASTER bands the maximum, mean and standard deviation statistics were calculated for the entire scene and for the scene after the masking process had been applied.

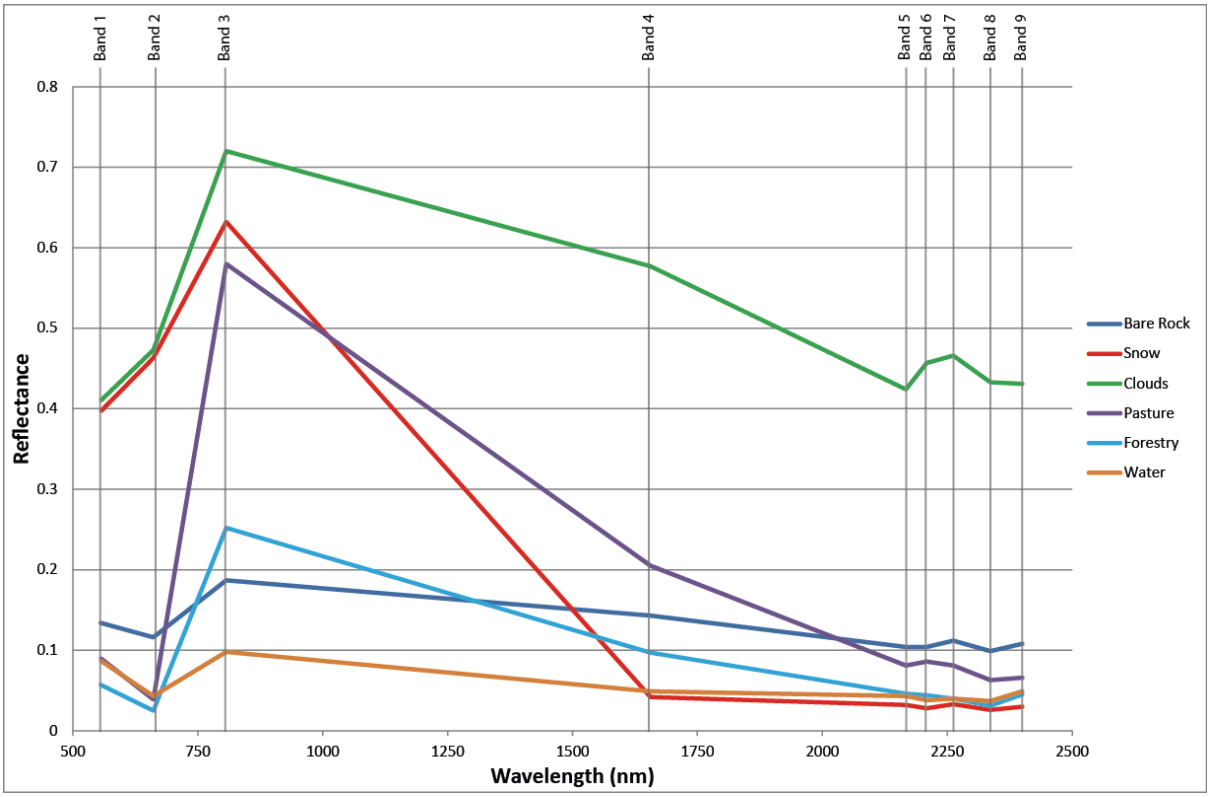

Figure 4-9 Spectral plots of typical targets in the ASTER image.

Typical targets within the ASTER image are bare rock, snow, clouds, pasture, forestry and water (Figure 4-9). The reflectance values will change based on what the reflectance for the typical targets are within each band. For example, clouds (green line) have high values in all bands and if all of these pixels are successfully removed through the masking process then a drop in the maximum values for bands 1,2 and 4-9 is expected, as long as there are no other high pixel values from other sources still present in the dataset. Band 3 has high values from snow and pasture so removing the clouds will only change the data range a small amount.The standard deviation is a better indicator as it shows how the distribution of data in that band is affected after the masking process is applied.

After masking only the sparsely vegetated to non-vegetated areas remain, the clouds, water bodies, vegetation and anything beyond the Tongariro National park boundary were removed. The result of the masking is a smaller range of data in most bands; the actual effect is different depending on the wavelength that each band captures and the wavelengths of the pixels being removed.

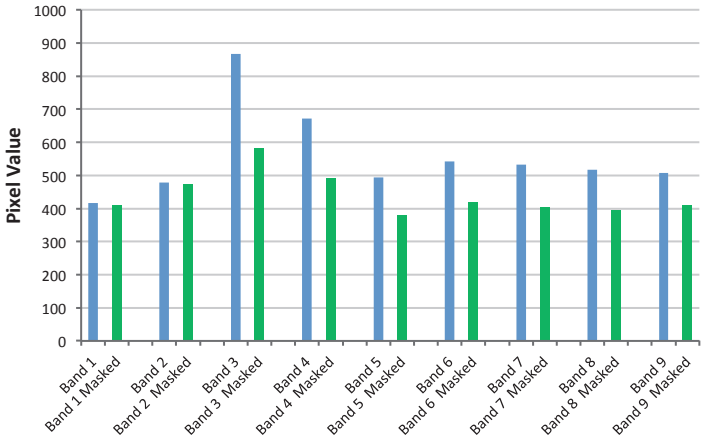

Figure 4-10: Maximum values for Full Scene and Masked ASTER bands

In most bands the maximum values drop a small amount due to the removal of the clouds and snow (Figure 4-10). The biggest difference is shown in Band 3 with a wavelength of 0.807 µm. This is in the red-near infrared region and with majority of the vegetation removed from the scene this drop is expected. Pasture, clouds and snow all have a high reflectance in Band 3 (Figure 4-9), which explains the decrease in the maximum values and the mean value (Figure 4-11) after the masking process.

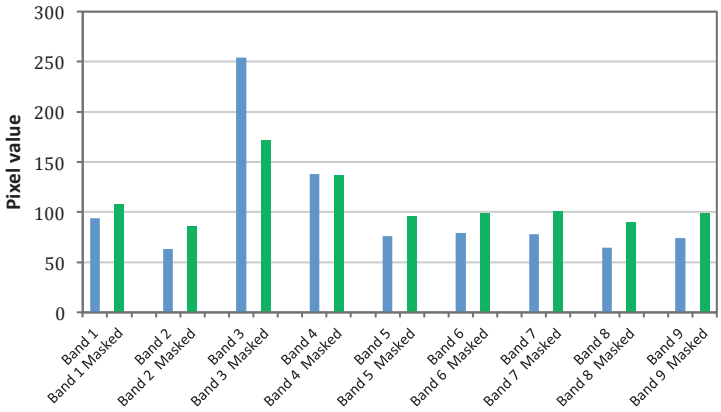

Figure 4-11: Mean values for Full Scene and Masked ASTER bands

The mean value for each band gives us the average pixel value within the scene. For mean values of the bands there is a drop in band 3, but higher mean values for the other bands in the masked image (Figure 4-11). Removal of the majority of vegetation, cloud and snow pixels only has a small effect on the mean value. In most bands pixels of vegetation, cloud, and snow still remain but may not be in the high or low section of the data range. Standard deviation values for the scene provide a better explanation of the affect masking the unwanted pixels has on the dataset. By eliminating the majority of the unwanted pixels from the dataset (water, vegetation, snow) all bands show a much smaller standard deviation (Figure 4-12), with each band now containing a narrower range of pixel values .

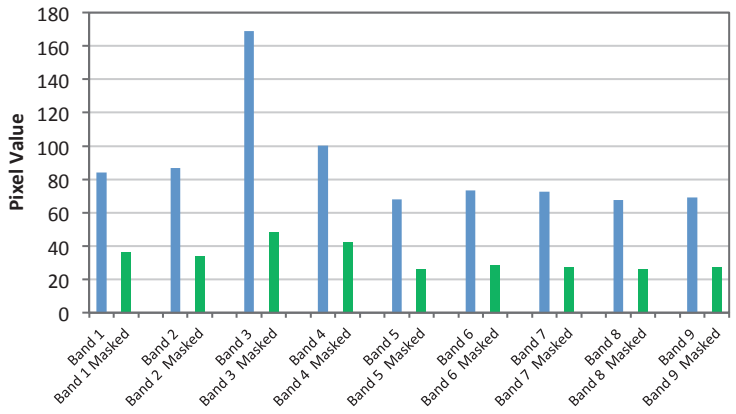

Figure 4-12 Standard deviation of the pixel values from the ASTER dataset for the full scene (blue) and masked scene (green)

When the percentage of pixels in the full scene and masked scene were plotted against the wavelength changes in the data distribution after the masking can be seen for each band (Figure 4-13). Masking allows the remaining data to be dissected easier and also speeds up the processing time.

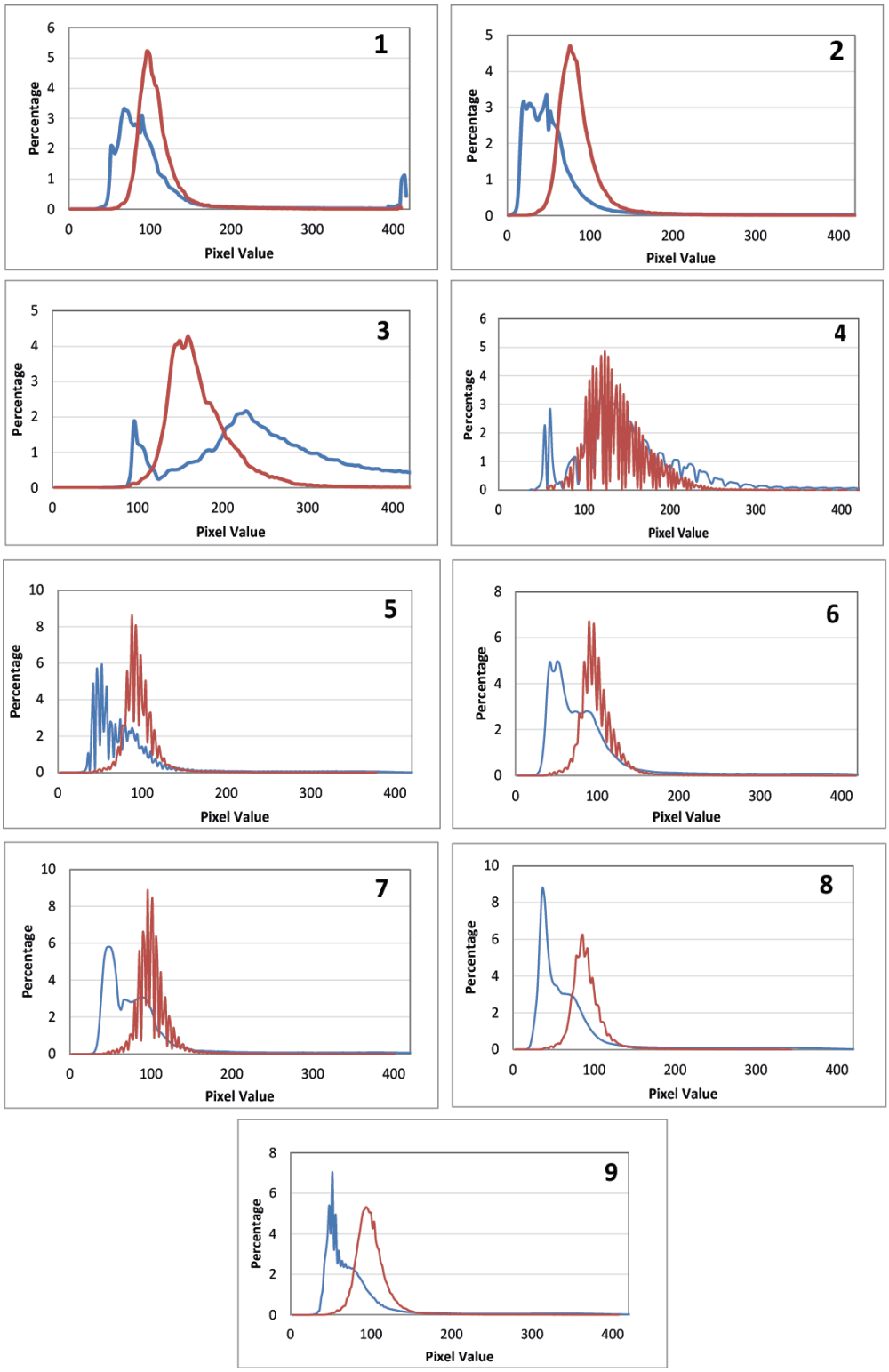

Figure 4-13 Pixel value distribution for the full scene (blue) and masked scene (red) for each of the 9 ASTER bands as labelled.

For this dataset, bands 4-7 (SWIR bands) exhibit an unusual sensor detector response. The data pixel values do not follow a standard smooth response, rather the percentage of pixel

values are higher or lower than expected (Figure 4-13 D-G). For bands 4 and 5 this odd response is expressed in the full and the masked dataset, but for bands 6 and 7 the fluctuations only appear in the masked dataset. This might indicate the errors are associated with the sensor response to bare ground pixels. It is likely to be the result of detector errors, due to the consistentcy of the fluctuations. This study did not attempt to establish the reason for the anomalies in bands 4 to 7, instead the data for these bands were removed from the dataset and a new analysis performed on the remaining bands.

4.6.2 Colour Slicing

Colour slicing is an image processing technique that allows the user to assign colours to data ranges to highlight areas of an image. The slice ranges selected were based on the position of the peaks for each band (Figure 4-13). Each colour represents a different target type in the image (Figure 4-14)

In Band 1 there were four distinct peaks, after the masking process was applied ne peak remained (Figure 4-13 A). Using a colour slice tool to highlight the data ranges in the full scene it shows that three of the peaks represent the different vegetation classes within the image, and the peak on the far right of the graph represents snow and clouds (Figure 4-15 A). The light blue colour slice represents the sparse vegetation to bare ground pixels. After the masking process the pixels remaining in Band 1 are areas of sparse vegetation to bare ground.

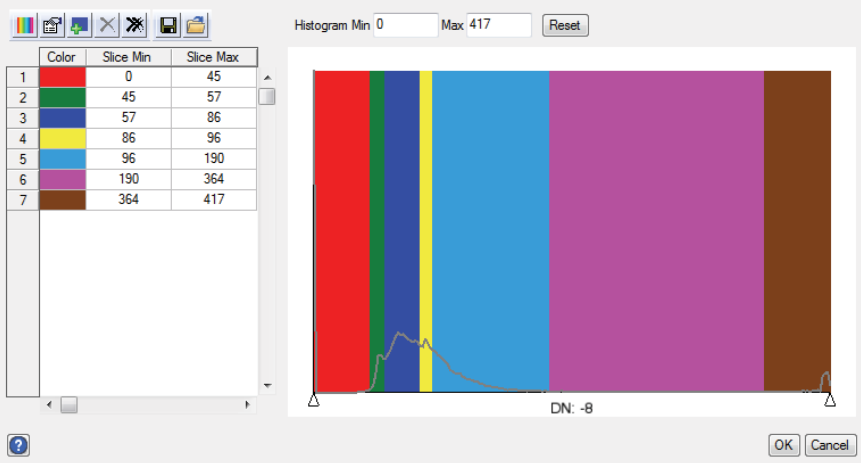

Figure 4-14: Colour slice for ASTER Band 1

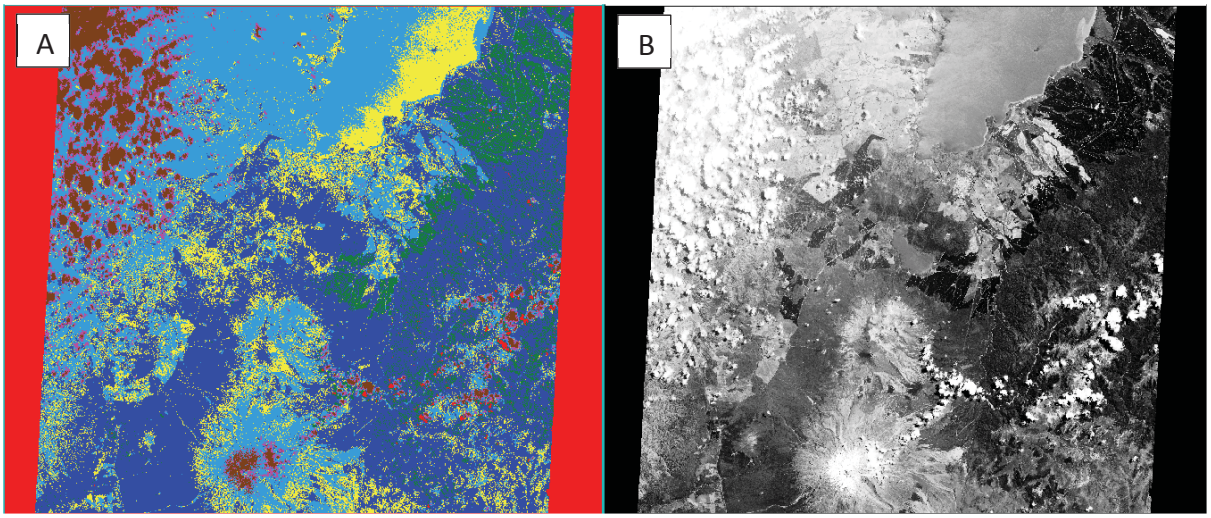

Figure 4-15: ASTER Band 1 colour slice using the parameters from figure 11 (A) and Band 1 in greyscale (B) for comparison.

Setting the break values to include different peaks in the data and then comparing with the infrared or visible image can be used as a confirmation that the masking was set to the correct threshold values.

The colour slice for Band 3 (Figure 4-17) highlights how different bands can be used to identify different image targets. In Band 3 it is easier to identify the lake (green) than Band 1 (Figure 4-15), conversely the clouds are not identified as easily in Band 3 as they are in Band 1.

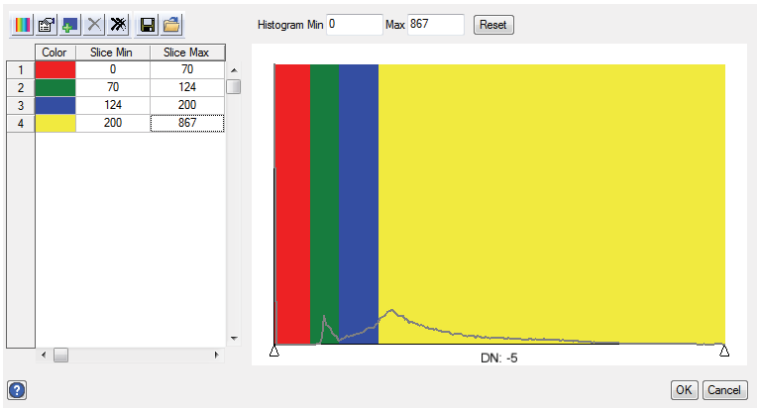

Figure 4-16: Colour slice parameters for ASTER Band 3 (Infrared)

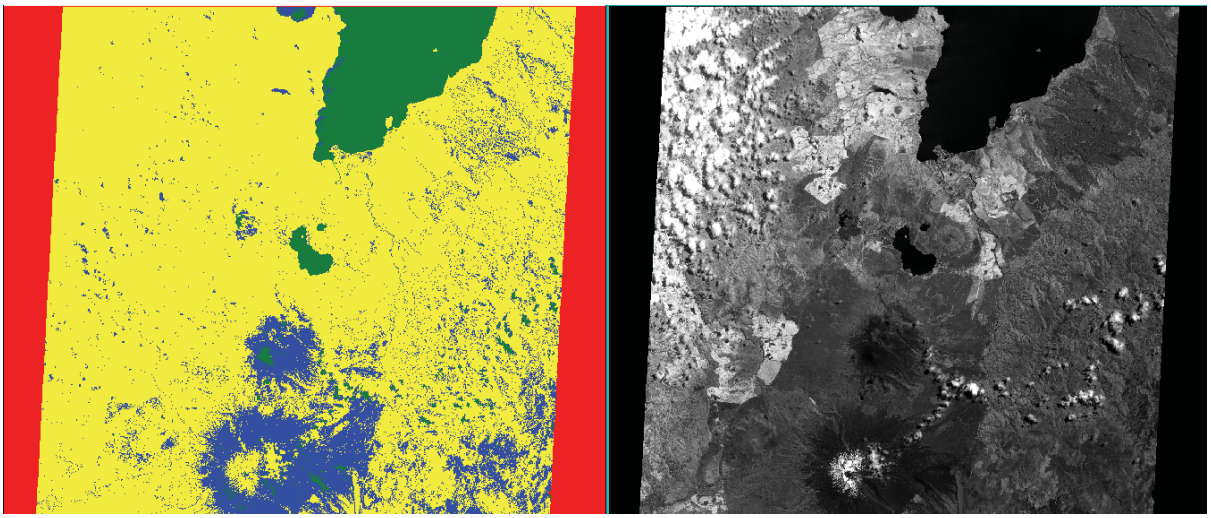

Figure 4-17: Colour slice image (A) using the parameters in Figure 4-16 and Greyscale (B) image for ASTER Band 3

4.6.3 Removal of bands containing noise

Based on the information shown in the pixel value distribution graphs (Figure 4-13) the bands with reflectance data anomalies (bands 4-7) were removed from the dataset. In doing so the spectral resolution of the remaining data is reduced to, Bands 1, 2 and 3 range from 0.52 to 0.86 µm and Bands 8 and 9 cover 2.295 to 2.430 µm. The spectral hourglass wizard was run on the remaining five bands (Bands 1,2,3,8 and 9).

4.7 Spectral Hourglass Wizard (ENVI)

The Spectral Hourglass Wizard (SHW) is a step by step processing tool is ENVI that finds spectral endmembers and maps the image accordingly.

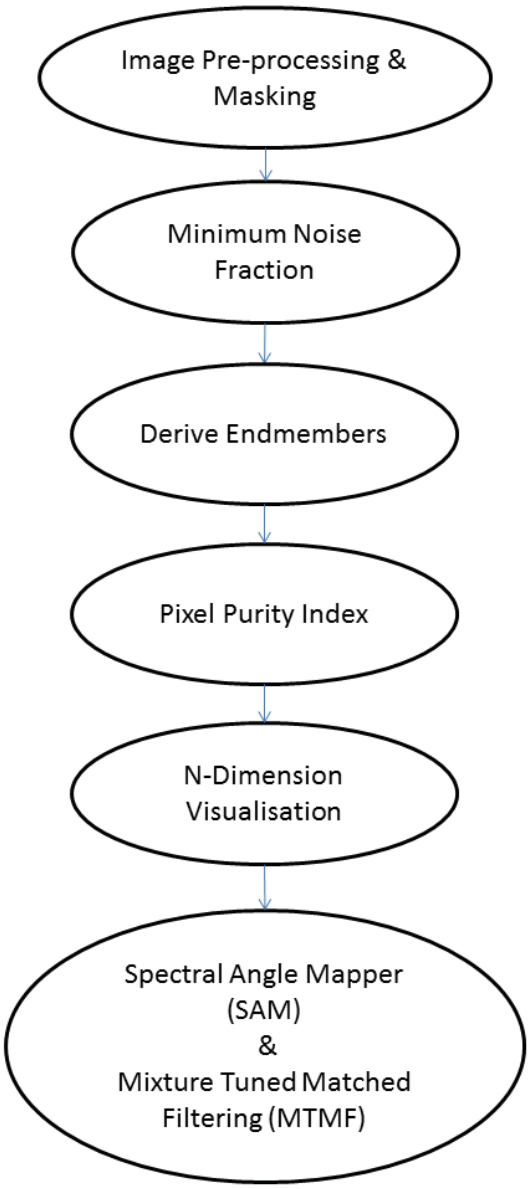

Figure 4-18: Basic flowchart of the Spectral Hourglass Wizard.

Initially the spectral hourglass wizard was run using the final masked image which had minimal vegetation, snow, clouds and water present.

4.7.1 Minimum Noise Fraction (MNF)

The first process in the SHW is the minimum noise fraction (MNF) transform. It determines the inherent dimensionality of image data, and by segregating and equalising noise the computational requirements for subsequent processing are reduced (ITTVis, 2005). The MNF ranked the 9 bands by increasing noise content. The eigenvalue plot can be used to determine which bands contain data and which contain noise. Bands with an eigenvalue

near 1 contain noise. The first band have high signal but the remaining bands all contain more noise as they are all much closer to 1 (Figure 4-20).

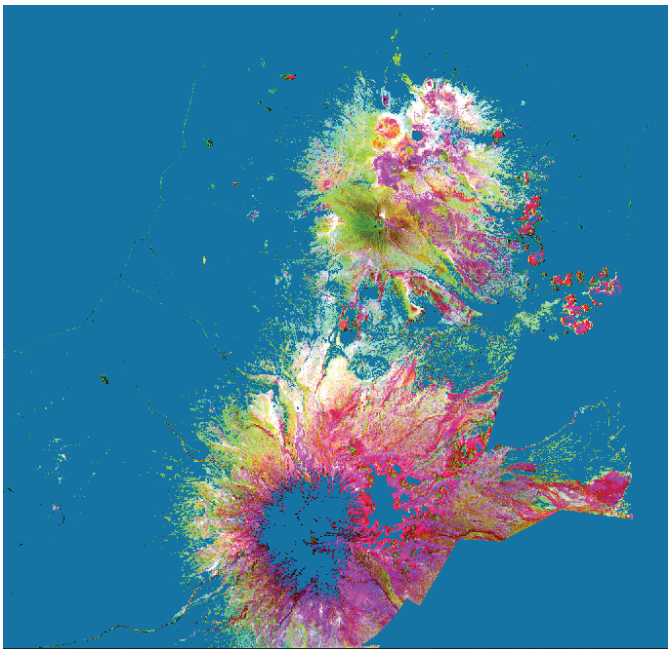

Figure 4-19 RGB display of the first 3 bands of the MNF transform for the Aster dataset.

The RGB image of the first three MNF bands is one way of quickly locating dominant spectral materials, which are displayed in bright, pure colors

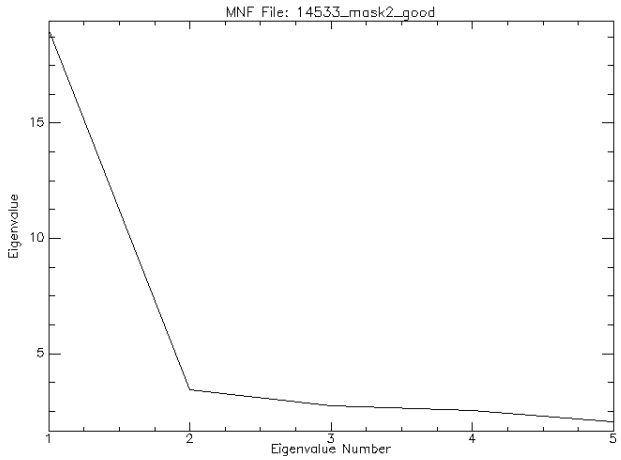

Figure 4-20: Eigenvalue plot for each transformed band

4.7.2 Spatial Coherence

Spatial Coherence is the correlation coefficient calculation between each band and a version of itself offset by one line (ITTVis, 2005). The lower ranked bands following the MNF step have spatial structure and contain mostly usable information, while the higher ranked bands contained most of the noise. By eliminating the noisy bands and retaining the bands that

contain the information, the spectral processing results can be improved. In this dataset the first 5 MNF transformed bands were above the threshold for spatial coherence, which indicates that these bands are acceptable for analysis (Figure 4-21) These bands have been transformed so they are no longer in order according to wavelength, they have been ordered according to their signal to noise ratio.

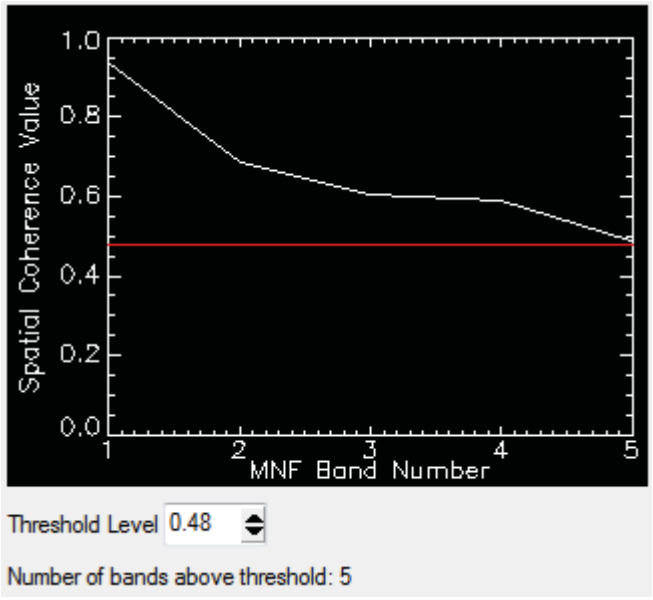

Figure 4-21: Spatial Coherence Plot of the 5 transformed bands

4.7.3 Pixel Purity Index

The pixel purity index (PPI) image is produced by repeatedly projecting n-*D* scatter plots on a random unit vector. The extreme pixels are considered to be the most spectrally pure in the image. These pure pixels are extracted as endmembers for classification (Figure 4-22).

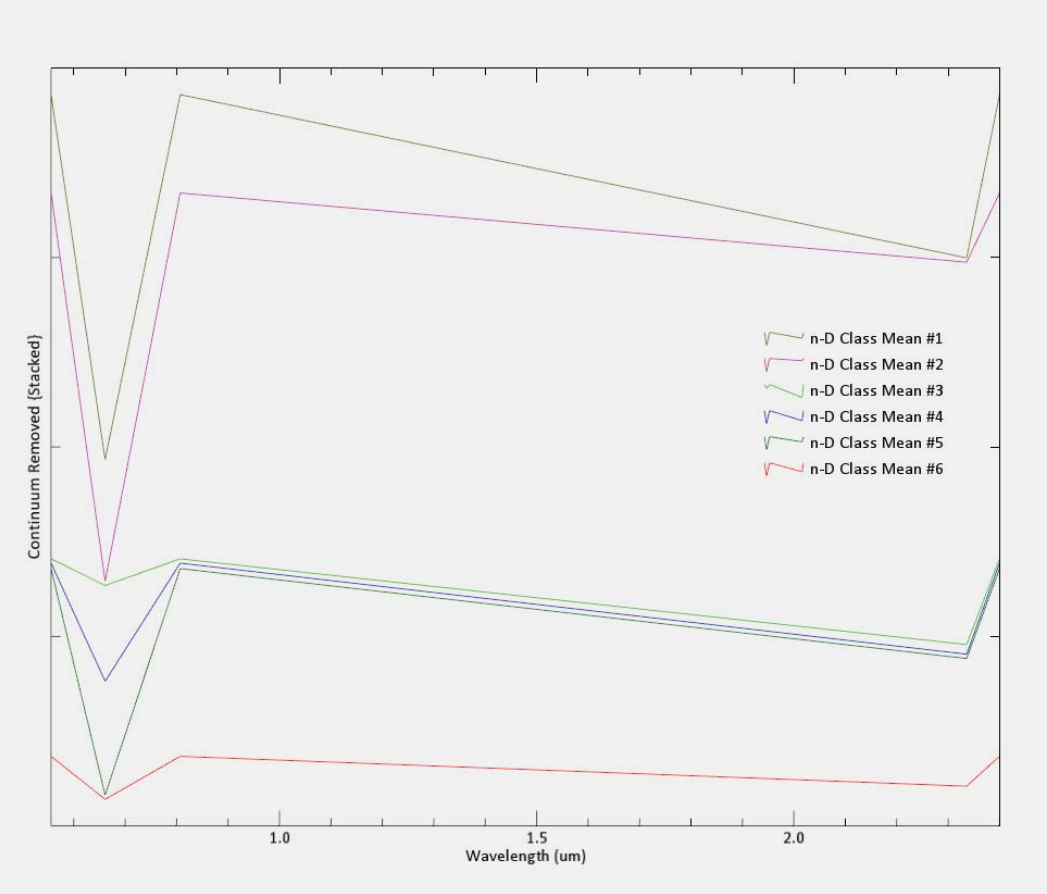

Figure 4-22 Plot of Endmembers extracted from the PPI image

After the endmembers were extracted each one was assessed using the Spectral Analyst to look for possible identification matches.

5 Results

5.1 X-Ray Diffraction

Clay minerals can be identified using the X-ray diffraction patterns looking at peak position, intensity, shape and breadth. Kaolinite has reflections based on a 7.1 Å structure while smectite has reflections at 16.9 Å (Moore and Reynolds, 1989). The aim of the XRD analysis was to identify the presence of clay minerals, not to estimate quantities. Quantity estimation is most often carried out in such studies by a method of standard addition, where the sample matrix is used, and fixed amounts of the clay mineral in question added. In this study, however, the range in potential concentrations of clay minerals varies so greatly with distance from the central areas of hydrothermal zones, it was deemed more important to concentrate on identification of key phases. In particular the mineral phases with shrinking-swelling properties, associated with instability (e.g, smectites) or, structures that hold water (e.g., Halloysite) were targeted.

Of the 22 samples collected, 20 were analysed with the XRD. The two that were not analysed included MI05-13, a basalt rock, MI05-8 which was lost in transit from the field site.

Six samples, MI05-4, MI05-5, MI05-6, MI05-7, MI06-1, MI06-2, and MI06-3 showed the presence of Kaolinite with a 1st order peak of 7Å at 14°. while four indicated the presence of smectite with first order peaks at ≈ 6° and 16.9Å.

Three samples showed the presence of smectite (MI05-11, MI05-12, and MI05-14) with a 1st order peak of 15.5Å at 6°.

Sample MI06-4 was almost entirely elemental sulphur and was not used for any further analysis.

The remaining samples analysed using XRD contained cristobalite, alunite and natro-alunite, or other non-clay minerals.

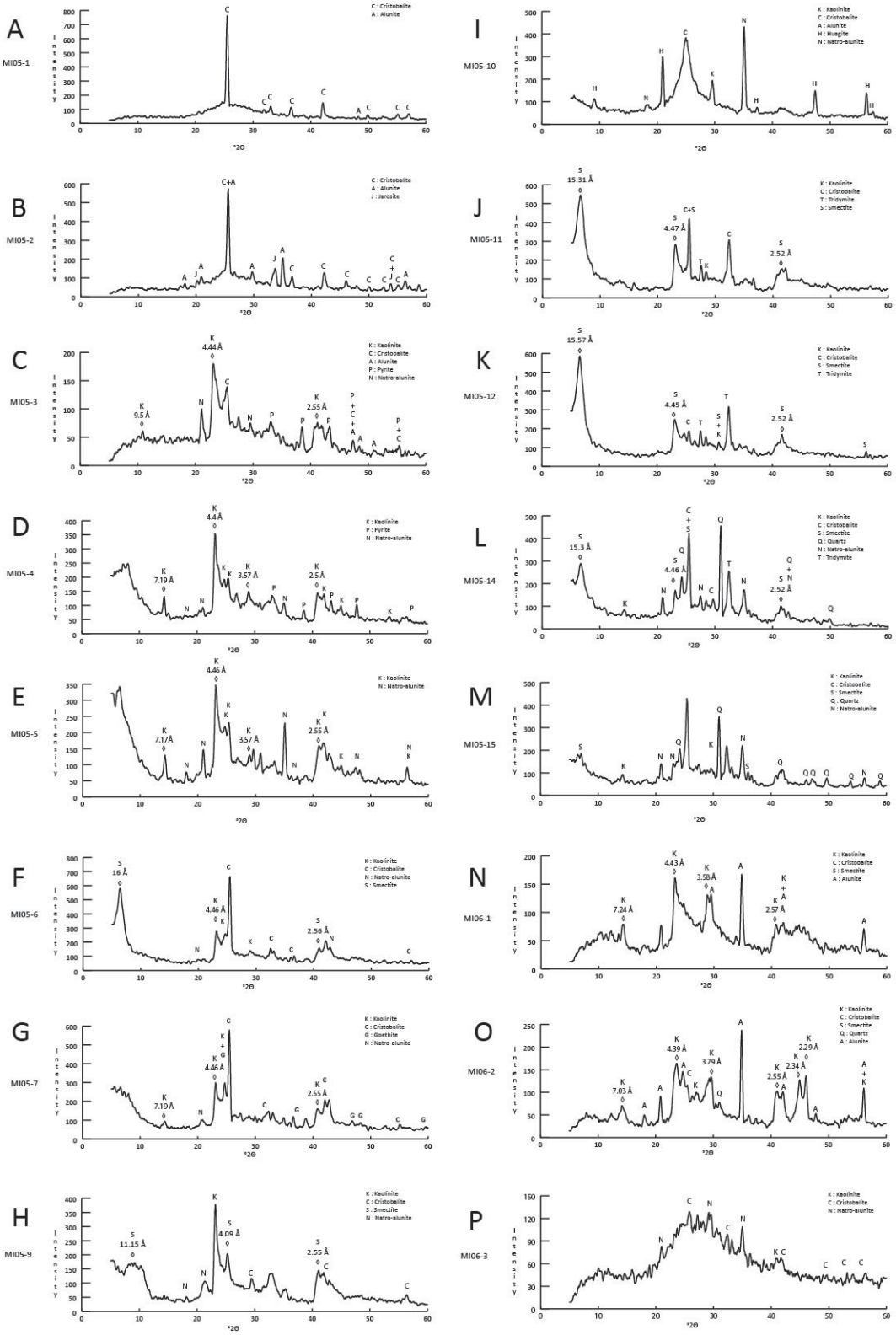

Figure 5-1 XRD scans for samples MI05-1 (A) to MI05-15(M) and MI06-1(N) to MI06-3(P), showing identified peaks and respective Angstrom units.

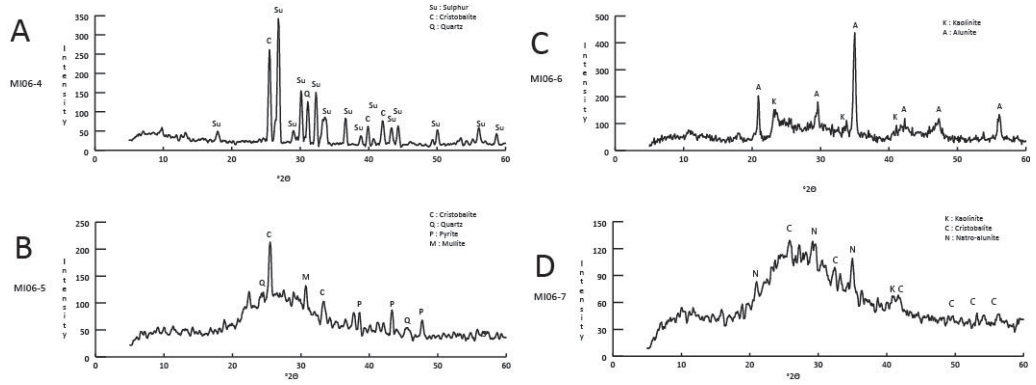

Figure 5-2 XRD scans for samples MI06-4 (A) to MI06-7(D), showing identified peaks and respective Angstrom units.

5.1.1 Smectite Identification

Two samples that represented to two types of smectite scan results were treated with glycerol to discriminate between smectite and Kaolinite. Sample MI05-5 was chosen because it displayed peaks of smectite and Kaolinite; while MI05-6 showed peaks of Smectite with no Kaolinite peak. The smectite peak shifted on both scans (Figure 5-3 and Figure 5-4) but the Kaolinite peak stayed in place on the MI05-5 sample (Figure 5-3). A peak shift after treatment confirms the presence of smectite.

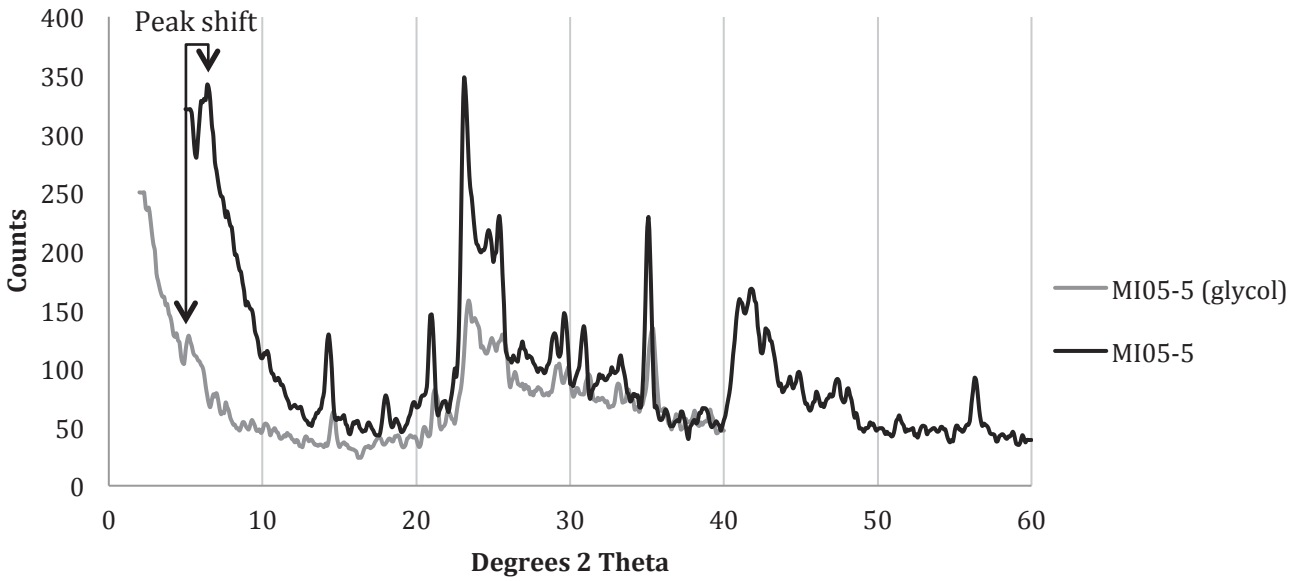

Figure 5-3 XRD scans for sample MI05-5 before and after gycol treatment.

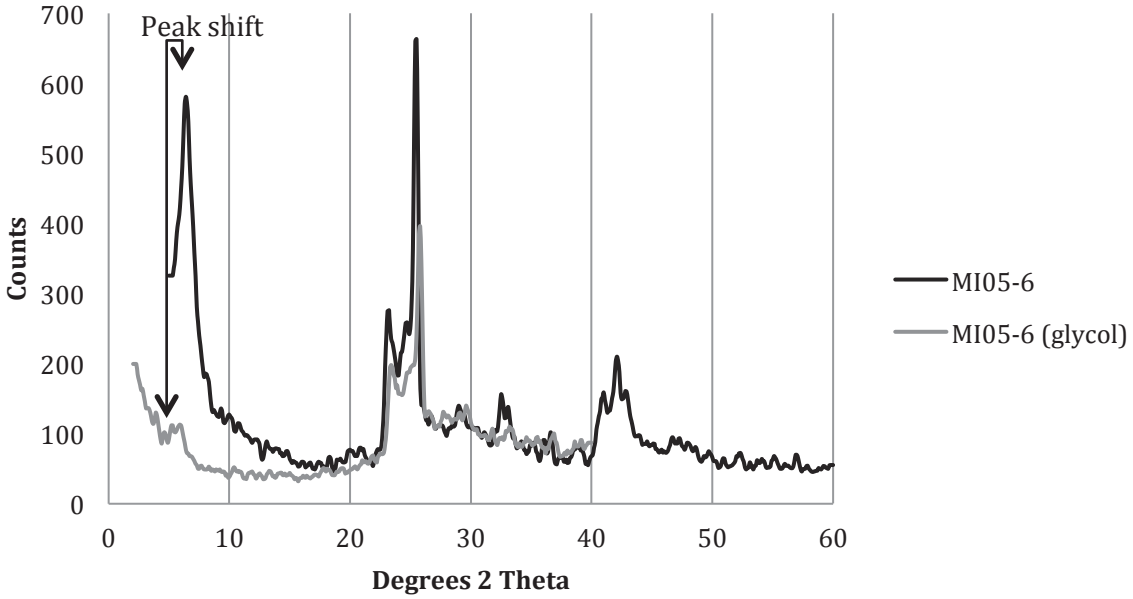

Figure 5-4 XRD Scans for MI05-6 before and after 10% Glycerol treatment

Samples with the large hump in the background (Figure 5-1) could be indicative of short-range order clay minerals such as allophane, ferrihydrite or imogolite, alternatively it could be volcanic glass. The XRD scan of volcanic glass (Hekia-4 glass and obsidian) Figure 5-5 has intensity counts of 400 to 1300 from 15 to 30 degrees 2-theta. The samples MI06-3, MI06-5, MI06-7 could all possibly contain volcanic glass. Glass can be segregated from the other constituents by preparing the sample using centrifugation of a suspension (Zehra and Selahattin 2000), but was not completed in this study.

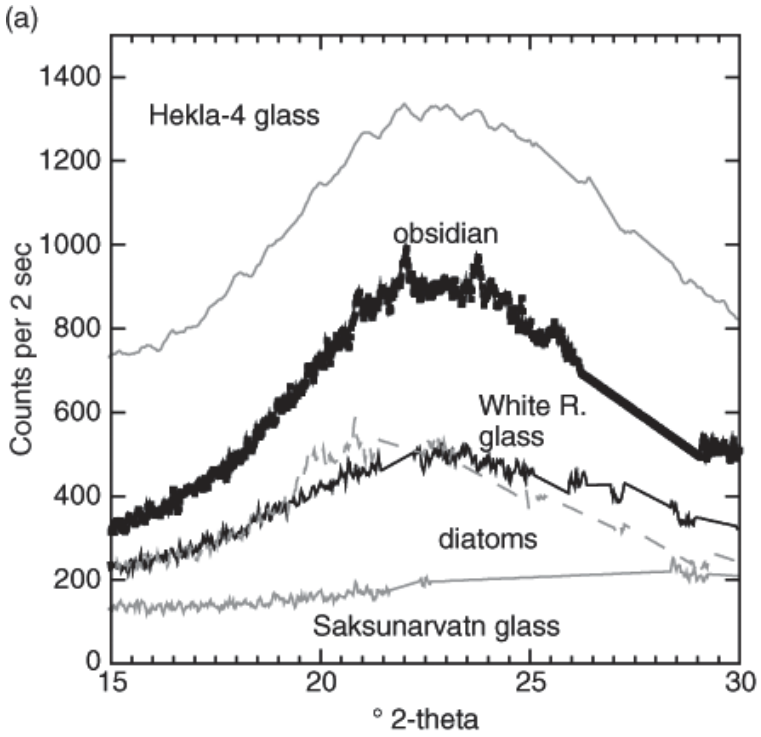

Figure 5-5 X-Ray diffraction pattern showing the characteristic hump in amorphous materials (Andrews et al 2013)

The peaks that are present for each sample in the XRD analysis are given in Table 5-1. Cristobalite, Kaolinite and Smectite feature prominently in the results. Even if there is an identification result it needs to be checked to see how strong the peak response is. Stronger peak responses would suggest the sample contains more of that mineral. XRD provides bulk identifications – or the whole scan will tell you more about the composition of the sample and the peak strength indicates the abundance in the sample.

Table 5-1 XRD identification results for the field samples

Sample	Mineralogy
MI05-1	Cristobalite, Alunite
MI05-2	Cristobalite, Alunite, Jarosite
MI05-3	Kaolinite, Cristobalite, Alunite, Pyrite, Natro-Alunite
MI05-4	Kaolinte, Pyrite, Natro-Alunite
MI05-5	Kaolinite, Natro-Alunite
MI05-6	Kaolinite, Cristobalite, Natro-Alunite, Smectite
MI05-7	Kaolinite, Cristobalite, Goethite, Natro-Alunite
MI05-9	Kaolinte, Cristobalite, Smectite, Natro-Alunite
MI05- 10	Kaolinite, Cristobalite, Alunite, Huagite, Natro-Alunite
MI05-11	Kaolinite, Cristobalite, Trdymite, Smectite
MI05-12	Kaolinite, Cristobalite, Tridymite, Smectite
MI05-14	Kaolinite, Cristobalite, Smectite, Quartz, Natro-Alunite, Tridymite
MI05-15	Kaolinite, Cristobalite, Smectite, Quartz, Natro-Alunite
MI06-1	Kaolinite, Cristobalite, Smectite, Alunite
MI06-2	Kaolinite, Cristobalite, Smectite, Quartz, Alunite
MI06-3	Kaolinite, Cristobalite, Natro-Alunite
MI06-4	Sulphur, Cristobalite, Quartz
MI06-5	Cristobalite, Quartz, Pyrite, Mullite
MI06-6	Kaolinite, Alunite

5.1.2 Kaolinite Identification

Following treatment with formamide, MI05-4, MI05-7 and MI06-2 contain only Kaolinite with only 7Å peaks and no 10Å peaks on the formamide scans (Figure 5-6 B, D, F). Samples MI05-5 and MI06-1 showed peaks at 7 and 10 Å, indicating a mix of Kaolinite and Halloysite. Sample MI05-3 shows very weak peaks at 7 and 10Å so it most likely contains a small amount of Kaolinite and Halloysite.

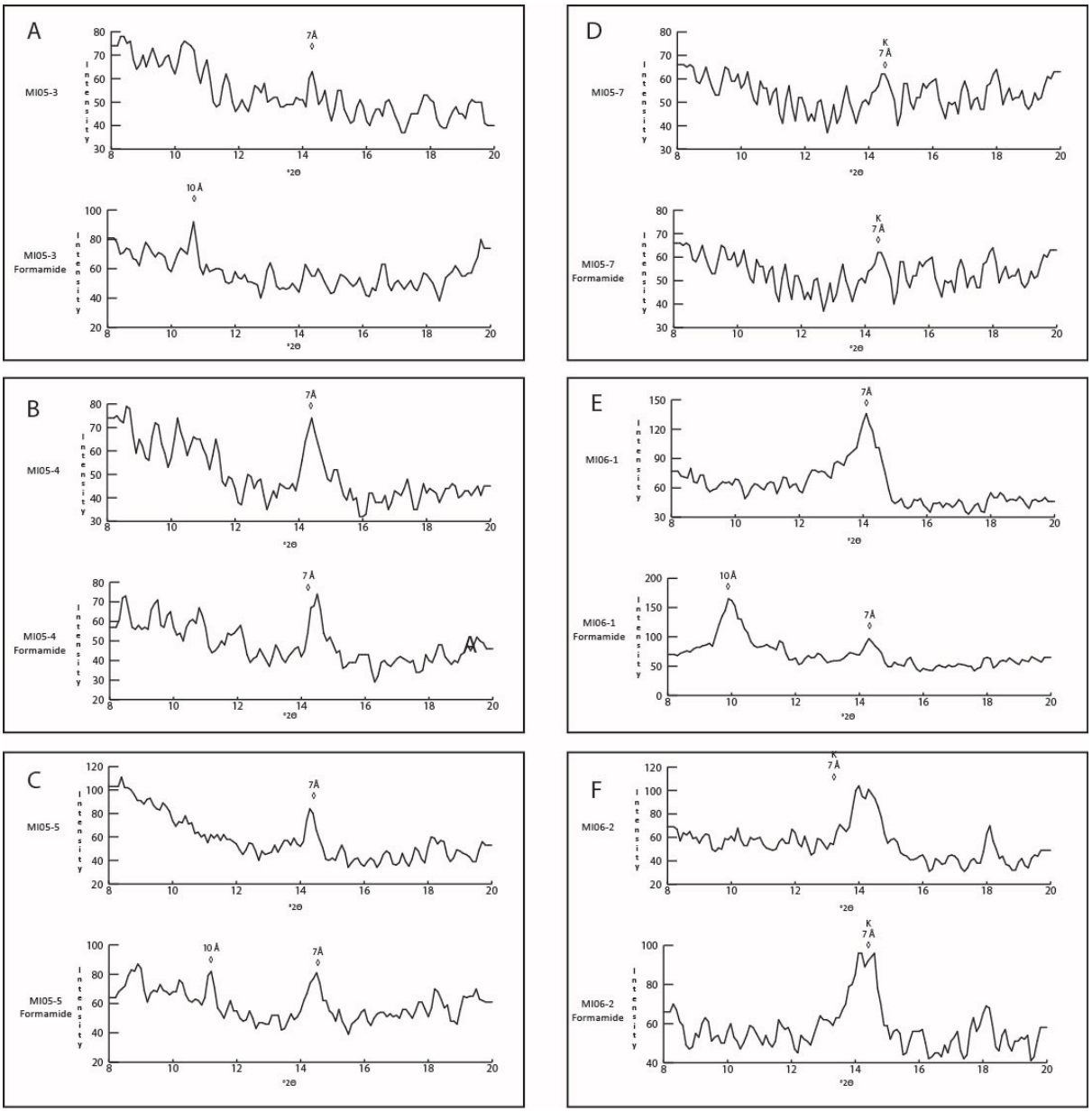

Figure 5-6 XRD scans before and after treatment with formamide on 6 selected samples to differentiate Kaolinite from halloysite.

5.2 VNIR Spectroscopy

Information from the XRD analyses and the environment where the samples were collected was used to select the most likely match from the suggested minerals in the Spectral Analyst results. The spectra collected using the spectro-radiometer for each sample was compared with the three relevant spectral libraries in ENVI (JHU, USGS and JPL) to test the robustness of the spectral analysis.

5.2.1 Example Comparison of ASD samples spectra with the JHU Spectral Library

The JHU spectral library ranges from 2.1 to 25µm and the ASD spectra reaches a maximum of 2.5µm. Only the 2.1 to 2.5µm region can be used for identification using Spectral Analyst when using the JHU spectral library. Analysis using Spectral Analyst matched 7 samples with Illite/Smectite, 7 with Kaolinite, and 6 with non-clay minerals. One sample (MI05-14) was undetermined.

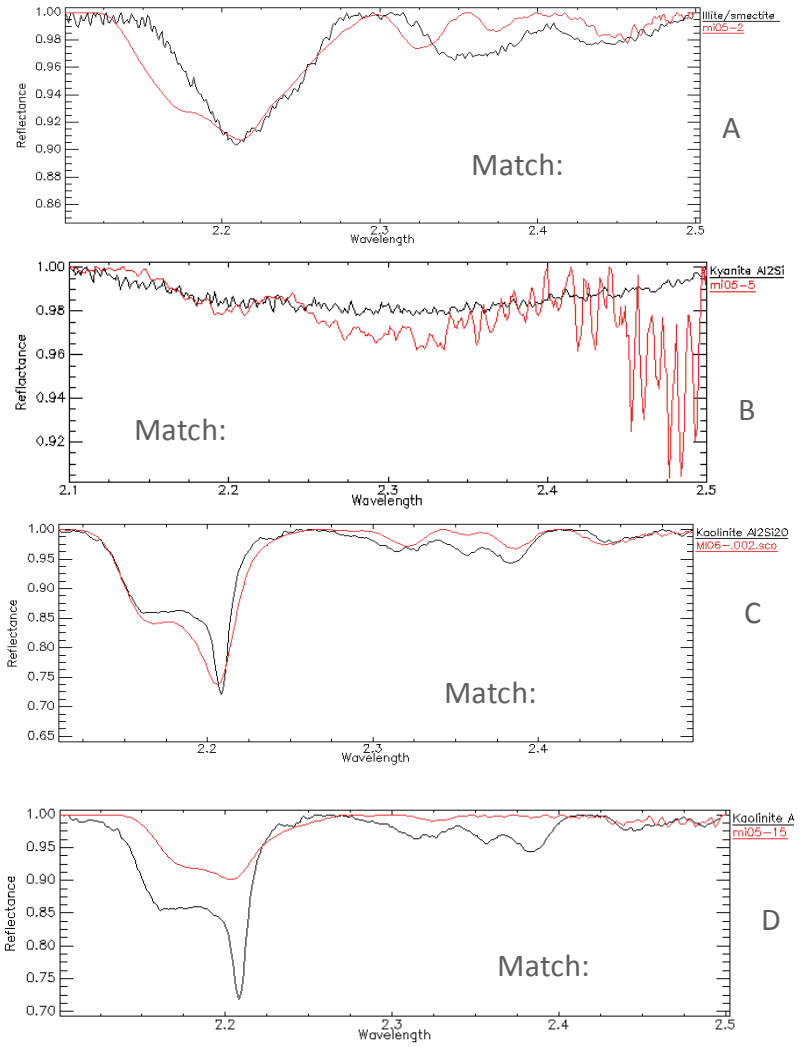

Figure 5-7 Examples of high match scores of field samples to the JHU mineral spectral library; (A) MI05-2 match Illite/Smectite, (B) MI05-5 match Kyanite, (C) MI06-2 match Kaolinite, (D) MI05-15 matched Kaolinite.

Sample MI05-2 had a good match of 0.878 for Illite/Smectite; this was confirmed visually by the similarity in the absorption at 2.2µm (Figure 5-7 A). Although the ASD spectra has a slight doublet feature which can indicate a Kaolinite mineral, there was no match as strong as the Illite/Smectite score from the spectral analyst results. Sample MI05-5 (Figure 5-7 B)

has a completely different spectral shape to the other examples in Figure 5-7 and is matched to Kyanite, which is an aluminosilicate. Sample MI05-5 is a good example of a non-clay mineral, with no absorptions at 2.2µm. Any sample that displayed no diagnostic absorptions in this range can easily be recognised as a non-clay sample. This sample is of unweathered ash or rock and may be at the early stages of alteration.

Sample MI06-2 was identified as Kaolinite with a score of 0.820 (Figure 5-7 C). One of the main diagnostic features of Kaolinite is the doublet feature at 2.2µm (Figure 5-8).

MI05-15 had high scores over all 3 spectral libraries. Against the JHU library the match score was 0.871, one of the highest matches of all samples (Figure 5-7 D).

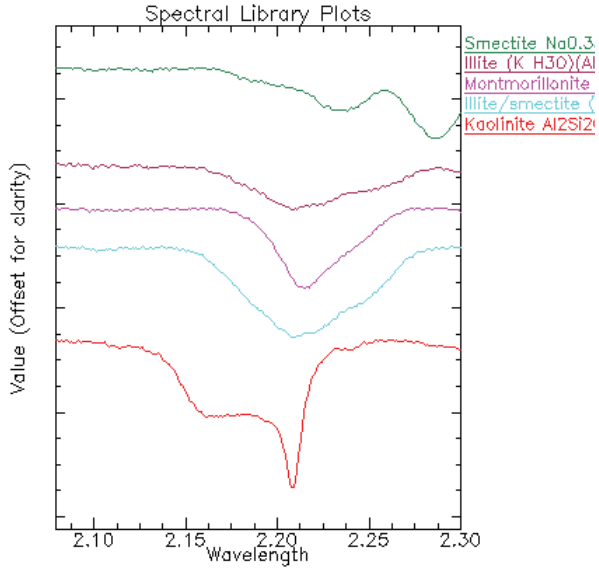

Figure 5-8 Plots of common clay minerals from the USGS Spectral Library

Figure 5-8 shows some of the common clay minerals and their differences. This highlights the Kaolinite doublet feature at 2.17-2.21µm. Montmorillonite, Illite and Smectite have a single absorption feature at 2.21µm, thus any sample that shows the doublet feature can confidently be identified as Kaolinite.

5.2.2 Comparison of samples with USGS library

The USGS Mineral spectral library has a range from 0.3951 to 2.56µm. Hydrothermally altered rocks have diagnostic absorptions from 1.4 to 2.5µm. For this reason the 1.4 to 2.5µm region is used for identification. The USGS spectral library does not include a spectra for Smectite but does contain a spectra for Kaolin/Smectite.

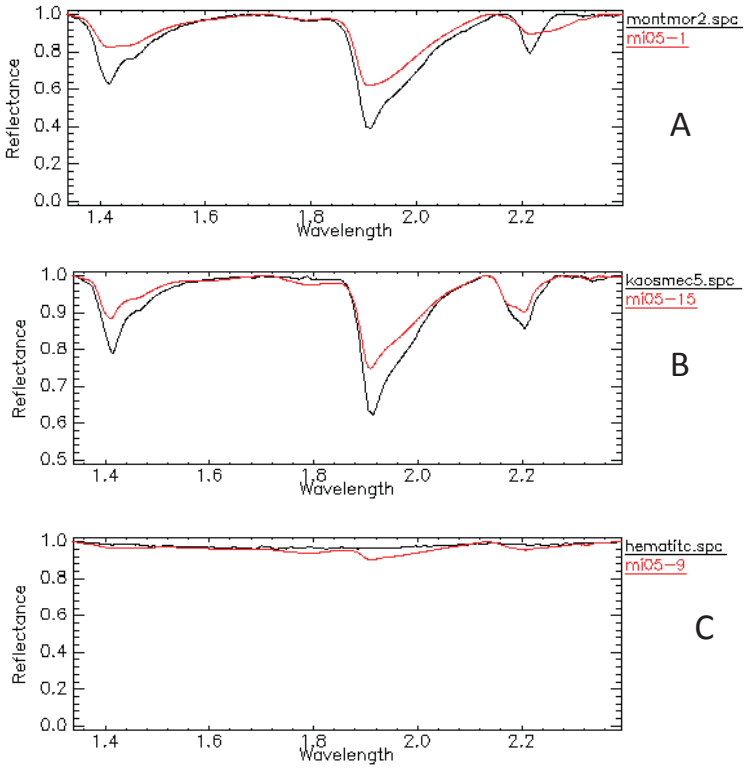

Figure 5-9 Selected samples matched with the USGS spectral library

Analysis with the USGS library matched 13 samples with Kaolin/Smectite, two with Montmorillonite and 6 as non-clay minerals. Sample MI05-1 was identified as Montmorillonite with a score of 0.773 (Figure 5-9 A). MI05-15 (Figure 5-9 B) when compared was identified as Kaolin/Smectite with a score of 0.904, and MI05-9 (Figure 5-9 C) was identified as a non-clay mineral, Hematite, scoring 0.868. These were the best visual matching/high scoring results that were supported by in situ observation.

5.2.3 Comparison of samples with JPL library

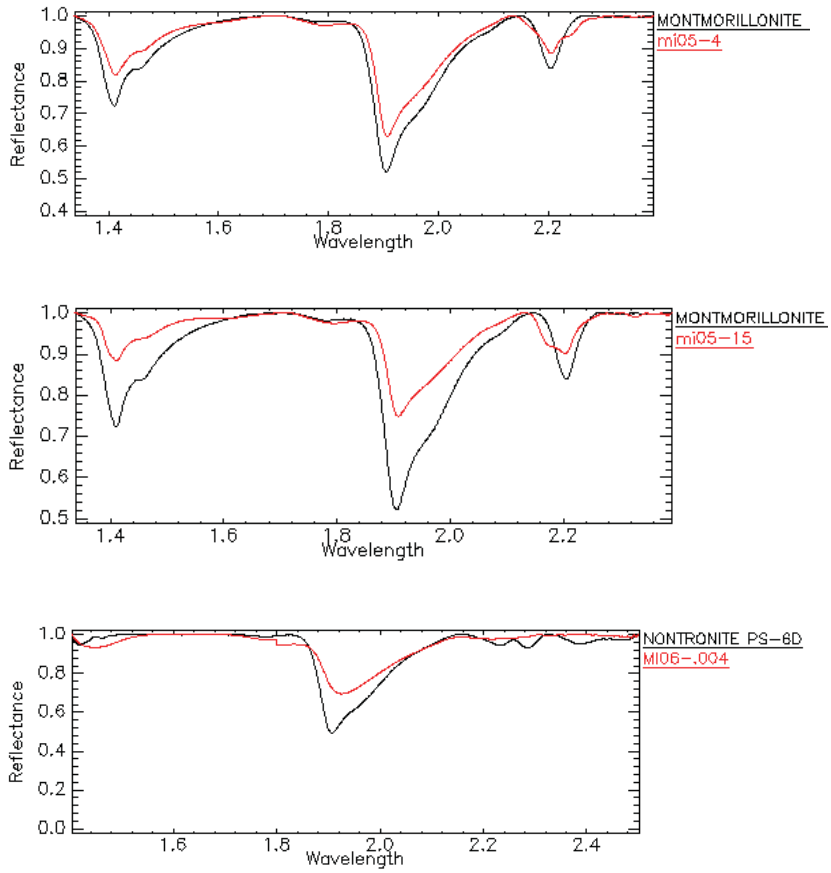

Figure 5-10 Comparison of a selection of samples to the JPL spectral library

The JPL spectral library covers the 0.4-2.5 µm range and only the 1.4 to 2.5µm region was used in the identification. The JPL library contains the spectra for 160 minerals. Identification using the JPL library found 16 samples matched with Montmorillonite, and 5 as non-clay minerals. For each sample the match score and mineral identified from each spectral library is provided in Table 5-2. # of the samples matched to a clay in all three libraries providing reasonable confidence that these samples are clay minerals.

Table 5-2 All samples with match scores and mineral identifications over the three spectral libraries

	JHU		USGS		JPL	
	Match	Mineral	Match	Mineral	Match	Mineral
MI05-1	0.745	Illite/Smectite	0.773	Montmorillonite	0.695	Montmorillonite
MI05-2	0.847	Illite/Smectite	0.839	Kaolin/Smectite	0.812	Montmorillonite
MI05-3	0.838	Illite/Smectite	0.876	Kaolin/Smectite	0.836	Montmorillonite
MI05-4	0.871	Illite/Smectite	0.862	Kaolin/Smectite	0.85	Montmorillonite
MI05-5	0.837	No Clay (Kyanite)	0.85	Hematite	0.864	Labradorite
MI05-6	0.882	Illite/Smectite	0.739	Kaolin/Smectite	0.738	Montmorillonite
MI05-7	0.878	Illite/Smectite	0.794	Kaolin/Smectite	0.781	Montmorillonite
MI05-9	0.92	Kyanite	0.868	Hematite	0.858	Hematite
MI05-10	0.779	Nepheline	0.774	Opal	0.706	Montmorillonite
MI05-11	0.866	Kaolinite	0.663	Kaolin/Smectite	0.665	Montmorillonite
MI05-12	0.859	Kaolinite	0.88	Kaolin/Smectite	0.805	Montmorillonite
MI05-14	0.8	Kaolinite	0.691	Kaolin/Smectite	0.678	Montmorillonite
MI05-15	0.871	Kaolinite	0.904	Kaolin/Smectite	0.842	Montmorillonite
MI05-16	0.776	Kaolinite	0.855	Kaolin/Smectite	0.762	Montmorillonite
MI06-1	0.839	Kaolinite	0.875	Kaolin/Smectite	0.829	Montmorillonite
MI06-2	0.82	Kaolinite	0.875	Kaolin/Smectite	0.702	Montmorillonite
MI06-3	0.971	Analcime	0.676	Heulandite	0.345	Nontronite
MI06-4	0.966	Erionite	0.865	Lamontite	0.747	Nontronite
MI06-5	0.943	Erionite	0.778	Ferrihydrite	0.733	Nontronite
MI06-6	0.785	Illite/Smectite	0.852	Kaolin/Smectite	0.78	Montmorillonite

Spectral identification graphs of all samples are in Appendix A

5.3 Satellite Data Results

5.3.1 Hyperion Atmospheric Correction

Atmospheric correction of the Hyperion dataset was required before any processing could be done. There are many different methods of correcting for the atmosphere; the FLAASH module was the best available tool in the ENVI software suite.

5.3.1.1 FLAASH Processing Results

The selection of the atmospheric model appears to be the major influence on the resulting images and the spectral profile. Natural Colour RGB images of the FLAASH processing results appear visually very similar Figure 5-11 so the spectral graphs of different targets within the image (vegetation, rock, water etc.) were checked before a result can be accepted. By clicking on many different targets within the image the resulting spectral plots from one pixel can be compared across the different FLAASH processing results such as for Mid Latitude Winter and Sub Arctic Summer atmospheric models (Figure 5-12). The pixel values have been scaled by ten thousand to make the pixel values integer values.

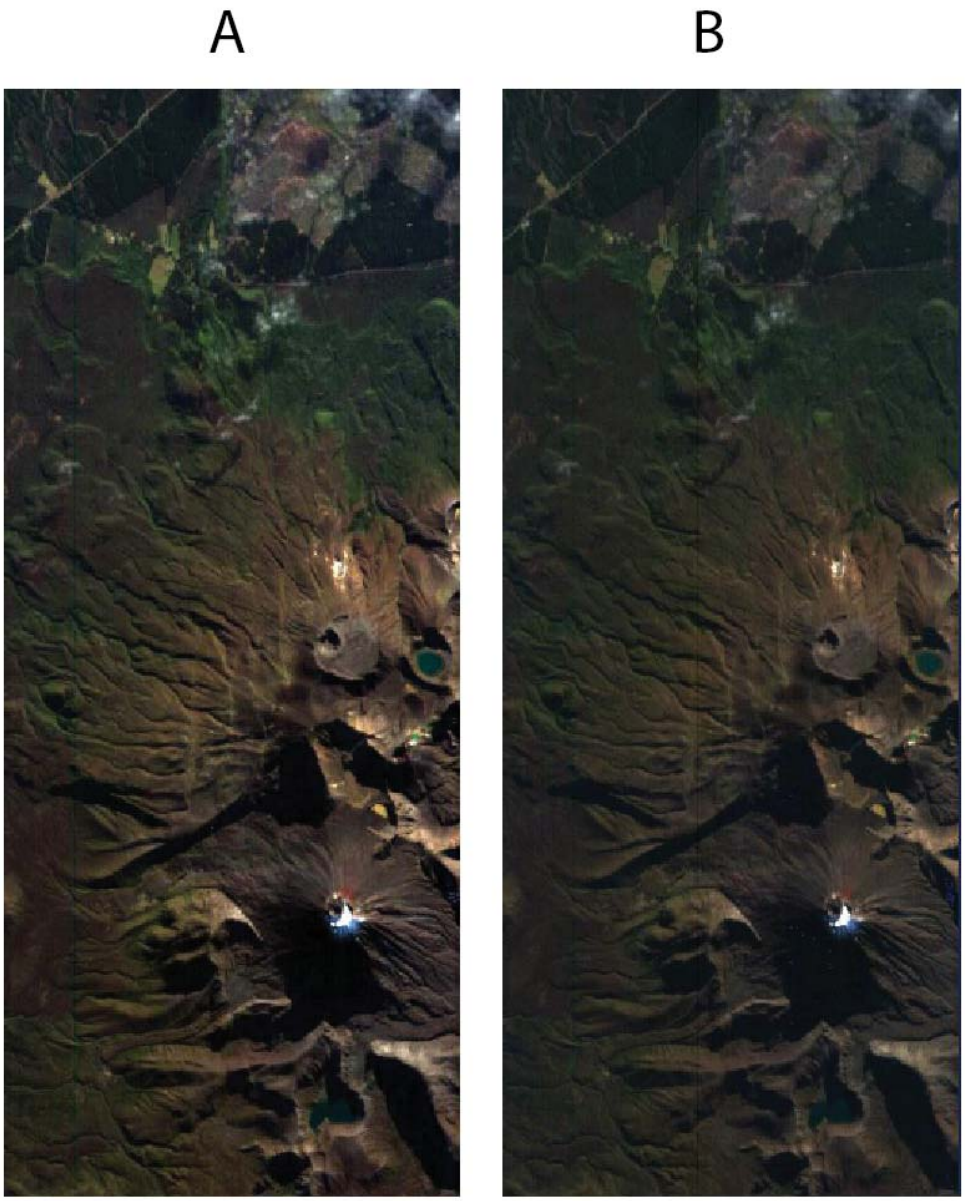

Figure 5-11 Natural colour RGB images after FLAASH processing using the Sub Arctic Summer atmospheric model (A) and the Mid Latitude Winter atmospheric model (B).

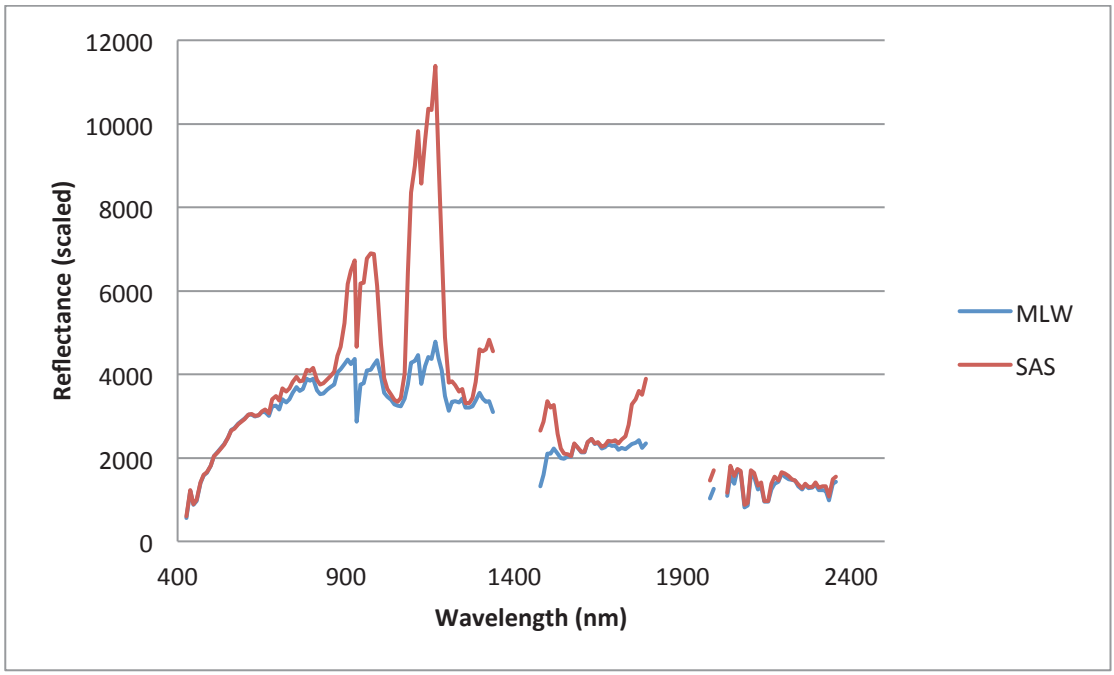

Figure 5-12 Spectral plots from one pixel (rock or bare ground) for the Mid Latitude Winter and Sub Arctic Summer atmospheric models in FLAASH

Assessment of the spectral plots would indicate that the MLW atmospheric model produced a better overall reflectance result, due to the SAS giving abnormally high results (at times greater than 10,000) from 900 to 1200nm. Both methods provide almost identical results in the region from 2000 – 2500nm, so if the data for this range was extracted for analysis either atmopsheric model would probably be acceptable.

5.3.1.2 Spectral Hourglass Wizard

Some initial attempts at classifying using the Spectral Hourglass Wizard (SHW) were run on the Hyperion data, with unsatisfactory results.

A subset of the Hyperion data was created using the bands above 2000nm to retain information relating to minerals and eliminate unwanted data (visible and near-IR vegetation bands).

After running a MNF transform on the data the bands are ordered by their increasing noise content. Physical features can only be recognised in the first two bands, the other bands are dominated by noise (Figure 5-13).

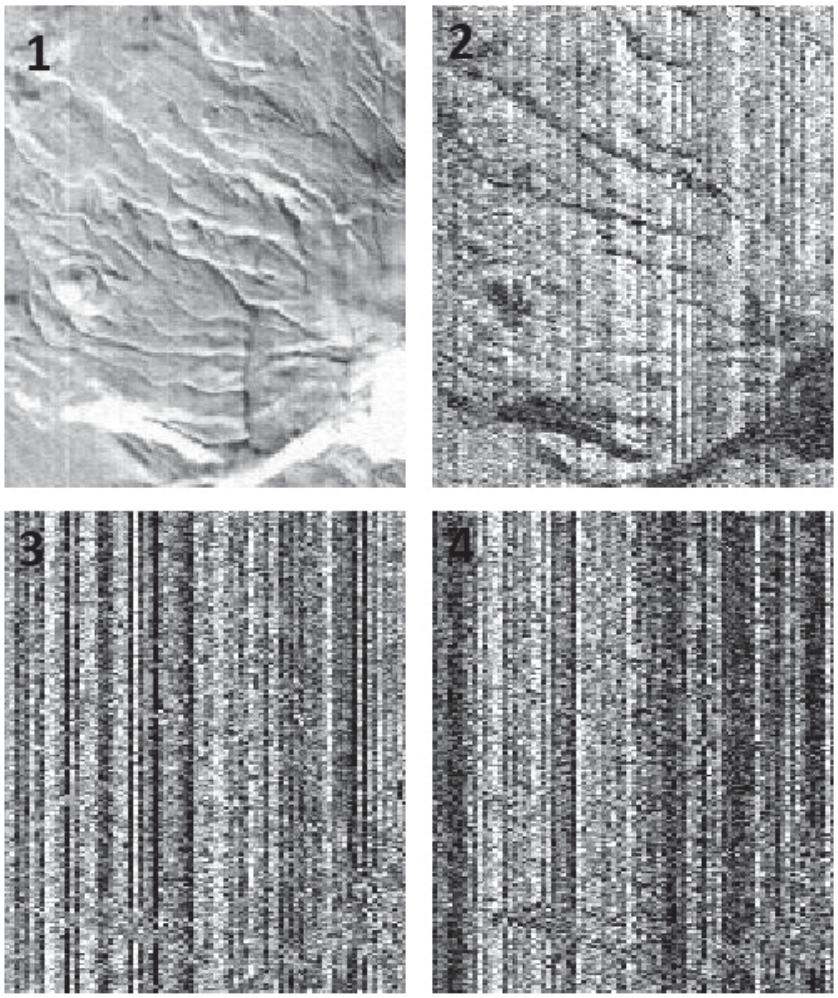

Figure 5-13 MNF Bands 1-4 showing the dominant noise in the subset above 2000nm

The noise dominated images in in the subset above 2000nm highlight why this particular Hyperion dataset is not going to produce any effective classifications results. There is only one or two non-noise dominated images and that is not enough data points for any worthwhile analysis. Hyperion imagery must be acquired under optimal conditions in order to provide useful data for mineral identification (Kruse et al., 2003).

5.3.2 ASTER Data

The Spectral Hourglass Wizard was initially run on the masked dataset with all 9 bands. The resulting classification (Figure 5-14)found no distinction in classification at Ketetahi springs or any of the other identified hydrothermal alteration zones within the Tongariro National Park boundary. This highlights the importance of removing bands with excessive noise from the analysis. The red zones shown in Figure 5-14 may represent a broad identification unit,

but overall this analysis did not help to identify any hydrothermal zones. As this was not a usefull classification no identifications of the endmembers was attempted.

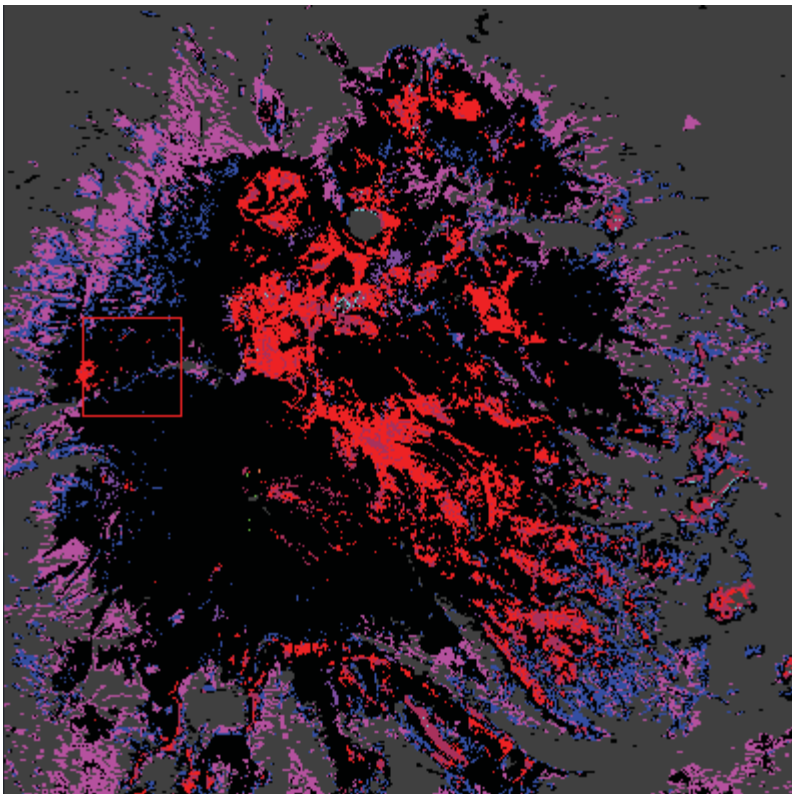

Figure 5-14: Spectral Angle Mapper classification result using the 9 ASTER VNIR and SWIR bands, each colour represents an identified end-member derived from the data.

The spectral hourglass workflow was run on a new Aster dataset with the noise dominated bands removed.

5.3.2.1 PPI Image endmembers

The Pixel Purity Index module examines the dataset and finds the purest pixels and assigns them as endmembers (Figure 5-15). The endmembers were then examined using the Spectral Analyst tool to find the best match from a spectral library (Table 5-3).

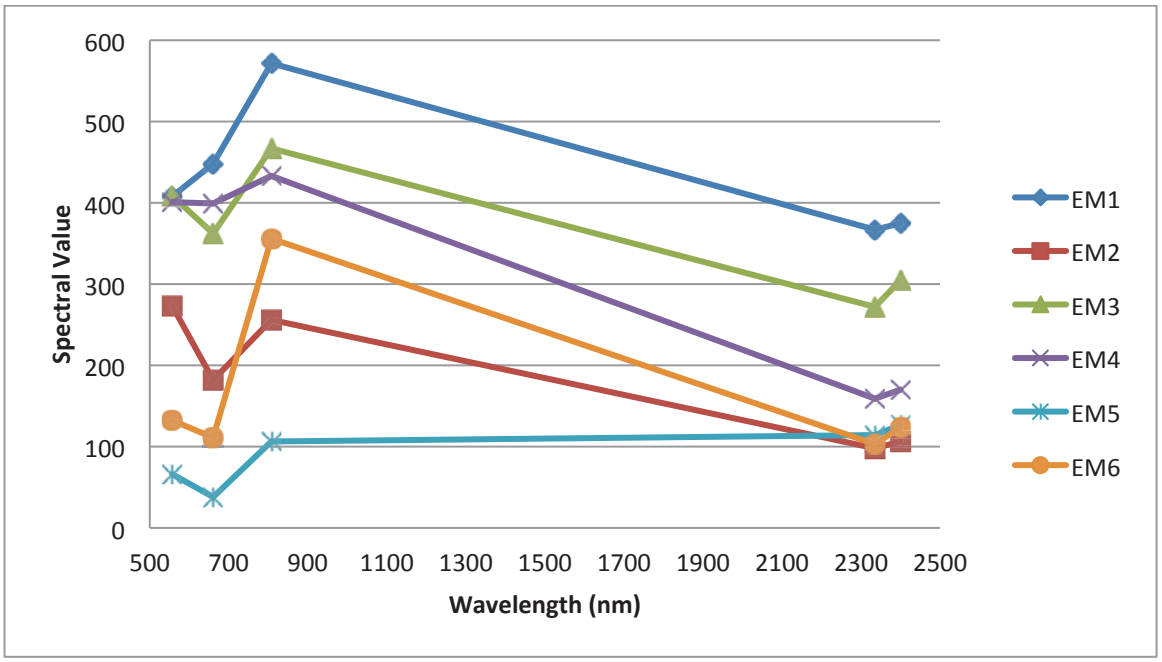

Figure 5-15: Pixel Purity Index Endmembers extracted from the ASTER dataset

Table 5-3 Mineral match and match score with the USGS spectral library for 6 Pixel Purity Index Endmembers extracted from an ASTER image of Tongariro National Park

Endmember	USGS Match	Match Score
1	Antigorite	0.947
2	Sphalerite	0.987
3	Glaucophane	0.786
4	Ilmenite	0.977
5	Prochlorite	0.863
6	Kerogen	0.667

Ilmenite is a titanium-iron oxide mineral ($FeTiO_3$) and is commonly recognised in hydrothermally altered igneous rocks. Because there are only 5 data points for each endmember, and only two of those being in the 2.0-2.5µm wavelength range, any classification is going to be limited. The ability to distinguish individual minerals is poor.

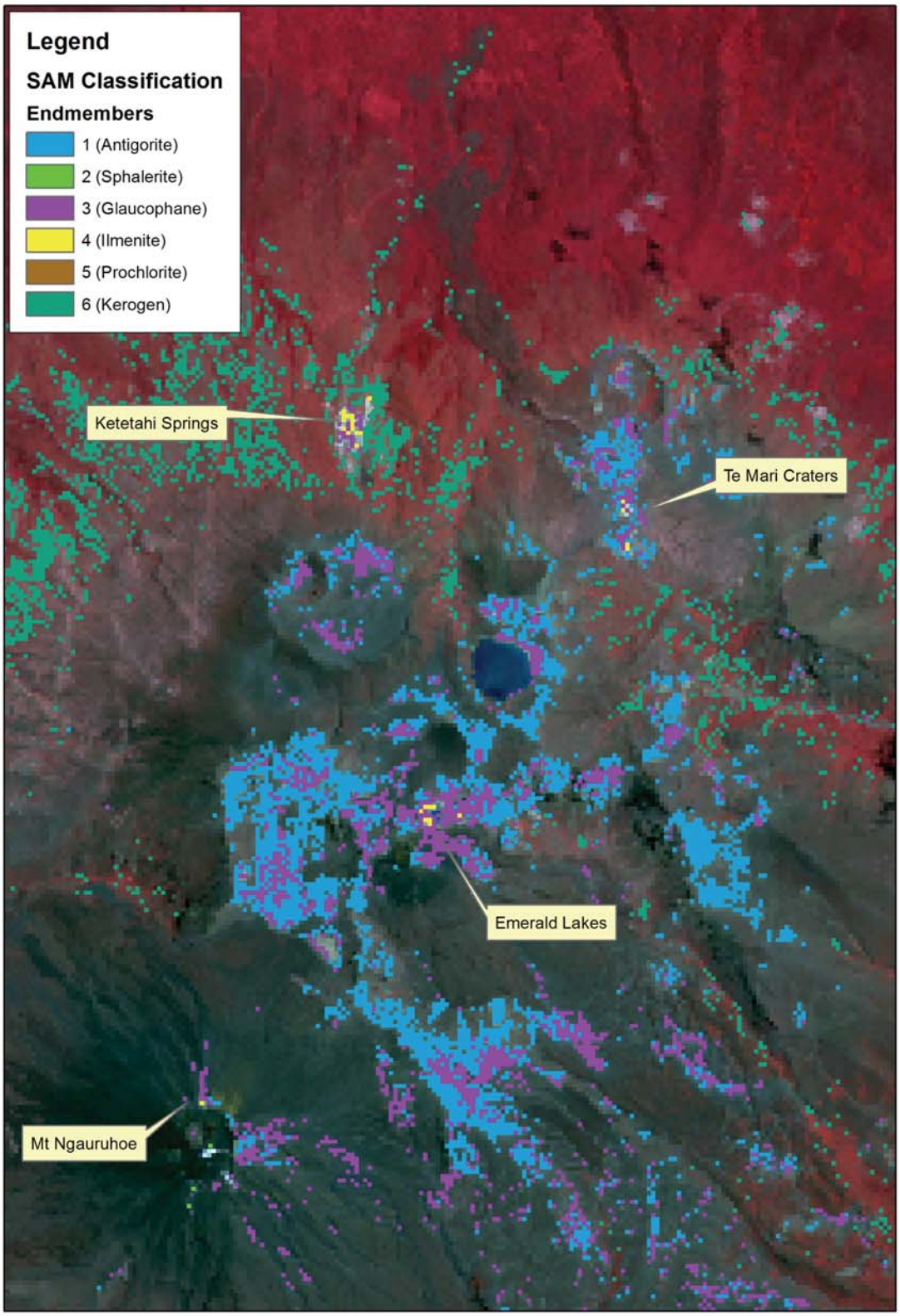

Figure 5-16: ASTER SAM classification result using non noise dominated bands displayed over the false colour ASTER image.

Four zones matching spectral endmember 4 were identified (Figure 5-16). The locations matched extremely well with the ground mapped areas of three known active hydrothermal zones (Ketetahi Springs, Emerald Lakes and the summit of Mt Ngauruhoe; Figure 5-17) and (at the time of this analysis) one non-active zone (Te Maari Craters). Given these results it can confidently be assumed that endmember 4 represents areas of hydrothermally altered materials; Ilmenite is an iron-titanium oxide and can be associated with hydrothermal conditions.

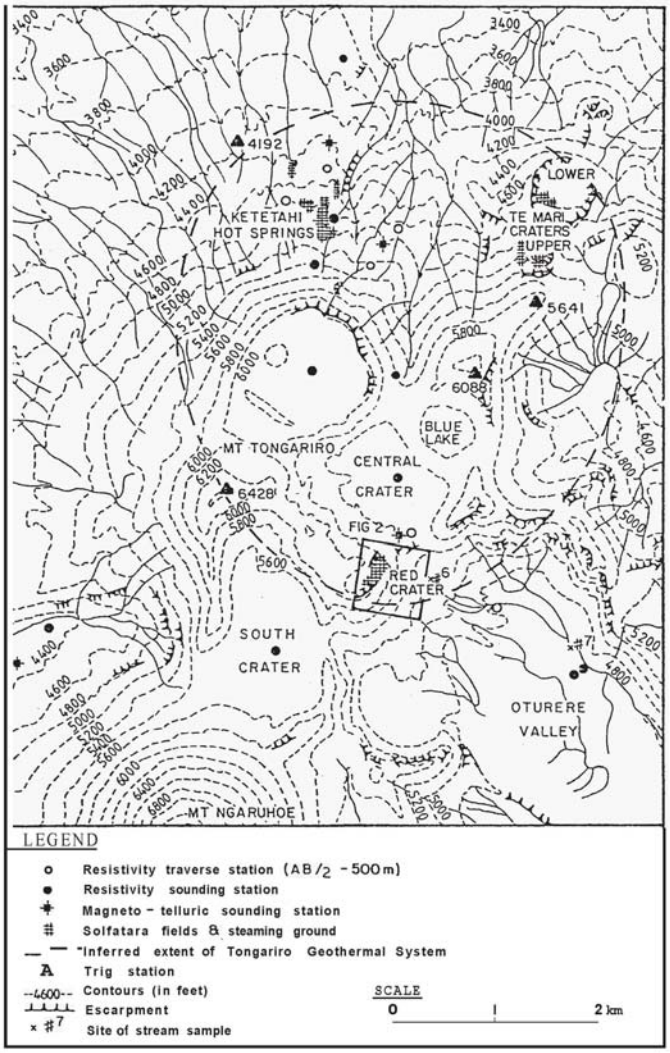

Figure 5-17 Topographic map of Mt Tongariro showing the locality of the thermal areas at Ketetahi, Red Crater and Te Maari (Hochstein, 1985).

Endmember 6 which was identified as Kerogen matches areas of altitude associated vegetation change, is more likely to be an incorrect identification, it also has a poor match score of 0.667. There are also a number of these pixels around the masked snow line on Mt

Ruapehu (Endmember 6), these are more likely to be identification errors associated with the snow line/masked area rather than actual hydrothermal zones.

Endmember 1 was identified as Antigorite, which is part of the Serpentine group, and Endmember 3 was matched with Glaucophane which is a sodic amphibole. Endmembers 1 and 3 could be associated with Andesite a family of fine-grained extrusive igneous, volcanic rock, intermediate in composition between rhyolite and basalt.

6 Discussion

6.1 Volcano Stability

One new and three known areas of hydrothermal alteration products were identified from the satellite analysis. The small number of data points per pixel available for identification from the Aster imagery used in this study combined with the low/ poor? signal/noise ratio was not sufficient to make specific mineral identifications, instead basic assemblages can be inferred. In addition, the limitations of the Aster image did not enable identification of any smaller areas of alteration. There may be alteration zones that are much smaller than the 15x15m pixel resolution of the Aster image. The reflectance of small areas of alteration would not be above a minimum threshold for data to be present and even spectral/pixel unmixing may not provide anymore information. If there are any smaller zones of alteration the response from the clays is too low or it is being masked by the surrounding rocks and cannot be identified using the resolution of the satellite imagery.

Slope angle is an important factor in volcano collapse (Voight and Elsworth, 1997). Subsidence or uplift may contribute to instability if an ediface is on a sloping or clay rich (weak) substrate (McGuire 2003). With the exception of the alteration on Mt Ngauruhoe, the zones of hydrothermal alteration that were identified are situated on the steeper slopes of the volcano (~21° – Figure 6-1). The slope data in Figure 6-1have been classified using the Jenks' Natural Breaks algorithm, which calculates the break values using the natural groupings inherent in the data. The location of hydrothermal alteration is at or near a slope class change which may mean the material above this point could fail.

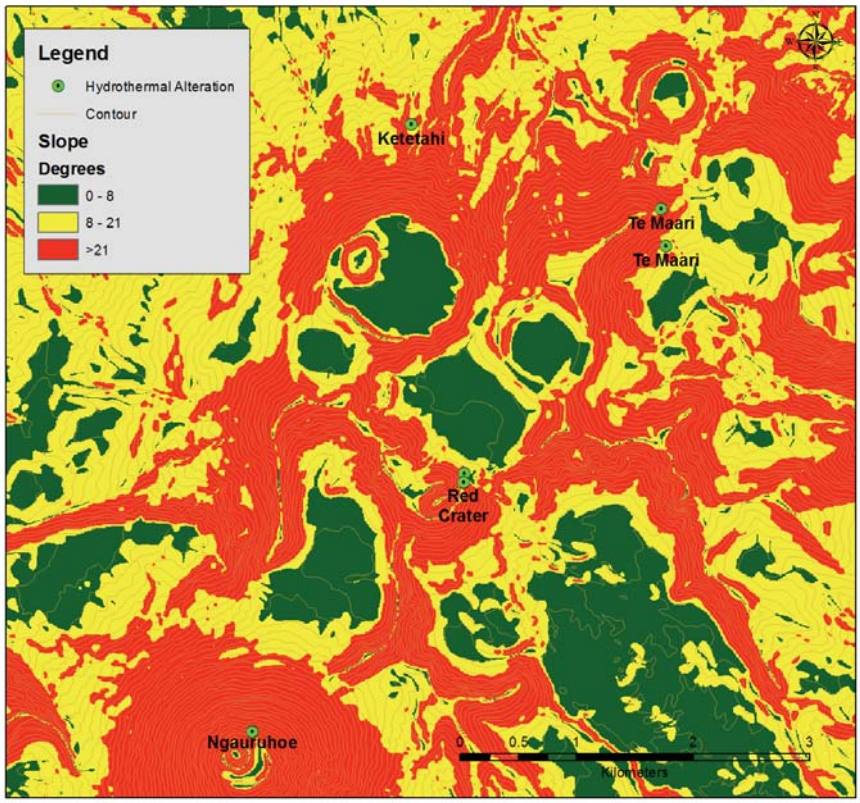

Figure 6-1 Tongariro slope map and locations of hydrothermal alteration identified from the spectral analysis.

Also of interest is the proximity of each identified alteration zone to the boundary of the geological units on which they are located according to the QMAP geological map of New Zealand (Figure 6-2). All the hydrothermal alteration areas, except for those at Red Crater, are very close to the geological unit boundaries suggesting the hydrothermal alteration is related to a contact zone between two geological units. This means that the whole contact zone could be hydrothermally altered, not just what is visible on the surface, providing a suitable surface contact with low shear strength that could facilitate a unit failure in these areas

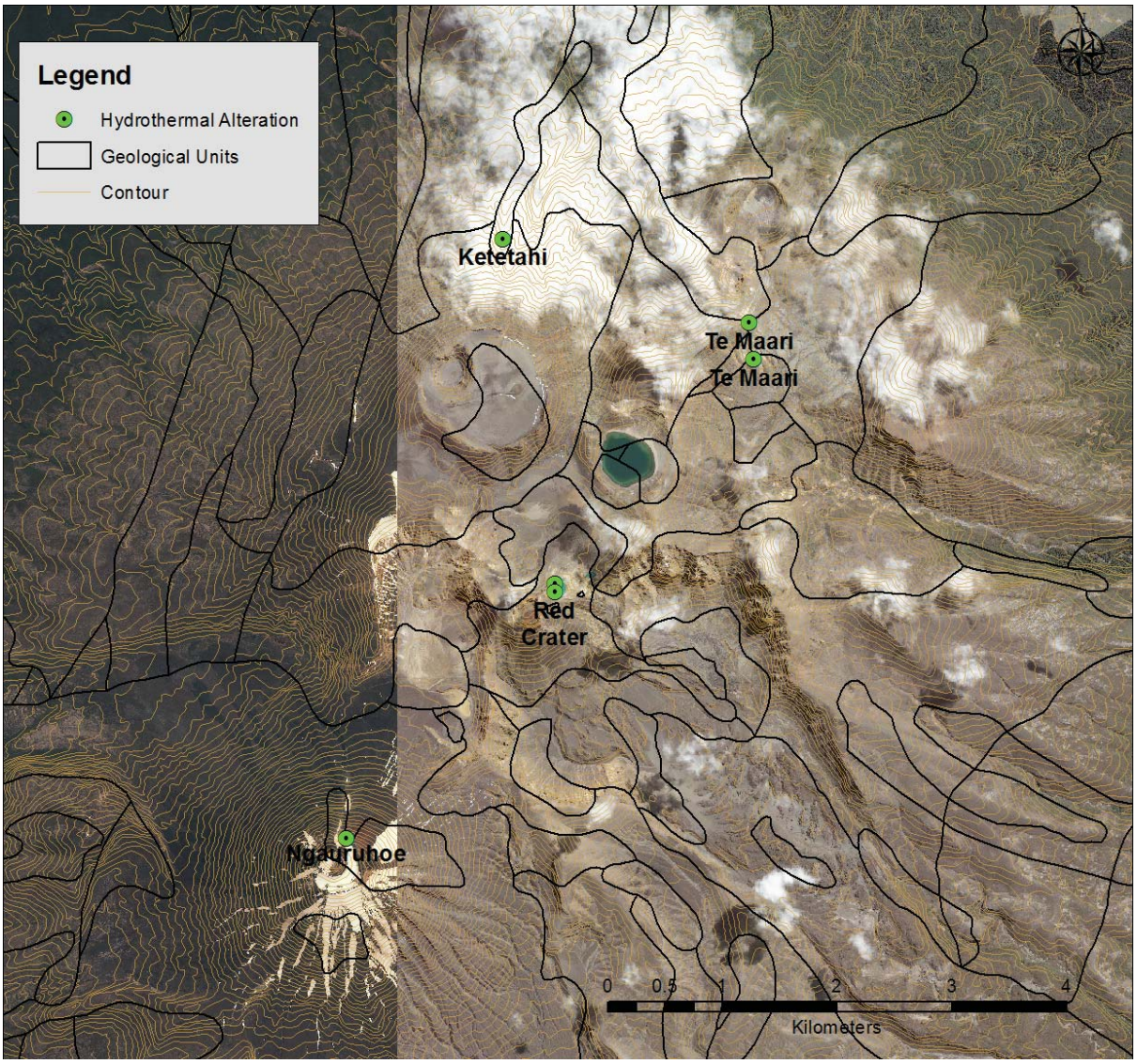

Figure 6-2 Location of identified alteration products and the geological unit boundaries.

Volcanic instability or lateral collapse is typically triggered by a dynamic event such as the intrusion of magma or by volcanic or tectonic earthquakes (McGuire, 2003). The distances that a failure may travel can vary from tens of metres from a minor rockfall to several hundreds of kilometres from gigantic debris avalanches (McGuire 2003). In New Zealand, at Mt Taranaki, the Pungarehu formation with a volume of 0.35 km^3 had a runout of 31 km (McGuire 2003). The identification of the Te Maari craters hydrothermal alteration was a major success for the satellite analysis methods. Being able to identify a clay rich/structurally weak area on the flank of a volcano is the ultimate goal for this type of analysis. Identification of this area prior to Te Maari crater eruption of 2012 shows that remote sensing has an important role to play for hazard mapping both in identification of unknown hydrothermal alteration zones and estimation of the potential impact of a failure

through the volume of material above the Te Maari Craters alteration site could be calculated using GIS.

In the journal article by Hochstien (Hochstein, 1985), it was suggested that Ketetahi springs was a low energy system and also not related to any of the other activity on the volcano so there is little risk of this area causing a major slope failure.

6.2 Hyperion/ASTER

The biggest constraints when attempting to identify hydrothermally altered zones on a volcano using remotely sensed images is the signal to noise ratio of the dataset, identifying spectral properties that correlate to rock-alteration products, and the resolution of the imagery. Initially data from EO-1's Hyperion sensor was considered for this study, because it is a satellite-based hyperspectral sensor, with a range from 400 to 2500 nm and a spatial resolution of 30m. However, EO-1 only passes over New Zealand every 16 days and always in the early morning, resulting in a very low sun-angle and a poor signal to noise ratio (SNR). Some classification and analysis was attempted on the Hyperion data but the results were unsatisfactory primarily because the wavelength bands required for mineral analysis (2000 – 2500 nm) were dominated by noise. These findings concur with the work of (Kruse et al., 2002) which concluded that Hyperion data collected under sub-optimum conditions have marginal SNR and allow only the most basic mineral occurrences and mineral differences to the mapped.

The ASTER sensor on the Terra satellite provides another freely available dataset that contains wavelength bands that can be used for mineral identification. Following data masking and processing a classification successfully identified locations of hydrothermal alteration. Three locations are known active areas of vigorous hydrothermal activity, but the fourth location was at Te Maari craters, where very little surface hydrothermal alteration was visible (Hochstein, 1985). This area had no volcanic activity when the ASTER dataset was acquired (January 12th, 2001). The identified hydrothermal zone is in close proximity to the Te Maari crater eruption of 2012, and was likely to have been triggered by a landslide from the hydrothermal area (Procter et al., 2014). Given this success in identifying weak/susceptible areas on the volcano, further development of this method is suggested. This could involve acquiring imagery from different years and analysing for changes in the areas of alteration over time. In addition, examining the use of newer, higher spectral and

spatial resolution datasets has considerable potential for greater success in identification of smaller surface areas of hydrothermal activity that may signal larger buried regions.

6.3 XRD

XRD is a traditional method for geologists to identify minerals with a crystaline structure. Clays are platy minerals that only give a “soft” response in XRD analysis, in contrast to sharp peaks such as those generated by quartz or cristobalite. A number of the samples collected and analysed from Mt Tongariro contained cristobalite and other crystalline phases such as feldspar and pyroxene. These mineral phases may have masked responses from the clay minerals present, especially if clay contents were low. A good example of this is MI05-1 (cristobalite) and MI05-3 (Kaolinite) in Figure 6-3

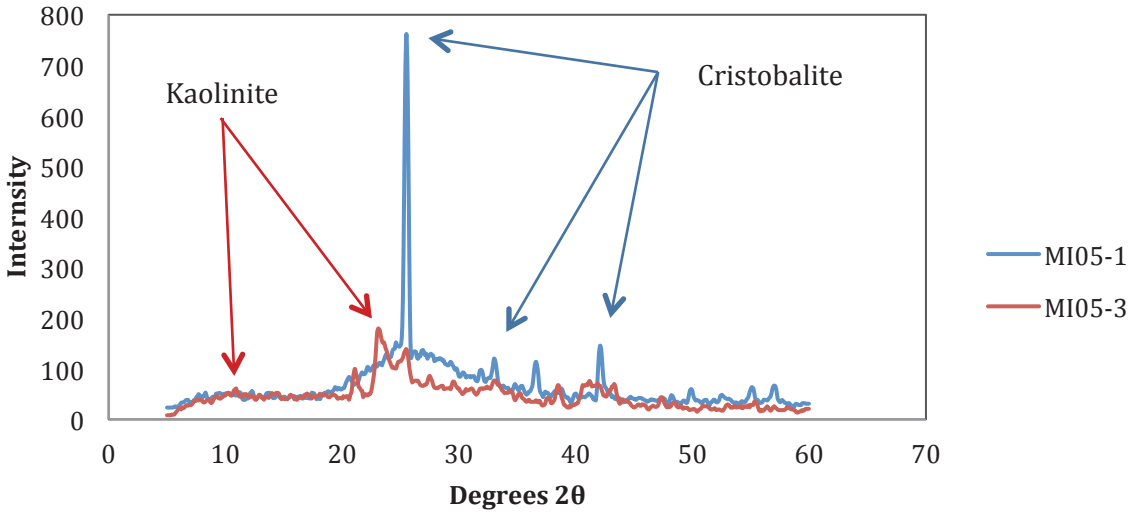

Figure 6-3 XRD Scans of MI05-1 and MI05-2

The maximum intensity of the cristobalite peak is around 800 counts, whereas the scans that showed a good clay response only registered a peak response of 200 counts. It is possible that the cristobalite present in some samples could be masking the clay mineral response and this may explain why there are some identification discrepancies between the XRD and the spectral analysis results. If larger field samples had been acquired further processing could have be carried out to separate the clay using a centrifuge or using a settling/flocculation method. However, even with these additional processing methods cristobalite can be very difficult to separate from the clay-sized particles as is the case with

halloysite clay. It is suggested that larger field samples are collected in any future work that is conducted so that this further processing can be carried out when required.

6.4 Spectroscopy

Spectroscopy provides a fast and simple method for identifying minerals. However, a natural samples are often mixtures of minerals rather than pure specimens making mineral identification problematic. In these situations it is necessary to have data from another analysis method (XRD) and a prior knowledge of the area. Having prior knowledge of what minerals are expected is essential to a successful identification. Also, the identification of minerals is limited by the number and relevance of samples in the spectral library. If the spectral library does not contain the correct mineral then the analysis will match the unknown spectra to the best option that can be found in the spectral library. It is therefore important to have a spectral library that contains relevant minerals for the study area. Taking measurements in sunlight introduces a lot of interference from the atmosphere which adds to the processing time. For that reason it was decided to analyse the samples in the laboratory environment where the best spectral response could be recorded. This does not mean that field measurements made in sunlight are not possible, but that could be the next step to extend this research.

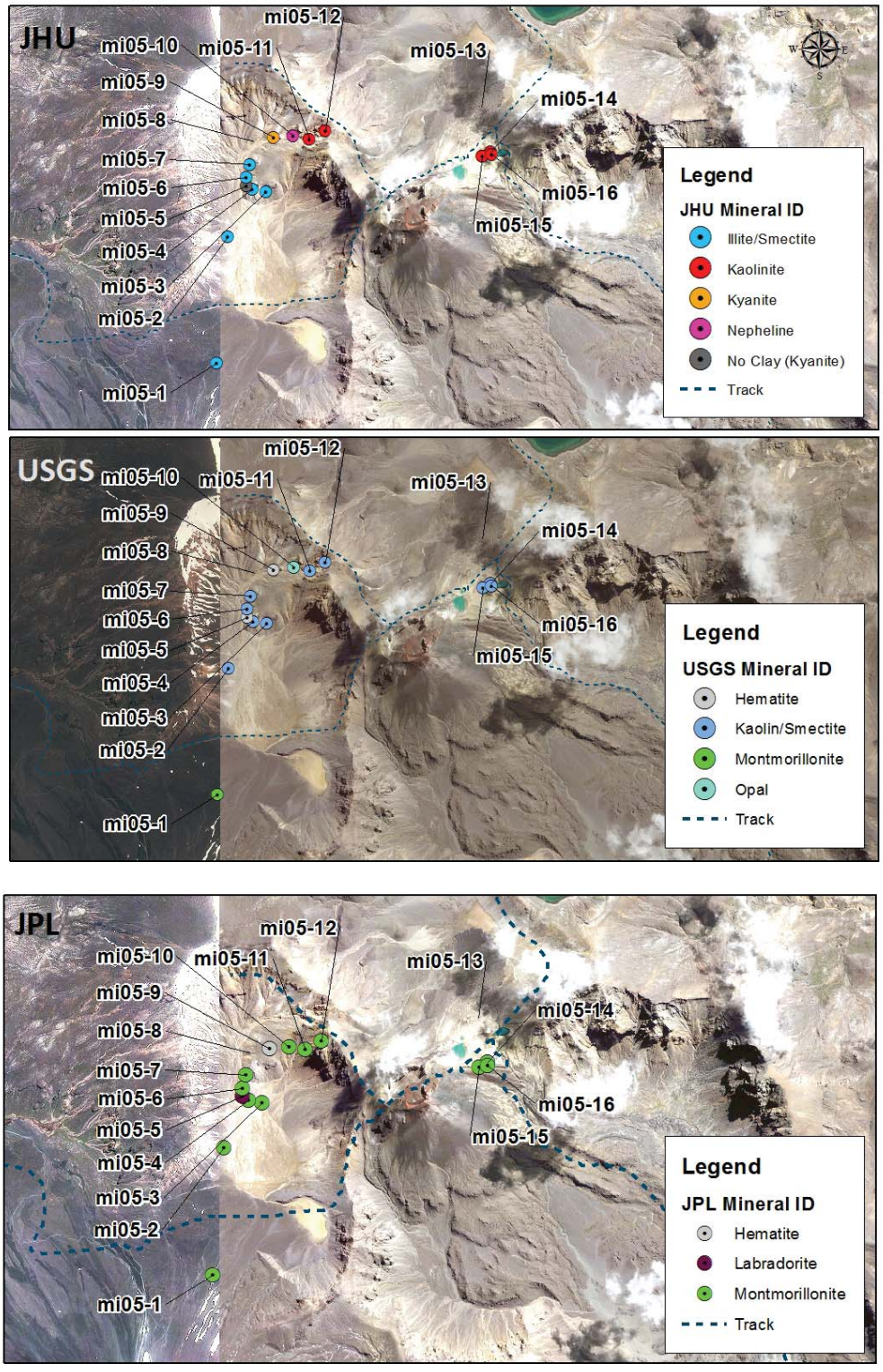

Figure 6-4 Locations and spectral identification results from the JHU, USGS and JPL mineral spectral library for the MI05 samples.

North crater contained most of the Smectite samples, but the matches to spectral analysis were not strong. This may indicate that the area only underwent a short period of alteration. Stronger matches between techniques were found in the Ketetahi Springs area,

possibly because they have vigorous and active hydrothermal alteration processes for longer periods of time that result in higher degrees of alteration. The locations of the MI05 samples have been plotted showing the identification result for each spectral library (Figure 6-4). This shows the spatial distribution of the samples and also the variation of identification results when using a particular spectral library. It is important to consider the results from all 3 libraries before accepting a result. MI05-5 gave non-clay identifications in all 3 libraries, and MI05-10 was identified as Hematite in two of the three libraries. The rest of the samples show a similar spatial pattern and similar identification in all three libraries. Overall the spectral matches were very successful and being verified against an independent source shows that the results are valid and can be relied on. Appendix A shows all the match data with all 3 spectral libraries.

6.5 XRD versus VNIR Spectroscopy

There were some discrepancies between the XRD results and the VNIR Spectroscopy in the samples examined in this study. This raises a question as to which result is more reliable. Even within the spectral analysis, different minerals were identified in the different spectral libraries. Like XRD, the spectral analysis may be more conclusive if further sample preparation was carried out to concentrate the clay minerals. However, for the purpose of comparing to satellite imagery, identification of natural/mixed samples is key to successful identification. Thus, considering mineral identification from both ASD and the XRD results in association with the satellite data is required to give a confident result. XRD and Spectral analysis from VNIR compliment each other, and XRD provides bulk composition while VNIR spectroscopy samples the surface features. Similarly, with different spectral analysis results from different spectral libraries, a conservative approach is to use the results from all the libraries for correlation to the satellite data.

6.6 Future Work

To extend this research and carry out a much higher-resolution survey, a targeted remote sensing approach should be considered for Tongariro National Park. A recommended option would be to deploy an airborne hyperspectral sensor such as AVIRIS, HYMAP or FENIX. A sensor on an airborne platform has a significantly higher signal to noise ratio, because the reflected electromagnetic energy has a shorter path through the atmosphere to reach the sensor. A high signal to noise ratio results in higher quality data and an improved

classification and mineral identification would be more likely. Another improvement to the spectral analysis would be to create a new spectral library for the minerals found on Mt Tongariro. This would involve taking some larger samples, analysing them with the spectroradiometer in-situ and then in the lab. Ideally the spectral library should be made up of the purest mineral samples that are present on Mt Tongariro. Larger samples would allow them to be processed (ground, dispersed, and settled or centrifuged) and provide enough of the <2µm fraction (clay) for multiple analysis which would improve the identification. Finally, the image processing techniques used are advanced and complex. Interpretation can be difficult and any mistakes made in the image processing workflow can heavily alter the results.

Satellite data, Airborne sensor data along with VNIR spectroscopy provides a valuable method for identification of hydrothermal zones on volcanic environments, and as new hyperspectral data becomes available, this workflow should be pursued with those data.

7 Conclusions

Although there are issues associated with the commonly mixed mineral assemblages in natural hydrothermal systems, the main mixtures identified in this study include Smectite, Illite, Kaolinite and Montmorillonite. All of these clays appear in hydrothermal alteration systems so their individual indentification is less important than the fact that “hydrothermal alteration clays” are present on a volcano, and they can be identified with a portable hyperspectral radiometer.

This study shows that portable hyperspectral spectroradiometer and XRD mineral identifications are able to be used to classify satellite imagery but much depends on the data spectral and spatial resolutions. Airborne hyperspectral data will provide the best opportunity for classification as due to its high signal to noise ratio. This data should show an improved correlation with the field spectroscopy and XRD data. If only satellite data is availble then the satellite sensor with the most bands in the mineral identification range which has been collected under optimal conditions should be used.

At present, identification of slope, vegetation and potentially geological contacts in relation to known hydrothermal features and ground-identified zones of smectite and other clays is probably the approach for mapping zones of weakness on volcanoes as found by this study. However, the approach of identifying wider areas of alteration should continue with the availability of new hyperspectral sensor imagery with greater spatial resolution, improved spectral resolution and higher signal to noise relationships of remotely sensed data.

References

Aizawa, K., Ogawa, Y., and Ishido, T., 2009, Groundwater flow and hydrothermal systems within volcanic edifices: Delineation by electric self-potential and magnetotellurics: Journal of Geophysical Research: Solid Earth, v. 114, no. B1, p. n/a-n/a.

Aranoff, S., 2005, Remote sensig for GIS managers, Redlands, ESRI Press, 487 p.:

ASD-Inc, 2002, FieldSpec Pro Users Guide.

Brady, D. J., 2009, Optical imaging and spectroscopy / David J. Brady, Hoboken, N.J. : Wiley ; [Washington, D.C.] : Optical Society of America, c2009.

Brindley, G. W., and Brown, G., 1980, Crystal structures of clay minerals and their X-ray identification / edited by G.W. Brindley and G. Brown, London : Mineralogical Society, 1980.

[New ed.], Monograph / Mineralogical Society: no. 5.

Capra, L., Macias, J. L., Scott, K. M., Abrams, M., and Garduno-Monroy, V. H., 2002, Debris avalanches and debris flows transformed from collapses in the Trans-Mexican Volcanic Belt, Mexico - behavior, and implications for hazard assessment: Journal of Volcanology and Geothermal Research, v. 113, no. 1-2, p. 81-110.

Churchman, G., Whitton, J. S., Claridge, G. G. C., and Theng, B. K. G., 1984, Intercalation Method Using Formamide For Differentiating Halloysite From Kaolinite: Clays and Clay Minerals, v. 32, p. 8.

Crowley, J. K., and Zimbelman, D. R., 1997, Mapping hydrothermally altered rocks on Mount Rainer, Washington, with Airborne Visible/Infrared Imaging Spectrometer (AVIRIS) data: Geology, v. 25, p. 559-562.

Evans, A. M., 1993, Ore Geology and Industrial Minerals, An Introduction, Boston, Oxford, Blackwell Scientific Publications.

Gillingham, S. S., 2002, Atmospheric Correction of New Zealand Landsat ImageryMaster of Philosophy]: Massey Universtiy, 117 p.

Hoblitt, R. P., Walder, J., Driedger, C., Scott, K., Pringle, P., and Vallance, J., 1995, Volcano Hazards from Mount Rainier, Washington, US Department of the Interior, US Geological Survey.

Hochstein, M., Steaming ground at Red Crater and in the Te Mari Craters, Mt. Tongariro geothermal system (New Zealand), *in* Proceedings Proc. 7th NZ Geothermal Workshop1985, p. 177-180.

Hunt, G. R., and Ashley, R. P., 1979, Spectra of Altered Rocks in the Visible and Near Infrared: Economic Geology, v. 74, p. 1613-1629.

ITTVis, 2005, The Environment for Visualizing Images (ENVI) software: Boulder, Colorado.

JPL, 2004, ASTER Instrument Characteristics.

Kruse, F. A., Mineral Mapping with AVIRIS and EO-1 Hyperion, *in* Proceedings AVIRIS Airbourne Geoscience Workshop2003.

Kruse, F. A., Boardman, J. W., and Huntington, J. F., 2003, Comparison of airborne hyperspectral data and EO-1 Hyperion for mineral mapping: Geoscience and Remote Sensing, IEEE Transactions on, v. 41, no. 6, p. 1388-1400.

Kruse, F. A., Boardman, J. W., Huntington, J. F., Mason, P., and Quigley, M. A., Evaluation and validation of EO-1 Hyperion for geologic mapping, *in* Proceedings Geoscience and Remote Sensing Symposium, 2002. IGARSS '02. 2002 IEEE International

Geoscience and Remote Sensing Symposium, 2002. IGARSS '02. 2002 IEEE International VO - 12002, Volume 1, p. 593-595 vol.591.
Lillesand, T. M. K., Ralph W., 2000, Remote sensing and image interpretation, New York, John Wiley and Sons, Inc.
López, D. L., and Williams, S. N., 1993, Catastrophic volcanic collapse: relation to hydrothermal processes: Science (New York, N.Y.), v. 260, no. 5115, p. 1794-1796.
Martí, J., and Ernst, G., 2005, Volcanoes and the environment / edited by Joan Martí and Gerald Ernst, New York : Cambridge University Press, 2005.
McGuire, W., 2003, Volcano instability and lateral collapse: Revista, v. 1, p. 33-45.
Milton, E. J., Schaepman, M. E., Anderson, K., Kneubühler, M., and Fox, N., 2009, Progress in field spectroscopy: Remote Sensing of Environment, v. 113, Supplement 1, no. 0, p. S92-S109.
Moon, C. J., Whateley, M. K. G., and Evans, A. M., 2006, Introduction to mineral exploration, Malden, MA, Blackwell Pub.
Moore, D. M., and Reynolds, R. C., 1989, X-ray diffraction and the identification and analysis of clay minerals / Duane M. Moore, Robert C. Reynolds, Jr, Oxford [England] ; New York : Oxford University Press, 1989.
Mosser-Ruck. R, Devineau. K, Charpentier. D, and Cathelineau. M, 2005, Effects Of Ethylene Gycol Saturation Protocols On XRD Patterns: A Critical Review and Discussion: Clays and Clay Minerals, v. 53, no. 6.
Reid, M. E., Sisson, T. W., and Brien, D. L., 2001, Volcano collapse promoted by hydrothermal alteration and edifice shape, Mount Rainier, Washington: Geology, v. 29, no. 9, p. 779-782.
Rencz, A. N., 1999, Manual of Remote Sensing: Remote Sensing for the Earth Sciences, Volume 3: New York, Wiley.
Schowengerdt, R., A., 2007, Remote Sensing: Models and Methods for Image Procesing, Academic Press.
Siebert, L., 1992, Threats from debris avalanches: Nature, v. 356, no. 6371, p. 658-659.
Siebert, L., Glicken, H., and Ui, T., 1987, Volcanic hazards from Bezymianny- and Bandai-type eruptions: Bulletin of Volcanology, v. 49, no. 1, p. 435-459.
Tilling, R. I., 1989, Volcanic hazards / Robert I. Tilling, editor, Washington, DC : American Geophysical Union, 1989.
USGS, 2003, EO-1 User Guide, *in* Beck, D. R., ed., Version 2.3: Cincinnati, Ohio, online.
-, 2016, On Demand Surface Reflectance - VNIR & Crosstalk Corrected SWIR: https://lpdaac.usgs.gov/dataset_discovery/aster/aster_products_table/ast_07xt.
van der Meer, F., 2006, The effectiveness of spectral similarity measures for the analysis of hyperspectral imagery: International Journal of Applied Earth Observation and Geoinformation, v. 8, no. 1, p. 3-17.
Voight, B., and Elsworth, D., 1997, Failure of volcano slopes: Geotechnique, v. 47, no. 1, p. 1-31.
Whitton, J. S., and Churchman, G. J., 1987, Standard Methods for Mineral Analysis of Soil Survey Samples for Characterisation and Classification in NZ Soil Bureau, Standard Methods for Mineral Analysis of Soil Survey Samples for Characterisation and Classification in NZ Soil Bureau B2 - Standard Methods for Mineral Analysis of Soil Survey Samples for Characterisation and Classification in NZ Soil Bureau: Lower Hutt, New Zealand.

Yuan, J., and Niu, Z., Classification Using EO-1 Hyperion Hyperspectral and ETM Data, *in* Proceedings Fuzzy Systems and Knowledge Discovery, 2007. FSKD 2007. Fourth International Conference on
Fuzzy Systems and Knowledge Discovery, 2007. FSKD 2007. Fourth International Conference on VO - 32007, Volume 3, p. 538-542.

Appendix A

ASD Spectra of collected samples compared to 3 Spectral Libraries

JHU Spectral Library Comparisons

Sample MI05-1 Illite Match: 0.745

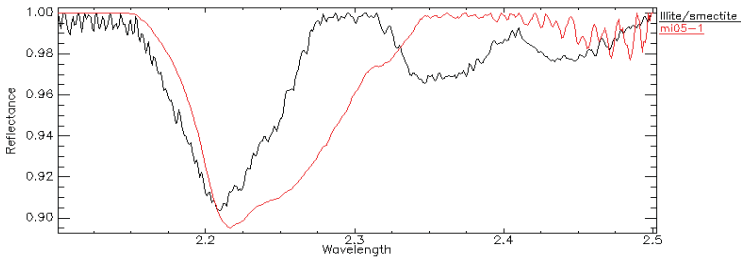

Sample MI05-2 Illite/Smectite match: 0.847

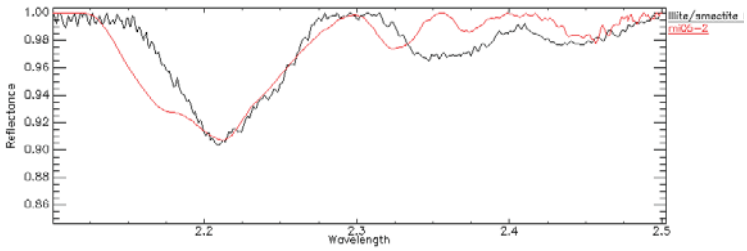

Sample MI05-3 Illite/Smectite match: 0.838

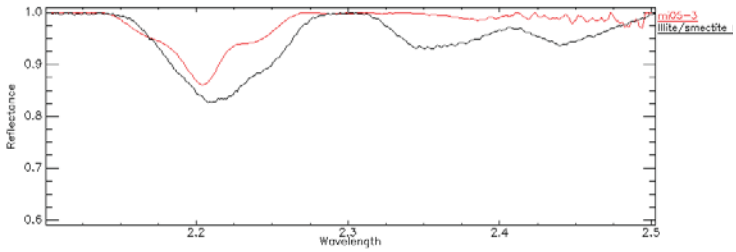

Sample MI05-4 USGS Match: Illite/Smectite 0.871

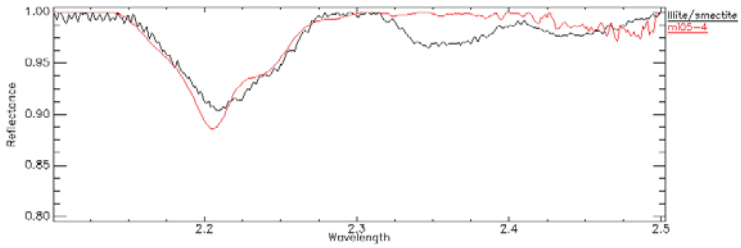

Sample MI05- No Clay match. Kyanite (Al2SiO5) match 0.837

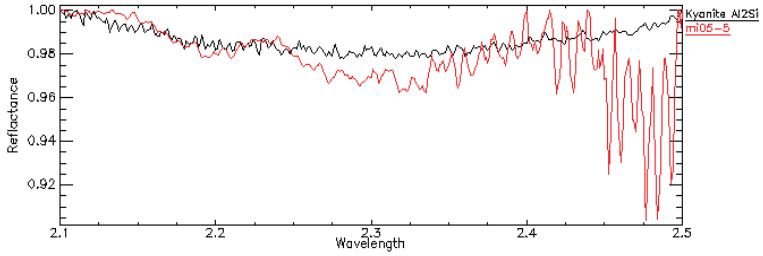

Sample MI05-6 JHU Match: Illite/Smectite 0.882

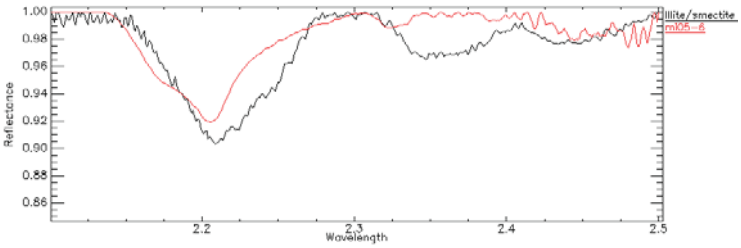

Sample MI05-7 JHU Match: Illite/Smectite 0.878

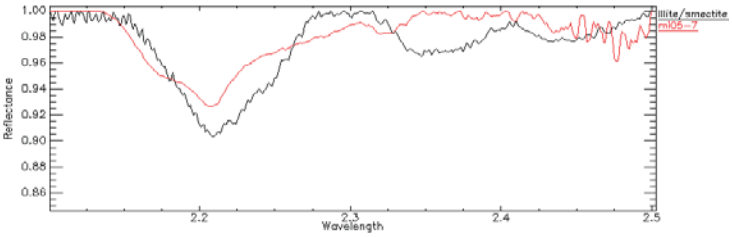

Sample MI05-9 JHU Match: Kyanite 0.920

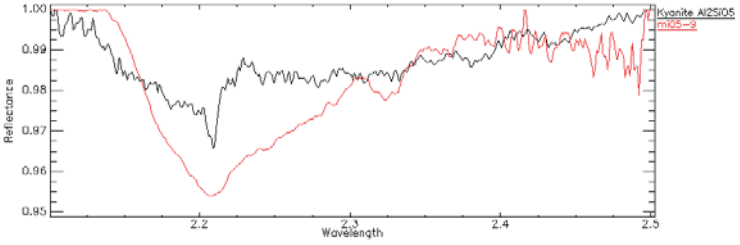

Sample MI05-10 No Clay. JHU Match: Nepheline 0.779

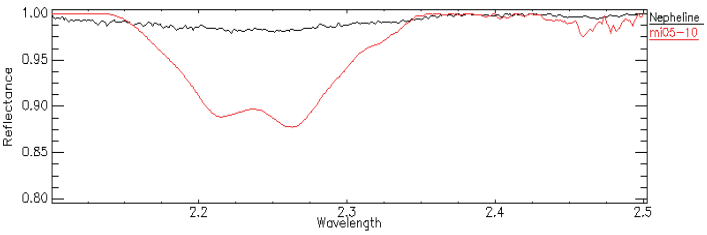

Sample MI05-11 JHU Match: Kaolinite 0.866

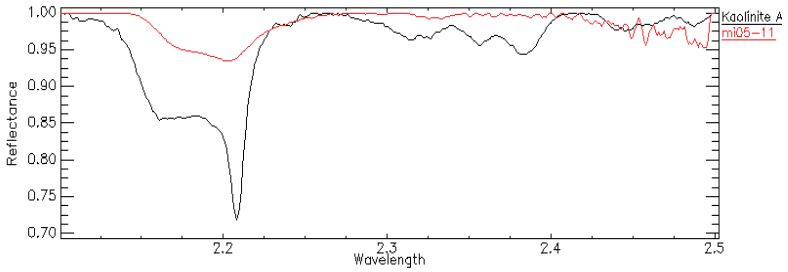

Sample MI05-12 JHU Match: Kaolinite 0.859

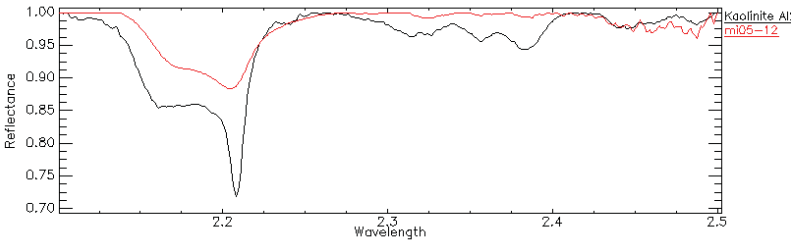

Sample MI05-14 JHU Match: Kaolinite 0.800

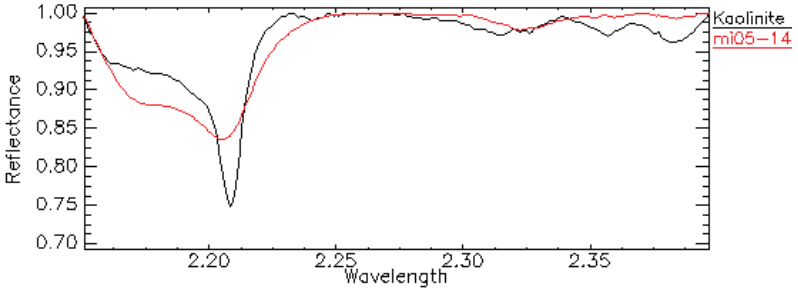

Sample MI05-15 JHU Match: Kaolinite 0.871

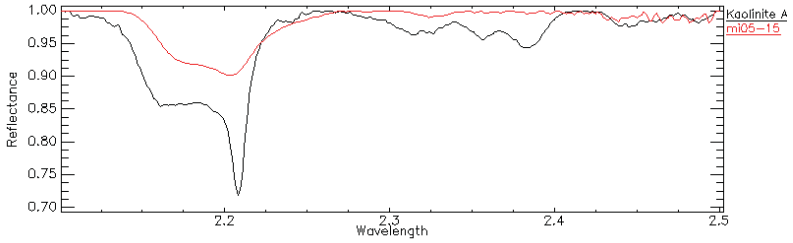

Sample MI05-16 JHU Match: Kaolinite 0.776

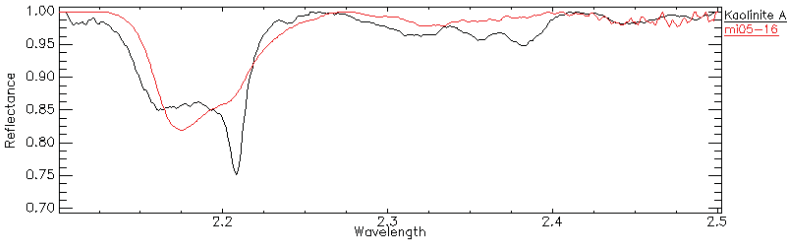

Sample MI06-1 JHU Match: Kaolinite 0.839

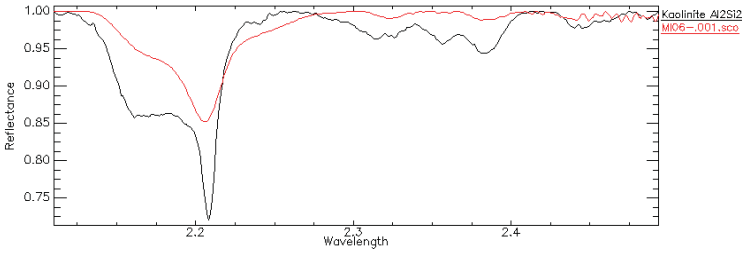

Sample MI06-2 JHU Match: Kaolinite 0.820

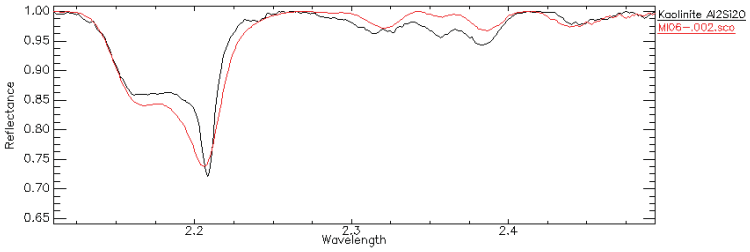

Sample MI06-3 JHU Match: Analcime 0.971

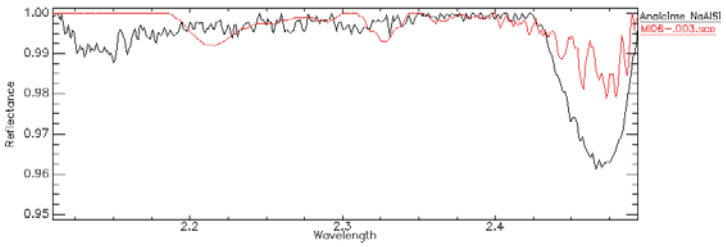

Sample MI06-4 JHU Match: Erionite 0.966

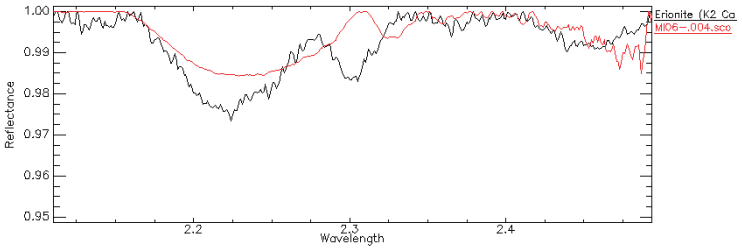

Sample MI06-5 JHU Match: Erinote 0.943

JHU Match: Illite/Smectite 0.928

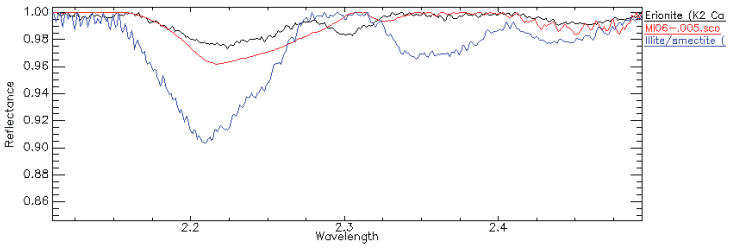

Sample MI06-6 JHU Match: Illite/Smectite 0.785

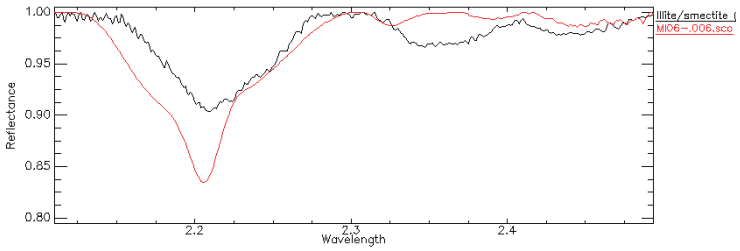

USGS Spectral Library Comparisons

Sample MI05-1 USGS Match: Montmorillonite 0.773

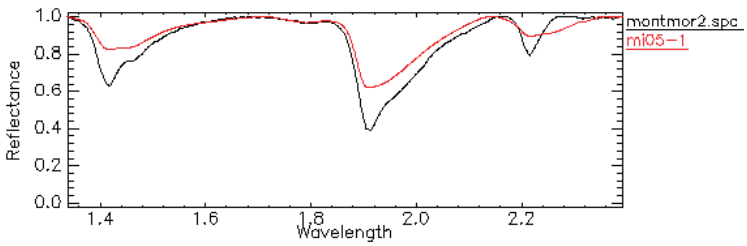

Sample MI05-2 USGS Match: Kaolin/Smectite 0.839

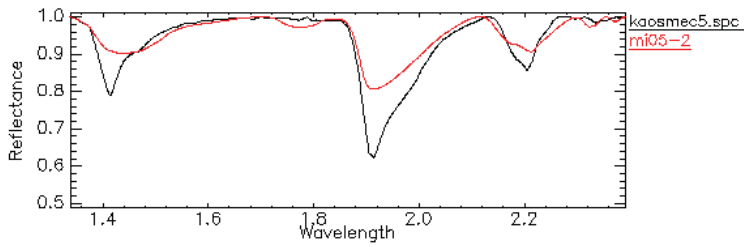

Sample MI05-3 USGS Match: Kaolin/Smectite 0.876

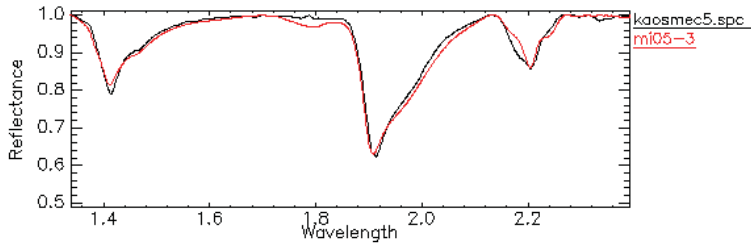

Sample MI05-4 USGS Match: Kaolin/Smectite 0.862

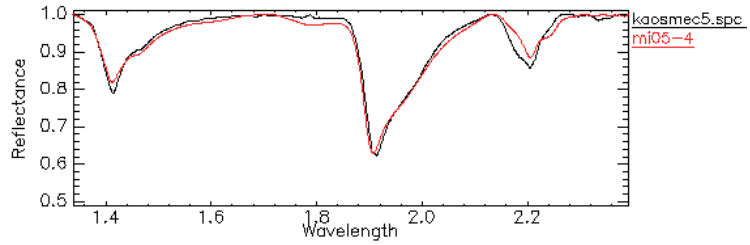

Sample MI05-5 USGS Match: USGS Match: Hematite 0.850

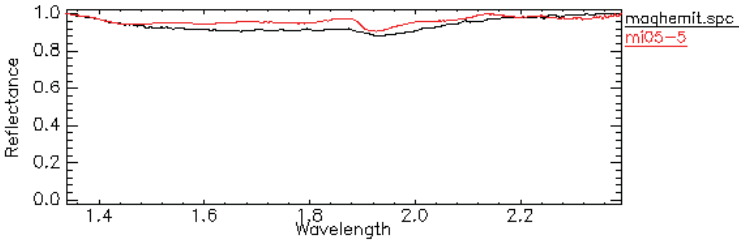

Sample MI05-6 USGS Match: Kaolin/Smectite 0.739

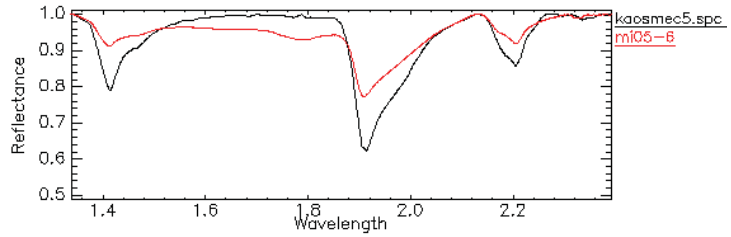

Sample MI05-7 USGS Match: Kaolin/Smectite 0.794

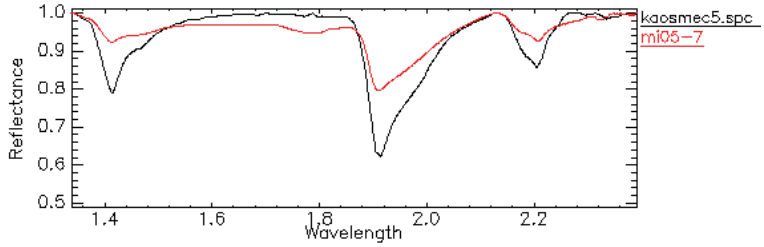

Sample MI05-9 USGS Match: Hematite 0.868

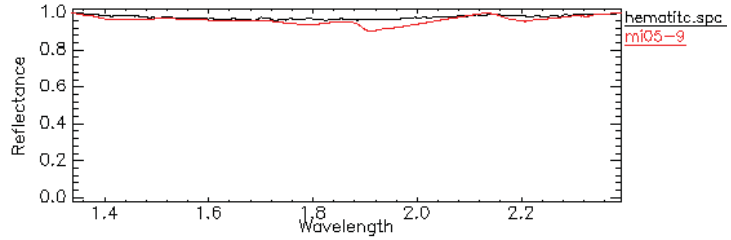

Sample MI05-10 USGS Match: Opal 0.774

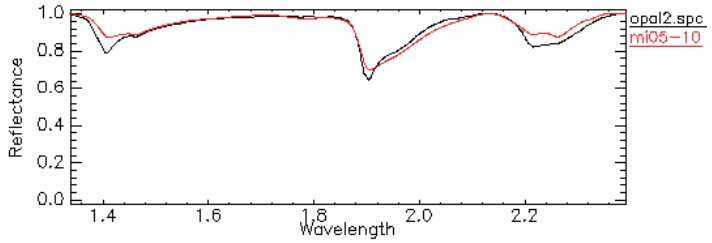

Sample MI05-11 USGS Match: Kaolin/Smectite 0.663

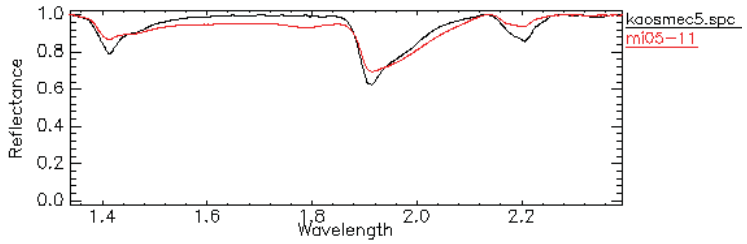

Sample MI05-12 USGS Match: Kaolin/Smectite 0.880

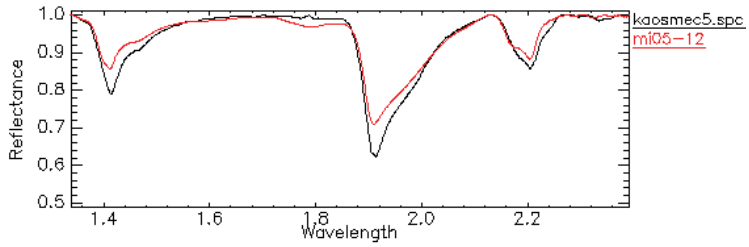

Sample MI05-14 USGS Match: Montmorillonite 0.691

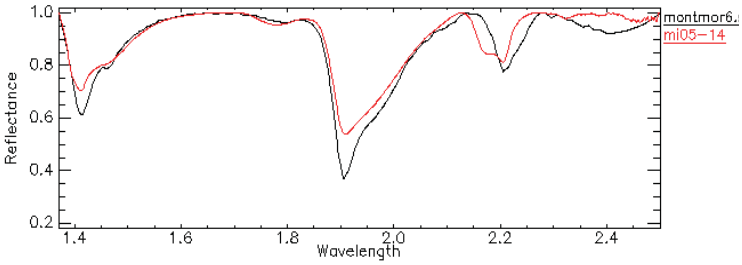

Sample MI05-15 USGS Match: Kaolin/Smectite 0.904

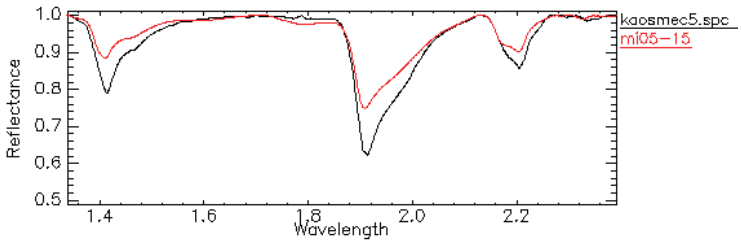

Sample MI05-16 USGS Match: Kaolin/Smectite 0.855

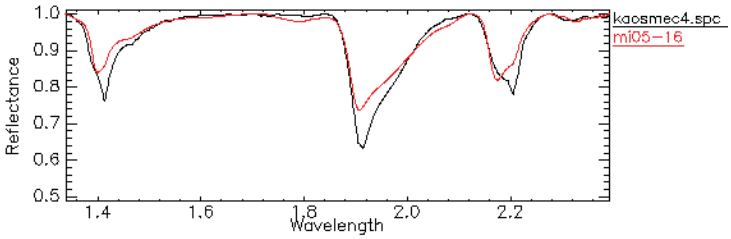

Sample MI06-1 USGS Match: Kaolin/Smectite 0.875

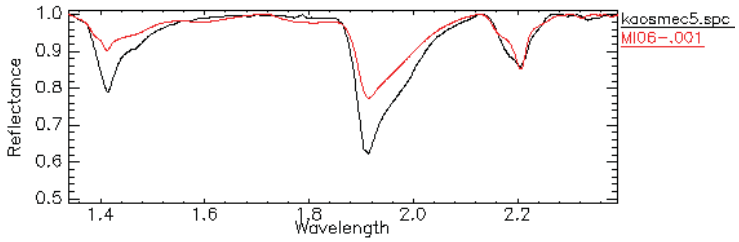

Sample MI06-2 USGS Match: Kaolin/Smectite 0.875

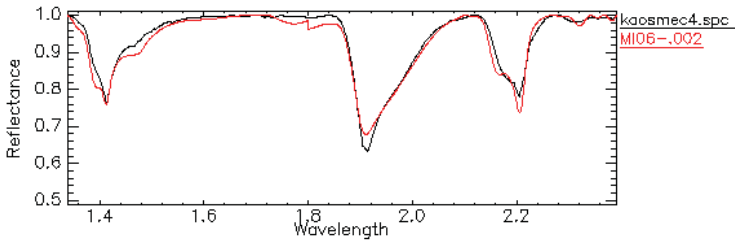

Sample MI06-3 USGS Match: Heulandite 0.676

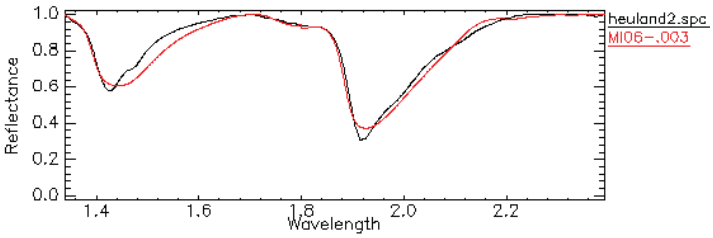

Sample MI06-4 USGS Match: Lamontite 0.865

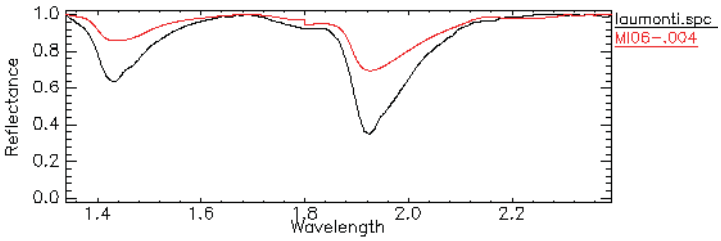

Sample MI06-5 USGS Match: Ferrihydrite 0.778

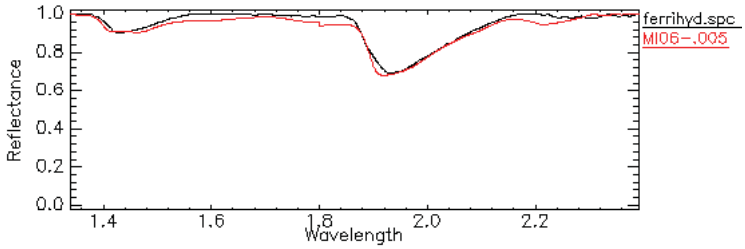

Sample MI06-6 USGS Match: Kaolin/Smectite 0.852

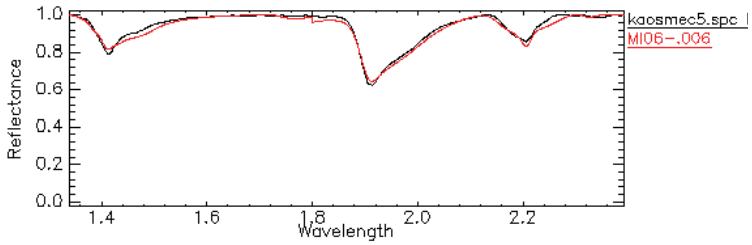

JPL Spectral Library Matches

Sample MI05-1 JPL Match: Montmorilonite 0.695

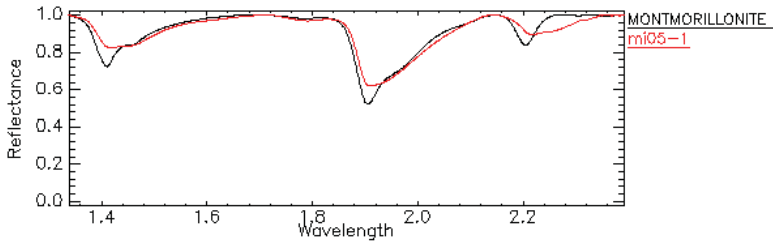

Sample MI05-2 JPL Match: Montmorilonite 0.812

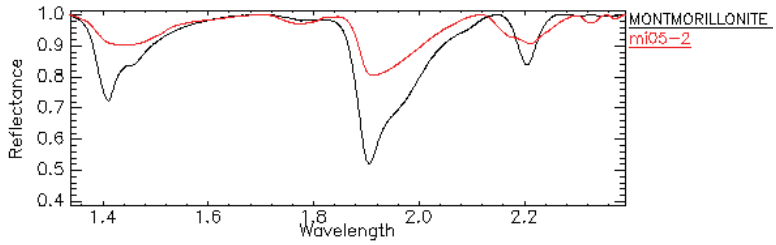

Sample MI05-3 JPL Match: Montmorilonite 0.836

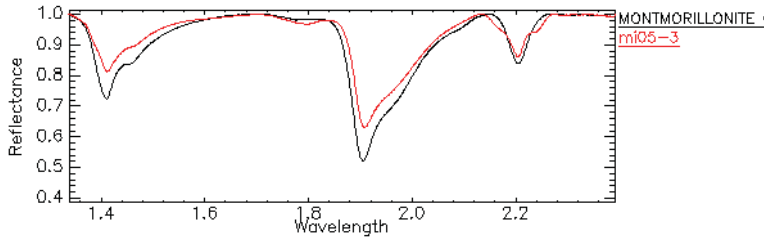

Sample MI05-4 JPL Match: Montmorilonite 0.850

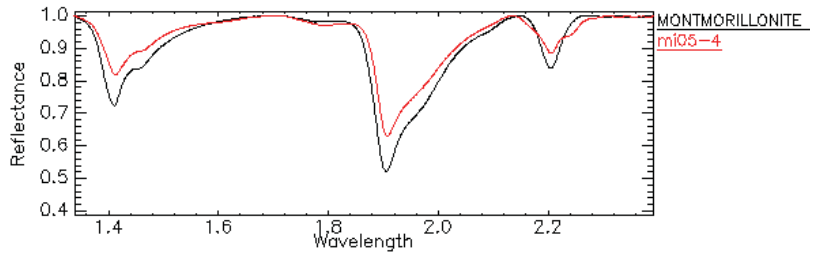

Sample MI05-5 JPL Match: Labradorite 0.864

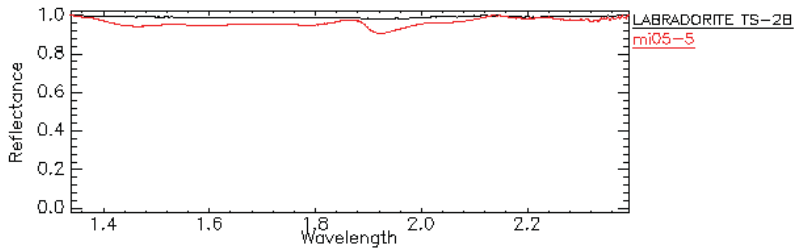

Sample MI05-6 JPL Match: Montmorilonite 0.738

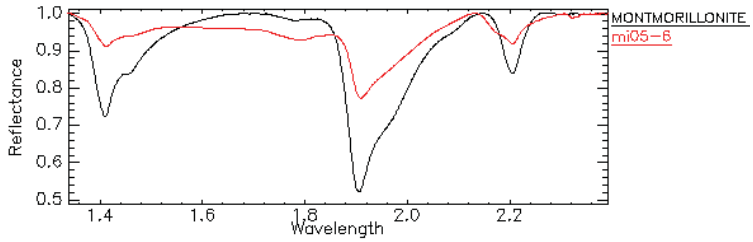

Sample MI05-7 JPL Match: Montmorilonite 0.781

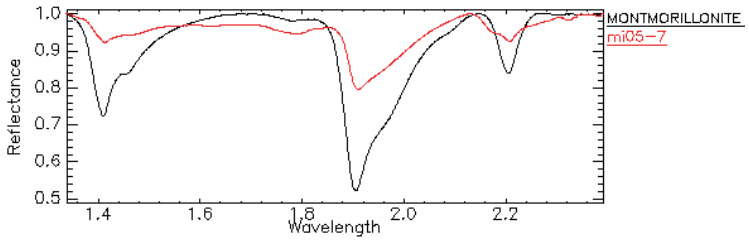

Sample MI05-9 JPL Match: Hematite 0.858

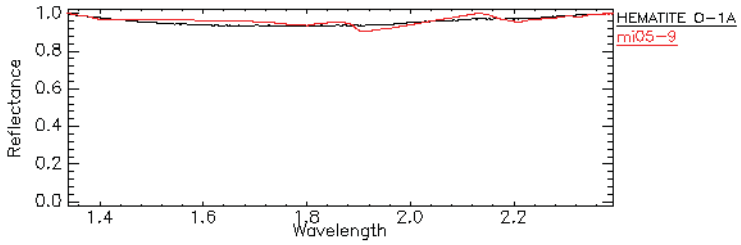

Sample MI05-10 JPL Match: Montmorilonite 0.706

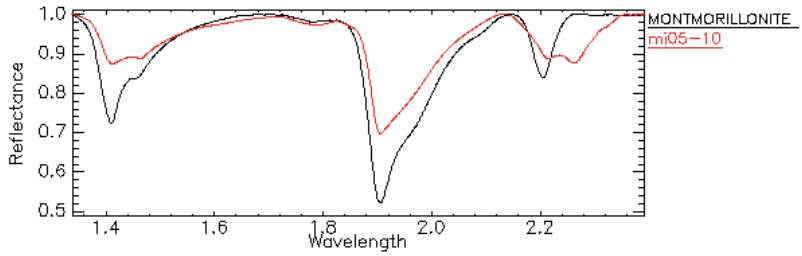

Sample MI05-11 JPL Match: Montmorilonite 0.665

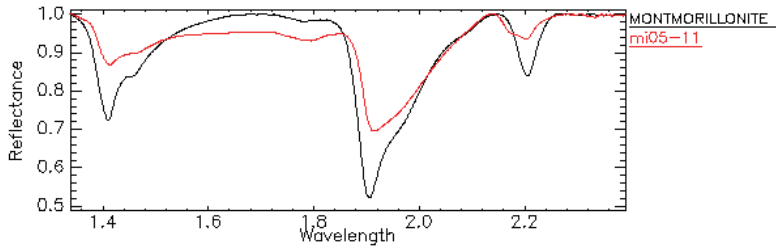

Sample MI05-12 JPL Match: Montmorilonite 0.805

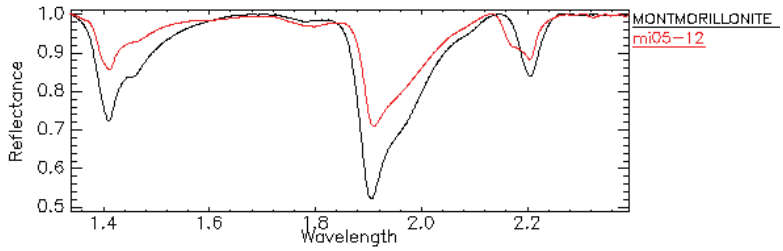

Sample MI05-14 JPL Match: Montmorilonite 0.678

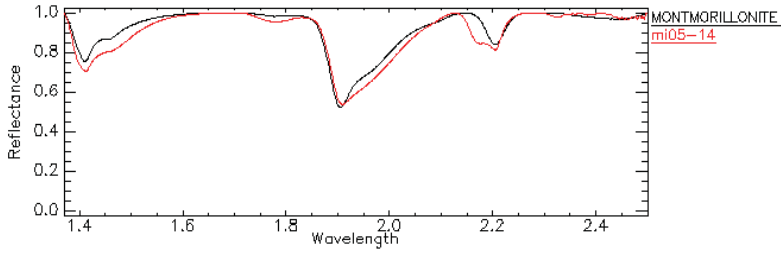

Sample MI05-15 JPL Match: Montmorilonite 0.842

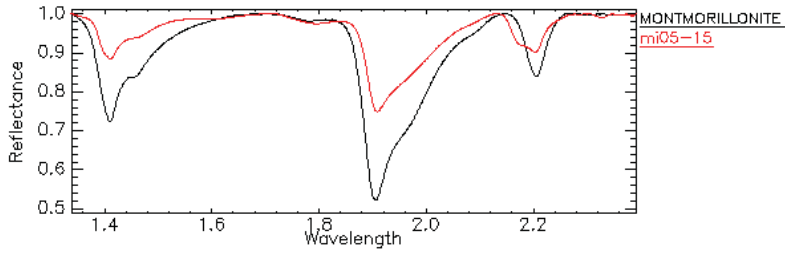

Sample MI05-16 JPL Match: Montmorilonite 0.762

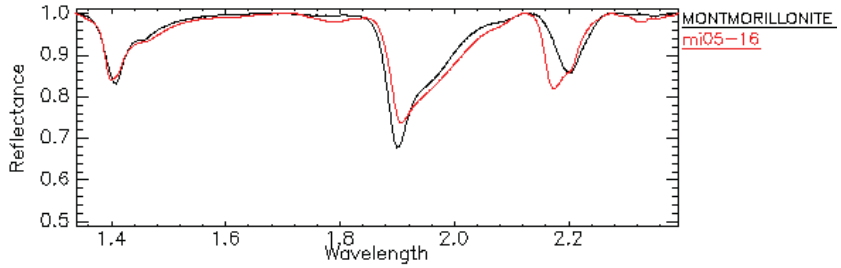

Sample MI06-1 JPL Match: Montmorillonite 0.829

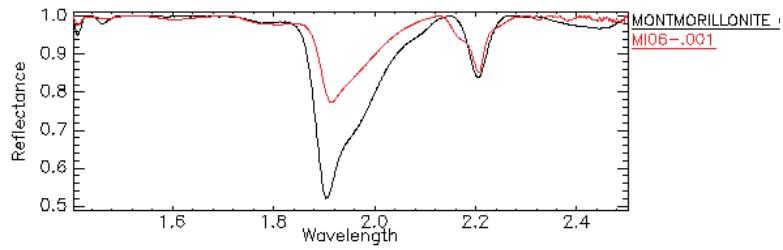

Sample MI06-2 JPL Match: Montmorillonite 0.702

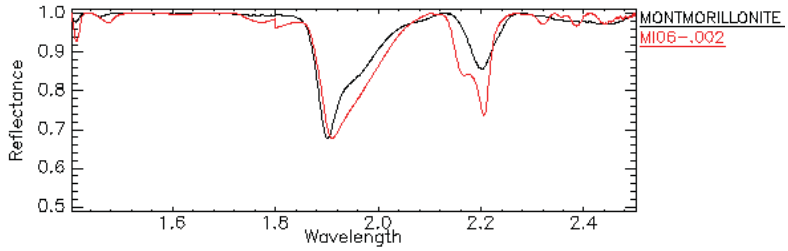

Sample MI06-3 JPL Match: Nontronite 0.345

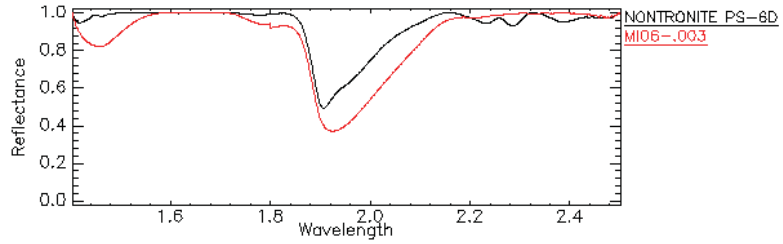

Sample MI06-4 JPL Match: Nontronite 0.747

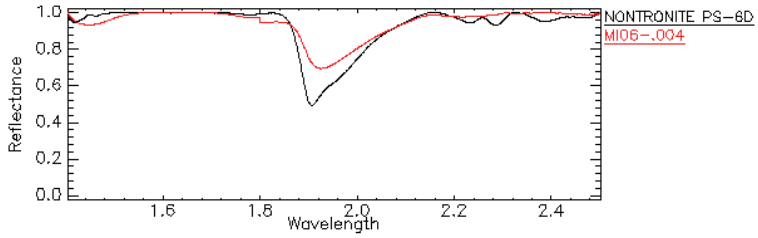

Sample MI06-5 JPL Match: Nontronite 0.733

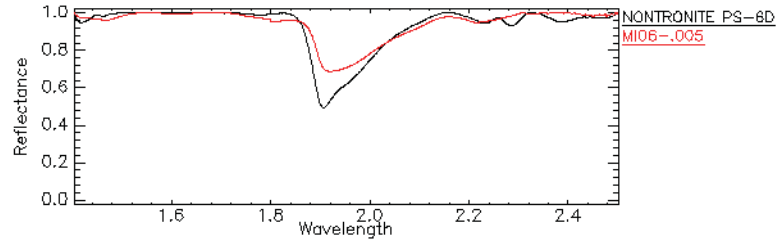

Sample MI06-6 JPL Match: Montmorillonite 0.780